SURFACE CHARACTERIZATION OF AMORPHOUS HYDROGENATED CARBON THIN FILMS CONTAINING NANOCLUSTERS OF NOBLE METALS

INAUGURALDISSERTATION

zur

Erlangung der Würde eines Doktors der Philosophie

vorgelegt der

Philosophisch–Naturwissenschaftlichen Fakultät

der Universität Basel

von

Ivan R. Videnović

aus Belgrad, Serbien & Montenegro

Basel, Juli 2003

Genehmigt von der Philosophisch–Naturwissenschaftlichen Fakultät
auf Antrag von:

Prof. Dr. Peter Oelhafen
Prof. Dr. Ernst Meyer

Basel, den 8. Juli 2003

Prof. Dr. Marcel Tanner, Dekan

mojoj majci

to my mother

Foreword

At the end of this significant task and, from every point of view exceptional and remarkable period of my life spent in Basel and in Switzerland, I would like to thank to all those who made it possible.

First of all, I wish to express my deepest gratitude to Prof. Dr. Peter Oelhafen. He admitted me in his research group in November 1999, at the time when political conditions in my country were such that many people in his position would hesitate or be reluctant to do so. I thank him for his open-minded attitude, for guiding me on my way to the Ph.D. title, and for enabling me to participate in some of the most prominent scientific meetings in this period.

I would also like to thank Prof. Dr. Ernst Meyer for his kind acceptance of the "co-referentship" of this work.

The financial support of the Bundesamt für Energie, Switzerland, and of the Swiss National Science Foundation is gratefully acknowledged.

I am indebted to Acad. Prof. Dr. Nikola Konjević (Faculty of Physics, University of Belgrade), my Master's degree supervisor, for providing me scientific background prior to my start in Basel. He was also persisting in our correspondence, thus enabling me to stay in touch with scientific activities in my homeland. Most of all, I thank him for his support and offering safe harbor in one difficult moment in the course of this Ph.D.

For granting me a leave from my teaching and research duties at the Faculty of Physics of the Belgrade University, my thanks goes also to the former and actual Deans of the Faculty of Physics of Belgrade University, Prof. Dr. Dragomir Krpić and Prof. Dr. Milan Knežević, respectively, to the vice-Deans Prof. Dr. Sunčica Elezović-Hadžić, Doc. Dr. Zoran Radović, and Prof. Dr. Mićo Mitrović, as well as to the Faculty Council and administration.

I had a fortune to make my first steps in photoelectron spectroscopy with help and instructions of a brilliant physicist and my good friend Dr. Andreas Schüler, who was completing his Ph.D. at that time. I think we made a good merger of his talent and efficiency and my experience to make some joint work even after his leave from the group. I appreciate that very much.

I wish to thank all actual and former members of Prof. Oelhafen's ESCA group at the Institute of Physics in Basel, that I had fortune to work with:

Dr. Teresa de los Arcos,
Dr. Georges Reber,
Dr. Andriy Romanyuk,
Dr. Marc Ley,
BA Ling. Dipl. Phys. Shui Ching Ho,
Dipl. Phys. Jamila Boudaden,
Dipl. Phys. Michael Büttner,
Ing. HTL Roland Steiner,
Dr. Michael Gunnar Garnier,
Dr. Dieter Robert Kohler,
Dr. Matthias Töwe,
Dr. Ralf Wahrenberg,

PD Dr. Petra Reinke,
Dr. Jürgen Geng,
Dr. Andreas Schüler,
Dr. Thormen Wrase,
PD Dr. Hans-Gerd Boyen,
Dr. Paul Gantenbein.

For dedicated work in atomic force microscopy of my samples I thank Ms. Verena Thommen.

My nanocluster samples with “nothing to see on them” have caused a lot of headaches to Daniel Mathys and Marcel Düggelin, who did their best to make scanning electron microscopy images in the Zentrum für Mikroskopie of the Basel University. I am thankful for their work.

The joint work and assistance of Dr. David Babonneau from the Laboratoire de Métallurgie Physique, Université de Poitiers, France, in grazing incidence small-angle x-ray scattering studies of our samples is gratefully acknowledged.

When it inevitably comes to the liquid nitrogen, the work in our Institute would be impossible without generous assistance of Mr. Werner Roth.

My special thanks goes to the secretaries of the Institute of Physics, two remarkable ladies, Ms. Barbara Kammermann and Ms. Astrid Kalt. Their efforts in number of necessary supporting activities for our group, often beyond their responsibilities, are highly appreciated.

For the assistance when we were stacked in our ignorance in electronics, as well as for the friendly atmosphere in the working surrounding, I thank the Electronics Laboratory members Michael Steinacher, Bernd Heimann, and Werner Erni.

I am grateful to all my friends in Basel for spending some unforgettable time together. I will remember these moments for good. My special thanks goes to Dr. Sanja Schmutz, who persuaded me in the first place to apply for this position and continue my work in Basel.

I thank all my friends, those in Serbia and those scattered all over the globe for keeping in touch and sharing both joy and grief from our private lives and from that unsettled and stormy region where we originate from.

I deeply thank Mrs. Mirzeta Savić for sincere and sustained friendship that helped me a lot in the course of this work.

I am indebted to my wife Dejana for her courage, faith, and love, when she decided to postpone the normal life for some years and join me in this difficult journey. She accepted hard conditions of separated life during my time here, though some might say that was actually – an extended honeymoon. Anyway, I thank her and I love her more for that.

I dedicate this work and this dissertation to my mother Dr. Ivanka Videnović. Without her support, help, and comfort, as well as the great family work done on my behalf far back at home, I would simply not manage to get through to this point.

Basel, July 2003

Table of contents

1. Introduction

Amorphous hydrogenated carbon (*a*-C:H) thin films have attracted a lot of attention of material-science investigators in the past two decades [1,2]. Being an amorphous network of carbon and hydrogen, it consists of carbon atoms linked by sp^2 (trigonal, graphitic-like) and sp^3 (tetragonal, diamond-like) bonds, see Fig. 1.1. The amorphous nature of these coatings leaves the space to alter, by selecting the deposition methods and parameters, the sp^3/sp^2 coordinated carbon ratio, reaching maximum of more than 80% sp^3 bonds in tetrahedral hydrogen-free amorphous carbon [3]. Providing therefore the hardness that compares to the one of crystalline diamond, these materials are also known under the more popular name *diamond-like carbon* (DLC). Beside the hardness, a series of properties make these materials exceptionally useful in wide range of applications. *a*-C:H is characterized by low friction coefficient and low wear rate that makes it suitable for solid lubrication and a variety of tribological purposes [4-9]. Special attention is devoted to biotechnological applications of *a*-C:H. Due to its low friction, *a*-C:H – coated artificial blood vessels, heart valves, and blood pumps show superior characteristics in reduction of thrombus formation, compared to other coatings or uncoated implants [10,11].

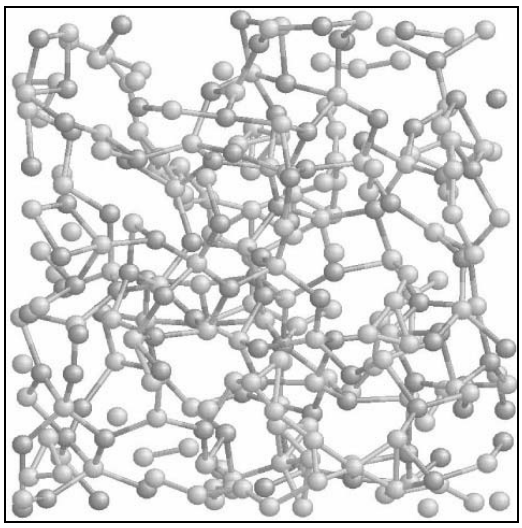

Fig. 1.1. Atomic structure of amorphous carbon network.

First evidence that metallic or metal carbide inclusions into *a*-C:H improve its friction coefficient and wear resistance was supplied by Dimigen and Hübisch [12], opening further applicative potential in tribology [13-20] and biotechnology [9,21-25]. A new field of interest for these materials was also opened in solar-selective absorbers for solar cells production [26-32].

Schüler *et al.* have recently studied titanium-containing *a*-C:H obtained in combined magnetron sputtering (MS) of Ti target and plasma-assisted chemical vapor deposition (PACVD) of *a*-C:H in argon-methane atmosphere as a potential solar-selective absorber [31]. They compared metal concentration in the bulk obtained by Rutherford backscattering spectroscopy (RBS), and surface Ti content measured by x-ray photoelectron spectroscopy (XPS). The metal concentration in the bulk was systematically higher than in the surface region. The question that arises is whether this systematic difference is caused by the coverage of the topmost metallic clusters with a tiny layer of *a*-C:H, of depth below electron escape depth? Or, in other words, are the surface metallic clusters only partially or fully embedded in the *a*-C:H matrix?

The latter case would provide an explanation of the observed discrepancies between RBS and XPS results [31].

Being a main inspiration, the above question implies a number of additional problems that together make a motivation of this work:

- Revealing of the surface structure and cluster arrangement of MS/PACVD nanocomposites within the first few monolayers,

- Studying the possibility to selectively etch the matrix, i.e. to uncover near-surface clusters to characterize them *in situ*,

- Investigation of the possibility to control the coverage of the surface clusters by selecting appropriate deposition parameters.

For this kind of study good candidates for doping *a*-C:H were noble transition metals of 1B group: gold, silver and copper.* These metals, in principle, do not form carbides and therefore, chemical shifts in XPS spectra are supposed to be absent. That makes *a*-C:H/Au, *a*-C:H/Ag and *a*-C:H/Cu suitable model systems for using photoelectron spectroscopy as a tool for studying size and arrangement of metallic clusters in the surface region of *a*-C:H matrix (see in detail in “Experimental techniques and procedures”, Paragraph 2.2.2).

So far, *a*-C:H/Au has been studied from the structural point of view by Schiffmann *et al.* [33,34] in order to establish the correlation between nanocluster size and size distribution and tribological improvements by metal inclusions into *a*-C:H. The scope of this work comprised also structural analysis of Au nanoclusters in *a*-C:H by means of grazing incidence small-angle x-ray scattering [35]. Optical properties of *a*-C:H/Au as a model system have been studied within solar-selective absorbers investigations [26,27]. Several studies have been devoted to the gold nanoparticle inclusions into other host dielectric matrices, such as silica where they caused nonlinear optical response [36], and polyacrilonitrite [37]. Gold nanoparticles themselves show interesting properties, like e.g. recently reported catalytic activity [38,39]. A novel breakthrough in understanding Au nanoparticles properties has been made by Boyen and coworkers [40-42], revealing the exceptional properties of Au nanoclusters that contain a „magic number“ of 55 atoms.

Silver-doped *a*-C:H has not been so extensively studied. The temperature-induced structural rearrangements studied by transmission electron spectroscopy and its influence on electrical conduction and optical transmission are reported by Biederman *et al.* [43,44]. Few RBS, XPS, and Raman spectroscopy studies of Ag and W ions implanted into polymide matrix have been also published [45,46]. The influence of doping *a*-C:H by silver for biocompatible purposes was studied by Hauert

* Throughout this work noble metals of 1B group will be sorted in this, descending order of atomic number and “nobility“.

et al. [21]. Several studies on characterization of nanocomposite materials containing Ag nanoclusters in other host matrices have been reported recently [47-53].

The most studied system of three selected in this work is *a*-C:H/Cu. Starting as early as 1994, first structural study of DLC doped with copper by ion implantation [54] and electro-optical properties of material deposited by copper and graphite target magnetron co-sputtering [55] are reported. Soon, an influence on the film properties of *a*-C:H doping by copper (also Mo and N) at elevated annealing temperature [56], and a wear resistance of Cu-incorporated DLC are reported [57]. A great deal of investigations on *a*-C:H/Cu has been done by St. Petersburg's group headed by V. I. Ivanov-Omskiĭ [55, 58-64]. Wei *et al.* [65-67] used pulsed laser deposition of Cu and graphitic target to improve wear resistance of DLC by incorporating copper.

In this work, we studied the surface structure of *a*-C:H/Au, *a*-C:H/Ag, and *a*-C:H/Cu with emphasis on the arrangement and coverage of the surface metallic clusters, the information that was not available so far. It will be shown that three nanocomposite systems under investigation, apart from their particularities, share some common properties regarding topmost clusters coverage. That suggests that one should look for the cause of the coverage in the deposition process itself and thereby, also the possibility to control it. Controlled exposure of the surface metallic or carbidic clusters would be significant from point of view of almost all known applications of *a*-C:H nanocomposites. First of all, the chemical activity of these coatings may be tailored in this way. Clusters exposure to the surrounding environment or their total embedment into *a*-C:H matrix can influence tribological properties of the coatings, especially hard lubricants. In biotechnological applications, this property may affect the influence of some toxic metals used in medical implants, like e.g. silver, copper, or vanadium [9]. Finally, for usage in solar cells, coverage or baldness of the surface clusters may improve or degrade aging properties of solar-selective absorber coatings.

The text of this thesis is divided into four chapters followed by the list of references and appendices. The chapter that follows describes the experimental techniques and procedures employed. Third chapter and its sections contain results and comparative discussion of *a*-C:H/Au, *a*-C:H/Ag, and *a*-C:H/Cu nanocomposite systems. In the last chapter a summary, concluding remarks and some further perspectives are given.

2. Experimental techniques and procedures

2.1. Thin film deposition

Among a variety of thin films and coatings deposition methods [68], a conventional one is chemical vapor deposition (CVD). To create a vapor of a desired material for deposition, different means can be used, e.g. thermal, electrical, laser evaporation. If an electrical gas discharge is used as a tool to create a chemical vapor, such method is usually denoted as plasma-enhanced or plasma-assisted CVD (PACVD). The species of the material to be deposited on a substrate are contained in a carrying gas, which may be, prior to deposition, subjected to dissociation and resynthesis into different species in plasma (molecules like e.g. hydrocarbons to C_nH_m species, ammonia to N_nH_m, silane to Si_nH_m, etc.).

On the other hand, plasma is sustained, most commonly, between two solid electrodes. If carrying gas includes inert species (argon in most cases) with sufficient energy gained in plasma, that may result, after bombardment the cathode by energetic ions and neutrals, in ejecting cathode (*target*) material into the plasma. This phenomenon is known as *sputtering*. If a substrate is placed in the plasma region, sputtered species are deposited on it. This method of deposition is usually denoted as physical vapor deposition (PVD).

The above described implies that for enhancing CVD one may use the plasma that provides PVD itself. In this way, a combined PVD/PACVD results in the film which contains species that originate in both methods. If, in addition, these species create a chemical compound in the deposited film, the process is denoted as a reactive PVD/PACVD.

For a number of applicative purposes, thin film deposition has to meet a requirement of high purity of deposited coatings. In PVD/PACVD, that means that atmosphere with its constituents is a source of impurities. The chamber where thin films are to be obtained, therefore, has to be evacuated to the level at which these impurities may be tolerated. That leads us to the high vacuum (HV) conditions, i.e. $<10^{-6}$ mbar of the base pressure in the deposition chamber. The active gas pressure during the deposition usually ranges from 10^{-3} to 10^{-2} mbar.

To be sustained at pressures below 10^{-1} mbar, however, glow discharges generally need assistance of a magnetic field [69]. The role of the magnetic field is depicted in Fig. 2.1, where the schematics of argon sputtering process is given. Represented by curved arrow lines, magnetic field captures electrons in the vicinity of the cathode (target), thereby increasing electron concentration in this region. This leads to the increase of the ionization degree, and higher number of Ar^+ ions extracted from the plasma and accelerated towards the target. They arrive to the target mostly without any collision. If happened at all, the dominant collision process is charge ex-

change, which results in transformation of a fast ion into fast neutral. Hence, energetic argon ions and neutrals strike the target and eject its atoms back into the plasma. In this way the target material is deposited on the substrate, growing the film that represents, to the significant extent, the image of state of the target. These types of plasma sources are known as *magnetrons*, and deposition method also as magnetron sputtering (MS), the term that we will use throughout this work rather than PVD.

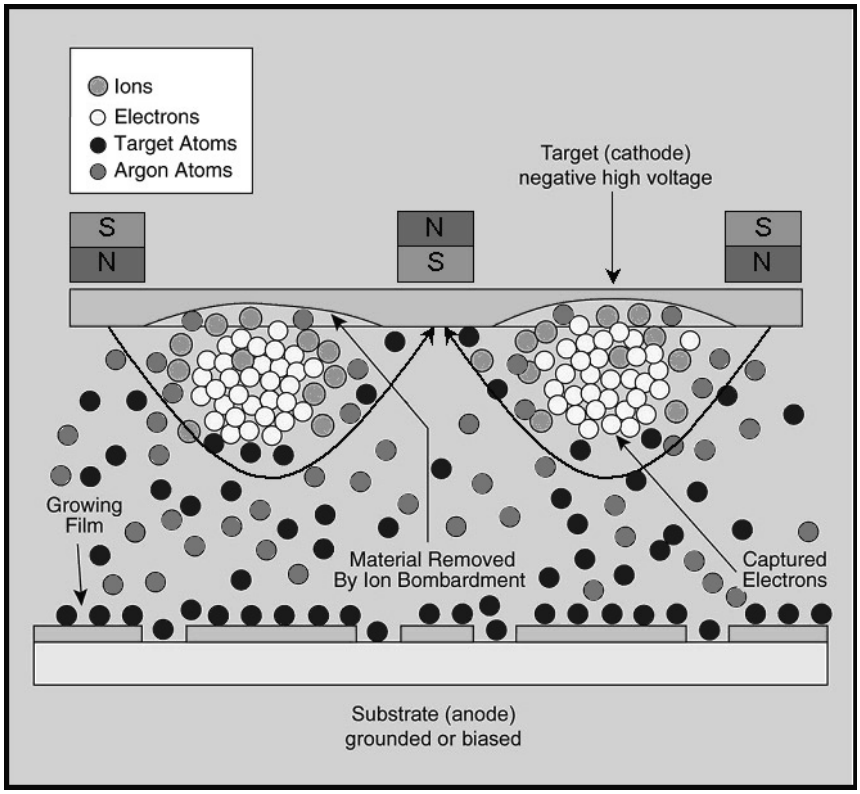

Fig. 2.1. Schematics of the sputtering deposition in a magnetron discharge.

To run the plasma, magnetron targets are powered with high negative voltage. This is most usually done with pulsed dc or radio-frequency (RF) power supplies. The usage of continuous dc power is restricted to conductive targets only. Employing pulsed instead of continuous dc powering with metallic targets shows advantages in covering entire target surface with plasma and hence, its more efficient exploitation and uniform consumption [70]. In this work a bipolar-pulsed (BPP) dc power supply (ENI, RPG-50) is predominantly used. Only few crosscheck experiments have been done using 13.56 MHz RF (Advanced Energy, RFX-600) power supply.

The walls of the deposition chamber play a role of anode in magnetron sputtering processes. The substrates used for deposition can be either kept on the walls potential (grounded), or independently biased with additional negative dc voltage. In the latter case, ionized target atoms are accelerated towards the substrate also. This feature is often used when higher density and lower roughness of deposited films are required. However, in this case the argon ions are accelerated not only towards the target, but also towards the substrate. This results in sputtering of the

deposited coating and often embedding argon in the film. The potential distribution in grounded and biased cases is shown in Fig. 2.2, where V_P is the plasma potential, slightly higher than the anode (ground) potential, V_T is the target potential, and V_B – the substrate bias voltage [71]. This figure is particularly important for this work, due to the differences in the nanocluster arrangement at the surface that we encountered with grounded and biased substrates.

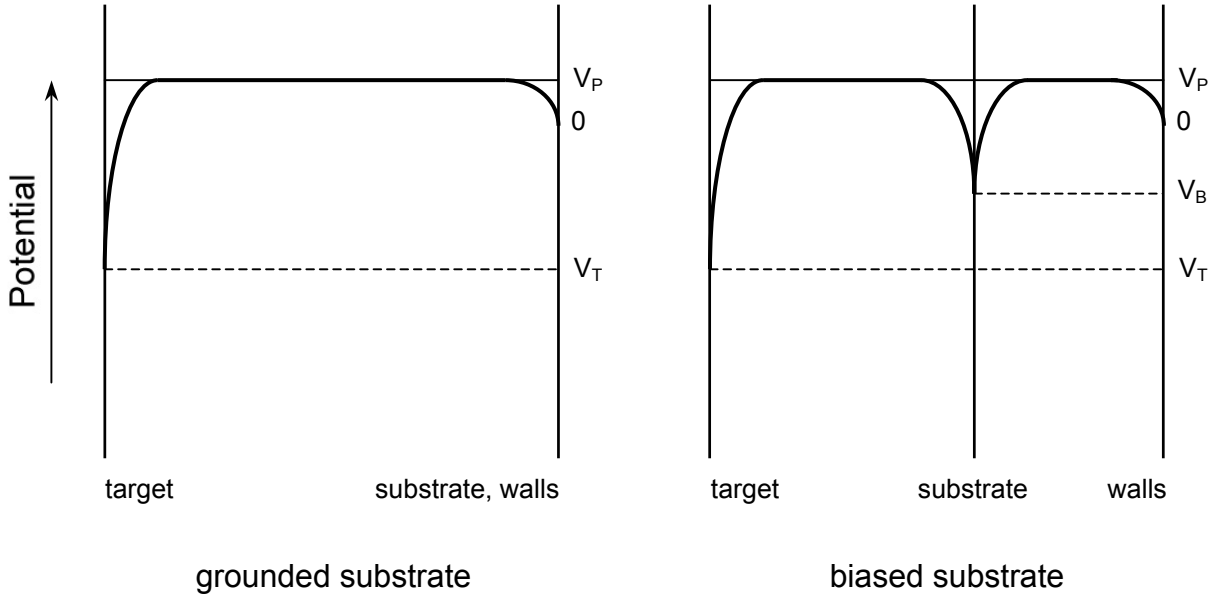

Fig. 2.2. Potential distribution in the deposition process with grounded and biased substrate.

2.1.1. "Target poisoning" problem

In our combined MS/PACVD of noble metals-containing *a*-C:H, we used a magnetron capped with a noble metal target, operating in the mixture of argon and methane. As usual, argon is used for target sputtering, while CH_4 was a source of carbon and hydrogen for *a*-C:H. All noble metals are characterized with high sputtering yield that is, the number of ejected atoms per one impinging argon ion/atom [72,73]. In operating such, so-called "soft" targets in Ar/CH_4 mixture, one faces a difficulty that is colloquially named *target poisoning*, and is the progressive target covering by carbon atoms during the deposition process. This effect was already encountered by Gampp [26] in *a*-C:H/Au deposition. If not kept under control, deterioration of the state of target (in terms of carbon coverage) causes decrease of the deposition rate during single deposition process and non-uniformity of the obtained film. A good sense of this effect one gets observing the target outside of the deposition chamber, after some time of operation in Ar/CH_4 mixture – it contains firmly embedded carbon, easily noticeable as black inclusions.

We started with the study of this problem using Au target, and more detailed results are given in Ref. [74]. Here we will give only two graphs to depict the difficul-

ties one meets working with this kind of target material. Figure 2.3 shows Au content in the deposited *a*-C:H/Au thin film determined by x-ray photoelectron spectroscopy (XPS, see Paragraph 2.2.1), as a function of RF plasma operating time, for three different mass flow ratios of argon and methane. In this experiment a magnetron capped with gold target of 25 mm in diameter is used and aluminum substrates are kept grounded. One notices that behavior of the deposition at three values of Ar/CH_4 mass flow ratio, which do not differ too much, is significantly different. At Ar/CH_4 = 0.67, one cannot reduce the Au content in the film even after 3 hours of plasma operating time. On the other hand, Ar/CH_4 = 0.43 results in almost immediate target poisoning and fast reduction of Au content in the deposited film (see Fig. 2.3). The intermediate, most interesting case of Ar/CH_4 = 0.54 shows that Au content remains high in the beginning, and then an abrupt deterioration of the target state by carbon coverage and Au content decrease takes place. That leads to the low Au concentrations in the film in a very short time compared to the total time of plasma operation.

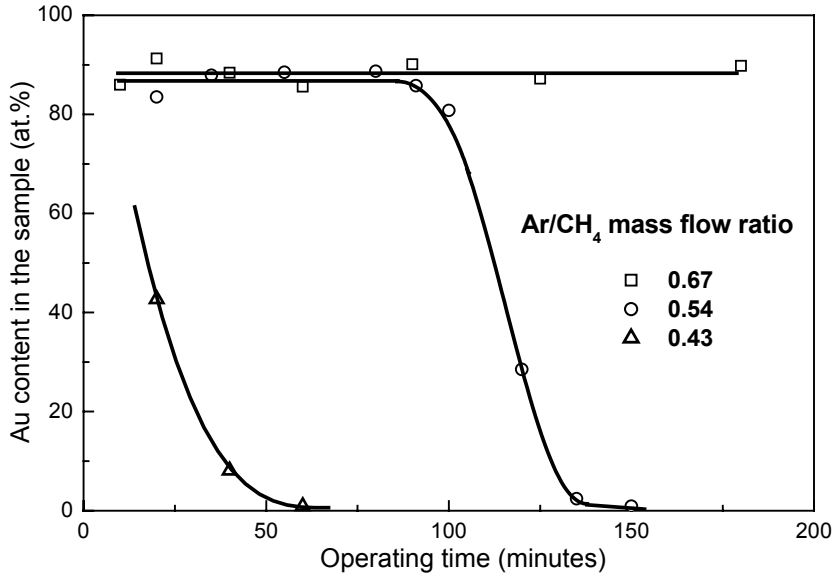

Fig. 2.3. The gold content in deposited a-C:H/Au films on grounded substrates vs. total RF plasma operation time, for different Ar/CH_4 mass flow ratios. Lines are guides to the eye.

Figure 2.4 shows a comparison of the Au content in the films obtained on grounded substrates in entirely different conditions: a magnetron capped with 25 mm diameter Au target was driven by 15 W RF power at a mass flow ratio Ar/CH_4 = 0.54, while the other one, capped with 90 mm diameter Au target is powered with 20 W BPP dc power (see details in Section 2.3) at a mass flow ratio Ar/CH_4 = 0.43. One notices that target poisoning exists and shows similar abrupt character regardless of the type of magnetron and power. In the latter case, the step of target deterioration takes place after longer operation time. That evidences on its origin in carbon coverage of the target: even in the atmosphere with higher CH_4 content, the larger area of the second magnetron target takes more time to get covered by carbon, and reach critical state when abrupt decrease of Au content takes place. In the same figure, the

nominal deposition rate (measured by a quartz crystal monitor, for unity density) in both cases is given. It shows monotonous decrease throughout the measurement. That implies that neither of these two regimes is actually convenient for thin film deposition. In our experiments, the results of which will be given in the following chapter, we have established such an Ar/CH_4 mass flow ratio (1.5, see Section 2.3), which provides dynamical equilibrium between target covering by carbon and cleaning by argon, and thereby – a constant deposition rate.

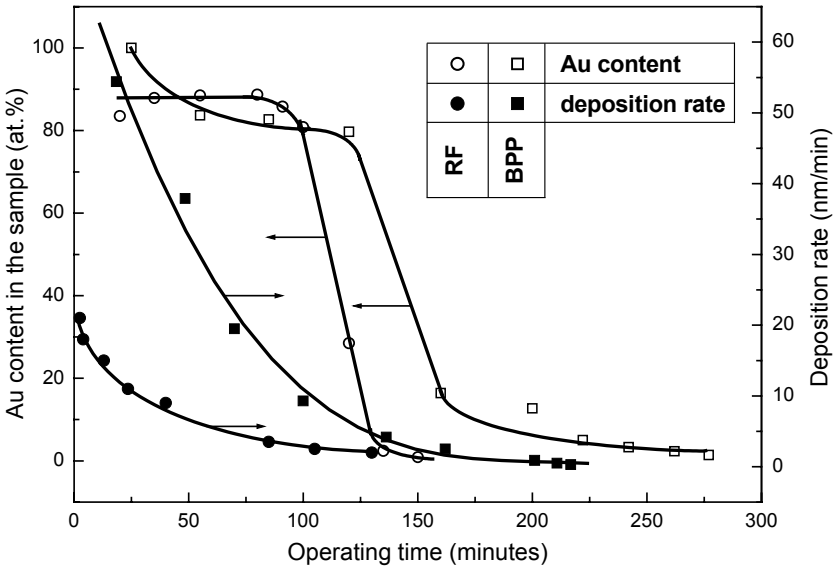

Fig. 2.4. Comparison between time dependencies of Au content in deposited film and nominal deposition rates in processes run by RF (∅ 25 mm target, P = 15 W, Ar/CH_4 = 0.54) and dc BPP (∅90 mm target, P = 20 W, Ar/CH_4 = 0.43) powered magnetrons. Arrows refer to appropriate ordinate axis. Solid lines are guides to the eye.

2.2. Surface characterization of thin films

2.2.1. Photoelectron spectroscopy (PES)

Photoemission, the effect of electron extraction from the solid surfaces exposed to the electromagnetic radiation, is first detected by Hertz in 1887 [75]. Followed by several experimental improvements by Thomson [76] and Lenard [77-79], the phenomenon is first explained by Einstein in 1905 [80], introducing the quantum nature of the light. That enabled today familiar picture of the photoeffect: the irradiated atom in the solid material releases an electron following the formula

$$h\nu + A \rightarrow A^+ + e^- \qquad (2.1)$$

Energy conservation yields:

$$h\nu + E(A) = E(A^+) + E_{kin}(e^-) \qquad (2.2)$$

or, for the kinetic energy of emitted electron

$$E_{kin} = h\nu - [E(A^+) - E(A)] \quad (2.3)$$

If we denote the term in brackets as *binding energy (BE)*, E_B, we obtain:

$$E_{kin} = h\nu - E_B \quad (2.4)$$

Calculating binding energy with respect to the Fermi level, E_F, the above equation requires a small correction – the *work function*, ϕ, the energy that has to be invested so that free electron leave the solid material reaching the *vacuum level*, E_{vac}:

$$E_{kin} = h\nu - E_B - \phi \quad (2.5)$$

What happens with electrons ejected from the atomic inner closed shells (core levels) and outer, valence band, is schematically depicted in Fig. 2.5. [81] The photoemission actually brings out to the observer the image of the inner electronic structure of an atom. A detailed quantum-mechanical approach to the photoemission can be found in several books dealing with this phenomenon [81-84]. For sake of clarity of further considerations, here should be noted only that after photoemission an atom is

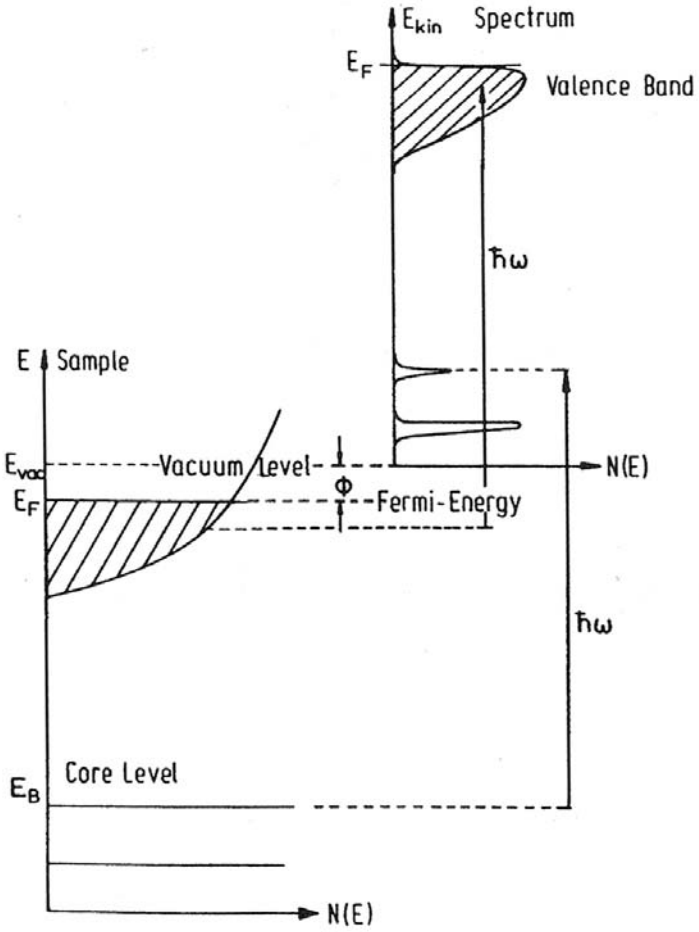

Fig. 2.5. Schematic diagram of the energy levels of the atom in the sample and its “image” in the photoelectron spectrum after the electromagnetic irradiation [81].

ionized, i.e. in the state with (N–1) electrons. It introduces complexity in energy spectrum. The most obvious consequence is spin-orbital (LS) coupling in closed inner shells: the remaining unpaired electron can have spin either parallel (½) or antiparallel (-½) to its orbital momentum l. Therefore, two final states with different energy are possible, characterized by total quantum number $j = l \pm ½$ and giving rise to two peaks, separated in energy. Usual notification of electrons in photoelectron spectroscopy is

$$nl_j$$

where n is the main, l - the orbital, and j – the total quantum number. According to the convention, orbital quantum numbers are replaced by letters for shells (s, p, d, f) and notification is preceded by a symbol of an element of electron origin, e.g.

$$\text{Ag } 3d_{5/2}.$$

As implies from Fig. 2.5, to be able to observe the inner structure of an atom, one has to be equipped with a dispersion element, capable to distinguish electrons by their kinetic energy and yield – an electron energy spectrum. Almost a century after the Hertz's discovery, that was achieved by the group of Prof. Siegbahn from the Uppsala University in Sweden [85,86], by employing hemispherical electron analyzer. This discovery opened new opportunities in solid-state research, and was extensively exploited and developed in the following years, reaching nowadays. Having an electron analyzer and an excitation source, one may obtain a *photoelectron spectrum (PES)*. To extract electrons from the inner shells, excitation photons of the order of 1000 eV has to be employed, falling into soft x-rays region. For this purpose most often are used Mg Kα (hν = 1253.6 eV) and Al Kα (hν = 1486.6 eV) lines. In this way, one obtains the *core-level*, or *x-ray photoelectron spectrum (XPS)*. Extracting valence electrons from an atom requires lower energy ultra-violet photons, and employs most frequently the vacuum-UV lines from the neutral and single-ionized helium, He I, hν = 21.22 eV, and He II, hν = 40.80 eV, respectively. This results in the *valence-band*, or *UV photoelectron spectrum (UPS)*.

For PES measurements in this work, a hemispherical electron analyzer SPECS EA 10 is used, which will be briefly described here. The cross-section schematics of the analyzer is given in Fig. 2.6. It consists of two concentric hemispheres with radii of 114 mm and 80 mm of the outer and inner one, respectively. The entrance and exit slits are centered at the mean radius of 97 mm. Electron arriving to the entrance slit can pass the full deflection angle to the exit slit only with certain kinetic energy. Electrons emitted from the sample after x-ray or UV excitation, are accelerated or decelerated by the two-stage electrostatic lens system. At the exit slit which, together with entrance slit makes an additional focusing stage, a multichannel detector (MCD) with 18 discrete channels is mounted, counting the number of arriving electrons and converting it into voltage signal. The electron energy spectra are created by scanning the analyzer system over the range of excitation photon energies. This can be achieved by changing the voltage between the hemispheres. In this

case, all electrons arrive to the entrance slit with their "original" energy, decelerated with same fixed factor. This mode of operation is called *constant retardation ratio* (CRR). Another way of scanning is to keep the voltage between hemispheres, i.e. the "pass energy" constant, and to use the electrostatic lens system to accelerate/decelerate all electrons to that fixed value. This mode is known as *constant analyzer energy* (CAE). Traditionally, UPS measurements are done in the CRR, and XPS in the CAE operation mode.

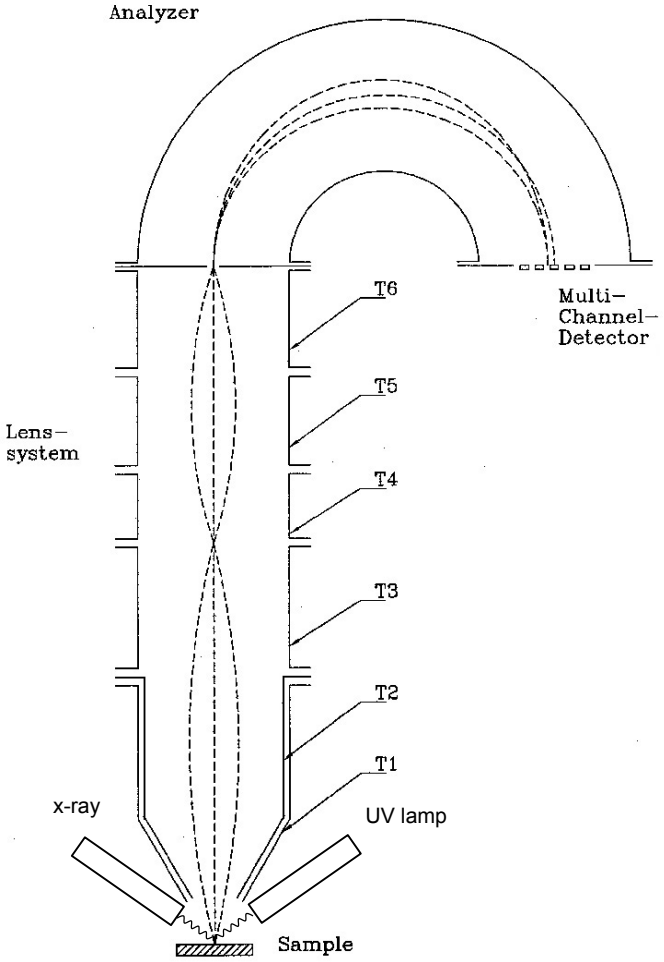

Fig. 2.6. Cross-section diagram of the SPECS EA 10 hemispherical electron analyzer, the system of electrostatic lenses, and the excitation sources.

The photon sources are UV lamp, operating in helium flow at 10^{-5} mbar for He I (21.22 eV) and at 10^{-6} mbar for He II (40.82 eV) excitation of the valence band, and a Mg-Kα x-ray source (1253.6 eV) for the core-level excitation. The spectral resolution of the spectrometer, measured as the full width at half maximum (FWHM) of the Ag $3d_{5/2}$ core-level signal is 0.93 eV.

In experimental photoelectron spectroscopy most results are given in binding energies, with respect to the Fermi level. The Einstein's equation of photoeffect (2.5) is therefore rewritten as:

$$E_B = h\nu - E_{kin} - \phi \qquad (2.6)$$

Here should be noted that in practical purposes would be very inconvenient to measure the binding energy with respect to the vacuum level of a sample. That would require the knowledge of the work function of each sample – practically impossible and mostly unnecessary task. The electrical contact between sample and spectrometer equalizes Fermi levels of the two [84], and Fermi level of a sample occurs always at the same energy, declared as zero binding energy. The kinetic energy that spectrometer actually measures is the energy with respect to the vacuum level of spectrometer, i.e.

$$E_B = h\nu - E_{kin} - \phi_{sp} \tag{2.7}$$

The work function ϕ_{sp} of our spectrometer is 4.4 eV.

Already in the early stages of exploiting PES as a tool of characterization of solid samples, it became clear that the escape depth of photoelectrons, and hence the information depth is very small [87]. In the solid sample, electrons ejected from atoms loose their energy in several ways: by excitation of the plasmons (collective oscillation mode of conductive electrons), excitation of valence electrons, and ionization of core levels. All these contributions results in very small electron mean free path in solids. Figure 2.7 shows the electron mean free path as a function of ejected electron energy (that is, above the Fermi level) [88]. Most experimental results show that, in the range of energies applicable for PES, electron escape depth is of the order of 1 – 2 nm. The hollow points on the theory "universal" curve in Fig. 2.7 are energies of He I, He II and Mg Kα excitation that we apply in our experiments,

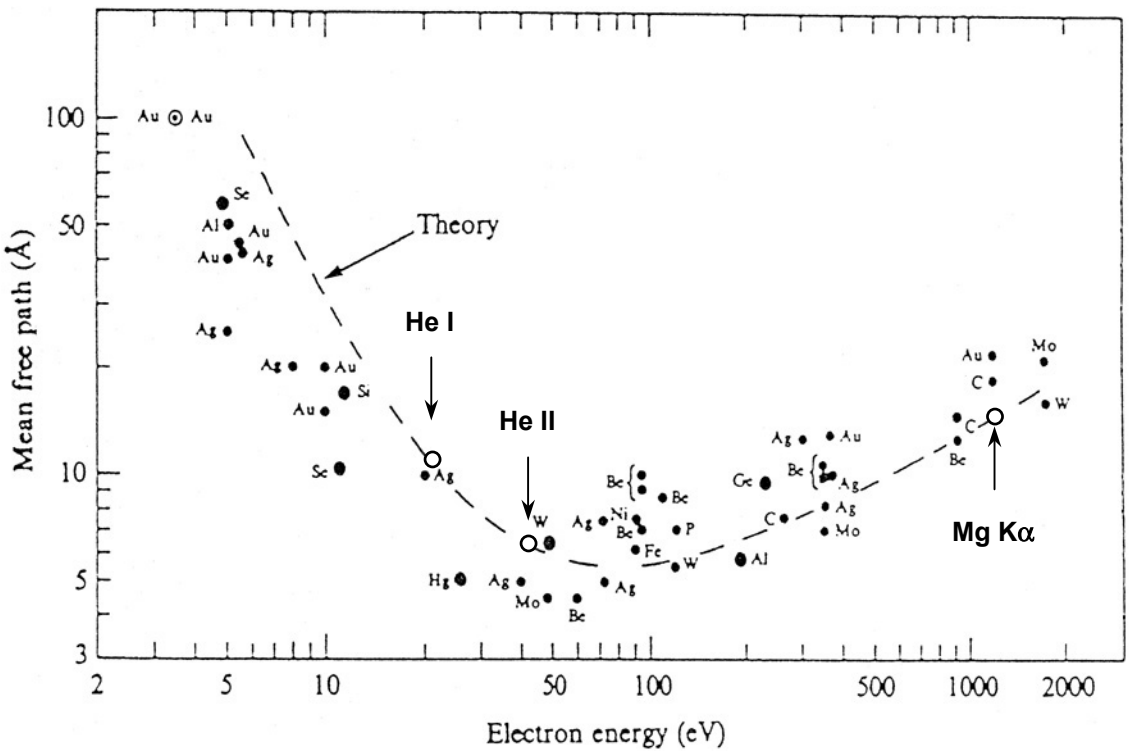

Fig. 2.7. Electron mean free path in solids vs. ejected electron energy. Hollow circles on the theory curve are values of characteristic PES excitation energies, i.e. maximal electron E_{kin}.

representing maximal kinetic energy that ejected electrons can carry, excited with respective photons. Mean free path is, however, a statistical value and is not equal to the maximum depth which we may obtain information from. It is regarded that maximal information depth is about triple value of the mean free path. Therefore, PES information can be extracted from about 6 – 7 nm below sample surface. If we take into account that thickness of a monolayer is about 2 – 2.5 Å, that means that PES can access first about 30 monolayers in maximum. This exclusive *surface sensitivity* turned out to be one of the most powerful characterization tools in surface chemistry.

The strength of this method lies in the possibility to measure quantitatively relative concentrations of the elements contained in the sample. Following the considerations of Schüler *et al.* [89], the relative electron concentration $[X]_{rel}$ of element X can be calculated as

$$[X]_{rel} \sim I \cdot E_{kin}^{0.43} / \sigma \qquad (2.8)$$

where I is the integrated area of a core-level peak after subtracting a Shirley background [90], and σ is the appropriate electronic shell photoionization cross-section of element X [91]. In this way, the stoichiometry of the sample surface can be determined.

Another important feature of XPS is the *chemical shift*. Namely, core-level binding energy positions are actually the “fingerprints” of each element in the periodic table. If elements are included into chemical compounds, their binding energies are slightly changed, and hence, their core-level peaks are shifted.

Altogether, the surface sensitivity, the stoichiometry determination ability, and the sensitivity to the oxidoreduction state makes the photoelectron spectroscopy powerful tool in surface chemistry. That was already recognized by Siegbahn, who named the new technique *Electron Spectroscopy for Chemical Analysis – ESCA* [85,86].

2.2.2. Surface characterization by PES

In samples prepared in the course of this work – noble metal nanoclusters containing *a*-C:H, one does not expect any chemical interaction between carbon in the *a*-C:H matrix and gold, silver or copper. Hence, the chemical shifts are not expected either. That opens a possibility of using PES, apart from the basic relative concentration measurements, for the study of surface structure and nanocluster arrangement.

As already pointed out in the introductory chapter, the aim of this work was to study the arrangement of nanoclusters within first few monolayers of these samples. The primary task was to reveal whether the topmost clusters are fully or only partially embedded into dielectric *a*-C:H matrix. In other words, are the topmost metallic clusters at the surface bald or not?

If there are no chemical shifts due to chemical reaction between the dielectric matrix and metallic inclusions, photoelectron spectroscopy can, in principle, offer an answer to this question by employing so-called *approximation of spherical capacitor and one-electron charging* [26,89]. In this approximation, metallic nanocluster is regarded as a spherical capacitor of radius *R* that looses one electron only in the photoemission process. The capacitor becomes charged positively with unit charge *e*. The energy of charged capacitor is:

$$E_C = \frac{1}{4\pi\varepsilon_0\varepsilon}\frac{e^2}{R}, \tag{2.9}$$

where ε_0 the is dielectric permittivity of vacuum and ε – the relative dielectric permittivity (dielectric constant) of the capacitor surrounding. The kinetic energy of the escaping electron will be therefore reduced, i.e. its binding energy shifted from the bulk metal to the higher values for the amount of E_C. Two factors influence E_C: the size of the cluster, i.e. its radius *R*, and the dielectric constant of the surrounding environment ε. Regarding the arrangement of the clusters at the sample surface, the problem is schematically depicted in Fig. 2.8. According to Eq. (2.9), the smaller the cluster size is, the higher E_C, i.e. binding energy of the escaped electron will be. On the other hand, fully embedded cluster (Fig. 2.8.a) is surrounded with the dielectric with relative permittivity ε. For partially embedded cluster, an effective dielectric constant, $\varepsilon > \varepsilon_{eff} > 1$ should be considered (Fig. 2.8.b). Therefore, if an isolated metallic cluster structure exists within the dielectric matrix, binding energies of metallic atom core levels should be shifted towards higher values with respect to the bulk metal. If the clusters are bald on the surface, this shift should be even larger.

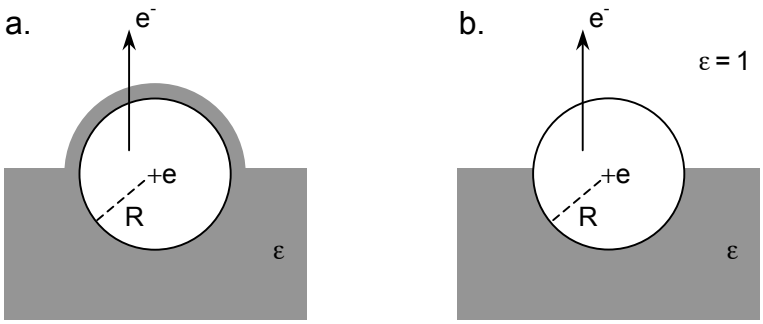

Fig. 2.8. Schematics of the photoemission process from (a) fully and (b) partially embedded metallic cluster in a dielectric matrix.

Another way of revealing surface arrangement is depicted in Fig. 2.9. By tilting the sample for a certain angle, the escaped electrons from the sample are collected by the electrostatic lenses system (represented by the first lens T1 in Fig. 2.9) at *off-normal take-off angle*. If the topmost metallic clusters are covered with a layer of *a*-C:H, increasing the angle Θ should result in XPS in decreasing of the intensity ratio

of metallic core level to the C 1*s*. By tilting the sample, the thickness of the cover *a*-C:H layer is apparently increased for the "observer" T1, and more carbon than metal-originated electrons arrive to the spectrometer (Fig. 2.9.a). On the other hand, by tilting the sample with bald clusters at the surface the beneath-lying *a*-C:H matrix would be "hidden" for the observer, and that should result in increased number of metal-originated electrons at the expense of the carbon ones, and thereby increased intensity ratio of metal to C 1*s* core levels (Fig. 2.9.b).

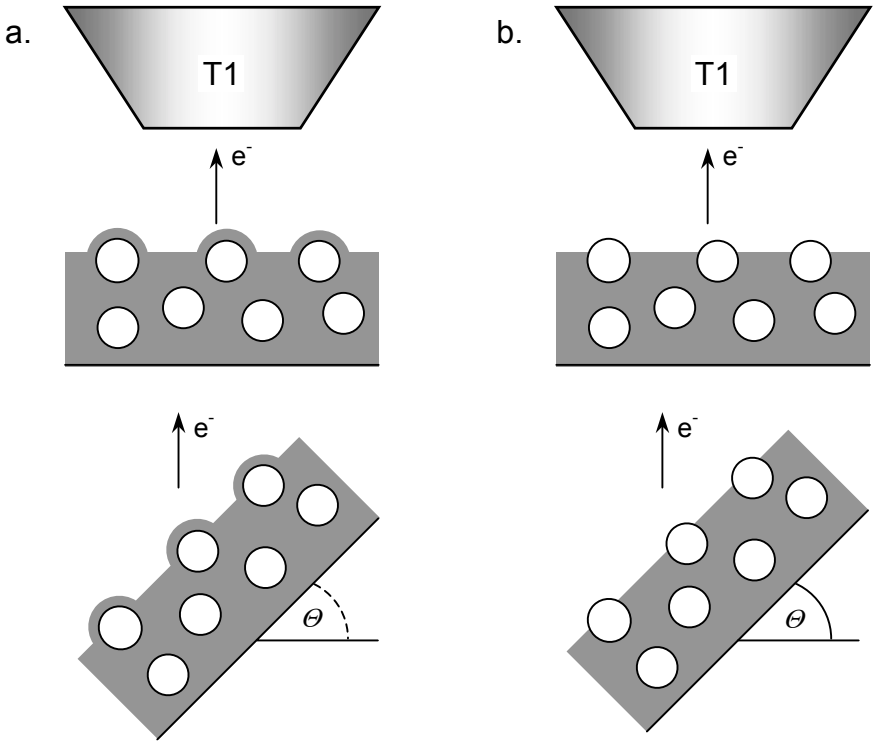

Fig. 2.9. Schematics of the off-normal take-off photoemission from (a) covered and (b) bald topmost metallic clusters in *a*-C:H matrix.

Finally, if topmost clusters are covered with a layer of *a*-C:H, it should be possible, in principle, to "uncover" them by Ar^+ ion bombardment with sufficient energy. Schematics of this experiment is given in Fig. 2.10. In subsequent *in situ* Ar^+ *etching* and XPS measurements, one should observe the increase of the metallic core level intensity with respect to the C 1*s*, as the cover *a*-C:H layer gets thinner. At one point, the topmost clusters should be entirely uncoated, and from that moment onwards, a decrease in metallic core level to C 1*s* intensity ratio should be observed, since further Ar^+ etching erodes metallic clusters as well (Fig. 2.10.a). Again, if topmost clusters are bald on the surface, they should be eroded by Ar^+ bombardment from the very beginning of the etching process and therefore, a monotonous decrease in metallic core level to C 1*s* intensity ratio should be observed throughout the experiment (Fig. 2.10.b).

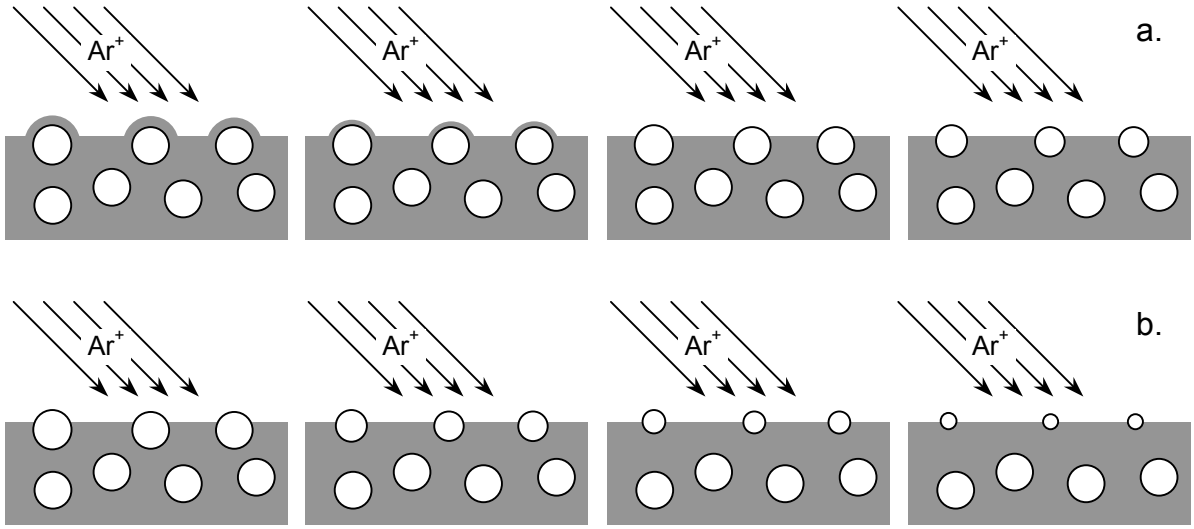

Fig. 2.10. Schematics of the evolution (from left) of the topmost metallic clusters coverage and size with *in situ* Ar^+ ion bombardment: (a) covered and (b) bald surface clusters.

2.2.3 Direct imaging techniques (AFM & SEM)

Following the pioneering work of Binnig *et al.* [92], atomic force microscopy (AFM) took its important place among variety of scanned-proximity probe imaging techniques. AFM works on the principle of an atomically sharp tip that is scanned over a surface. The tip, attached to the bottom side of a reflective cantilever, is driven above the sample surface by means of piezoelectric scanners. A diode laser is focused onto the upper reflective side of the cantilever. As the tip moves up and down with the contour of the surface, the laser beam is deflected off the attached cantilever into a dual element photodiode. The change in light intensity is measured by a photodetector and converted into voltage. In this way, an image of the surface morphology can be obtained with an atomic resolution. Two AFM instruments are used in this work: for *a*-C:H/Au imaging the Topometrix, type Explorer®, and for *a*-C:H/Ag and *a*-C:H/Cu the Digital Instruments, type Dimension™ controlled by Nanoscope® IV unit. In both cases, a tip NCHR-W by Nanosensor in non-contact mode is used.

Another imaging system used in this work is scanning electron microscope (SEM). Operating principle of SEM is based on the bombarding the sample with high-energy electron beam, focused by the system of electromagnetic lenses to a small spot at the sample. Incident electron ejects secondary electrons from the sample, which are collected by the detector. According to the number of secondary electrons collected, a magnified picture of the scanned sample area is created. In this work SEM systems Phillips XL 30 ESEM and Jeol 6300 F are used, both having a resolution of about 2 nm / 20 kV. Since samples of our interest are non- or weakly conductive due to isolated nanocluster structure, to increase the quality of the images, they were coated in commercial sputtering machine with 3 nm of platinum.

2.2.4. Grazing incidence small-angle x-ray scattering (GISAXS)

In the recent past, grazing incidence small-angle x-ray scattering (GISAXS) performed with synchrotron radiation has been developed as a powerful tool to study shape, size, and spatial correlation of buried nanoclusters as well as deposited islands in solid samples [93-95]. In the course of this work, these experiments were performed with the small-angle scattering setup, schematically depicted in Fig. 2.11, of the beamlines 22 (*a*-C:H/Au) and 31 (*a*-C:H/Ag and *a*-C:H/Cu) at the LURE synchrotron facility in Orsay, France. The energy of the x-ray beam at two beamlines was set at 9 keV and 7 keV, corresponding to the wavelengths of 0.138 nm and 0.177 nm, respectively. The beam size was 1×0.1 mm^2 (width and height, respectively). The angle of incidence was kept constant, about 0.1° above the critical angle for total external reflection, so that the penetration depth of the x-ray beam was approximately 120 nm. The GISAXS patterns were recorded with an imaging plate employed as a 2-dimensional detector for the *a*-C:H/Au samples, and replaced with advanced CCD camera for the measurements on *a*-C:H/Ag and *a*-C:H/Cu samples. As a result, on the detector one obtains GISAXS pattern. Each point in the 2-dimensional pattern is determined by its scattering vector $\vec{q}$ that can be decomposed as: $\vec{q} = \vec{q}_y + \vec{q}_z$, where $\vec{q}_y$ and $\vec{q}_z$ are the horizontal and vertical components, respectively, and $|\vec{q}| = q = (4\pi/\lambda)\sin\theta$, where θ is the scattering angle. GISAXS pattern can be analyzed using traditional Guinier plot [96], that yields in-plane diameter and the height of clusters, as well as intercluster distance in-plane and in the growth direction. By employing local monodisperse approximation, from the GISAXS patterns one may obtain additional information on the cluster size distribution both in the film plane and growth direction [35]. In this way, GISAXS represents complementary tool to the direct imaging techniques. Moreover, it provides information on the in-depth cluster dimensions, the data that are inaccessible with AFM, and require complicated preparation of cross-section transmission electron microscopy (TEM) specimens.

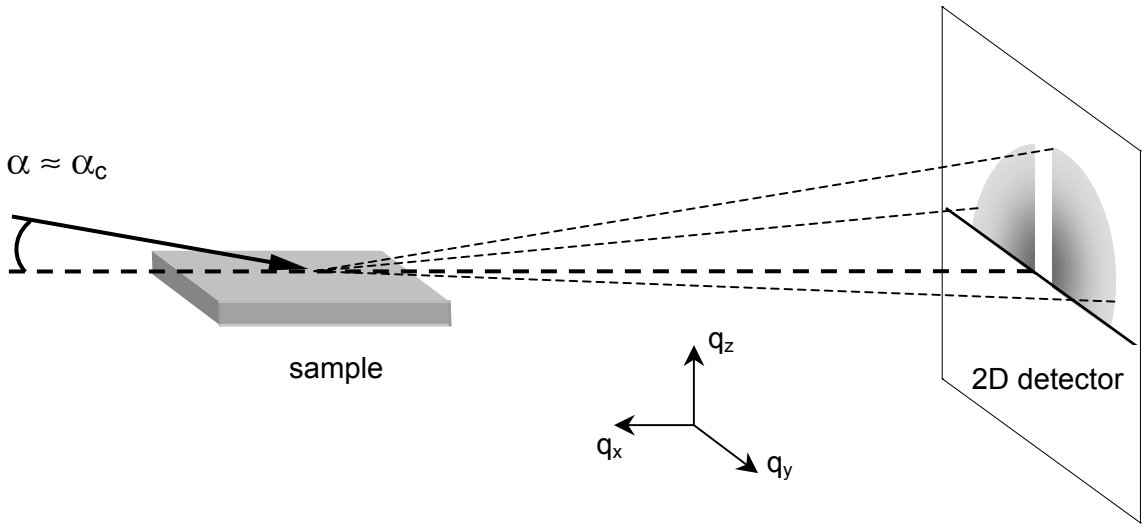

Fig. 2. 11. Experimental setup for small-angle grazing incidence x-ray scattering (GISAXS).

2.3. *In vacuo* thin film deposition – PES measurement system

The surface sensitivity of the PES technique, i.e. the fact that the information is obtained from the first several monolayers of a sample, puts one before the problem of sample exposure to the air. With non-reactive deposits (like *a*-C:H/Au and *a*-C:H/Ag in our case), it results in formation of native oxide at the surface, while samples that interact with oxygen (like copper in our *a*-C:H/Cu) faces even more serious alterations by oxidation. To obtain information from "as deposited" material, the requirement of avoiding sample exposure to the air between deposition and PES measurement should be met. It was achieved by our laboratory made *in vacuo* thin film deposition – PES measurement system. The schematics of the entire setup is given in Fig. 2.12. A stainless steel deposition chamber of 60 cm in diameter and 30 cm in height can be pumped down below 10^{-6} mbar using a conventional rotary–turbomolecular pumping system. Argon and methane are fed into the chamber via two mass flow controllers. For all our experiments, Ar/CH_4 mass flow ratio of 1.5 (6 sccm Ar / 4 sccm CH_4 for *a*-C:H/Au, and 24 sccm Ar / 16 sccm CH_4 for *a*-C:H/Ag and *a*-C:H/Cu) was selected. This mass flow ratio value showed to be the one which mostly reduces the target poisoning effect (see Paragraph 2.1.1). The total gas pressure in the chamber is controlled by a throttling valve and kept at about 6×10^{-3} mbar during the deposition. To run the plasma, a water-cooled magnetron, capped by a 90 mm diameter target is driven by bipolar-pulsed dc power at 50 kHz. The schematics

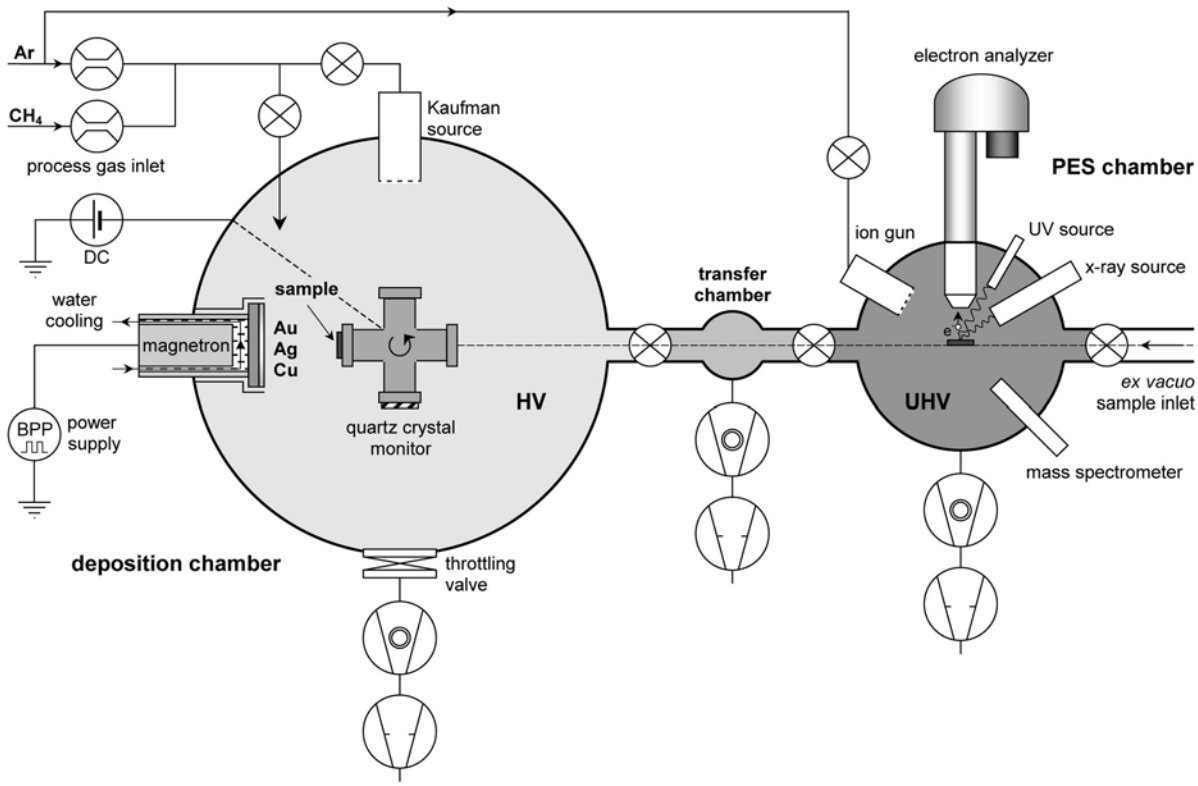

Fig 2.12. Schematic diagram of *in vacuo* thin film deposition – PES measurement system.

of the powering voltage cycles is given in Fig. 2.13. Short positive pulses of 1056 ns duration are used to accelerate electrons towards the target, thus discharging positively charged poisoned regions of the target, without loosing too much of operating negative powering.

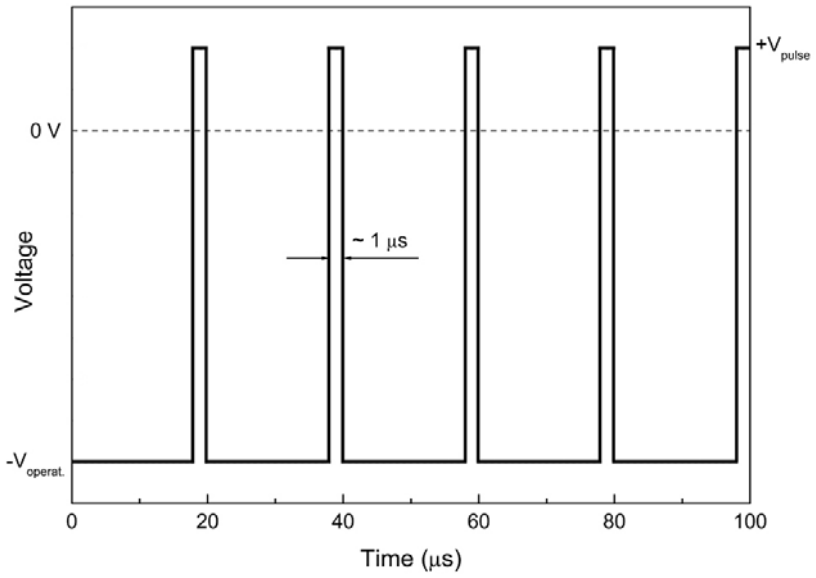

Fig. 2.13. Schematics of the powering cycles of the bipolar-pulsed power supply.

The targets used were Au, Ag, Cu, or graphite (for pure *a*-C:H deposition). For *in vacuo* PES measurements, the aluminum substrates are used, pretreated by ultrasonic cleaning in acetone and ethanol. Besides, the deposition chamber is equipped with a Kaufman-type ion source (ION TECH, MPS–3000 FC), which was employed to remove the oxide layer from the substrate surface by Ar^+ ion bombardment. Moreover, an efficient Ar^+ ion surface cleaning enables multiple usage of the same substrate. For *ex vacuo* measurements, Si (100) wafers of 0.5 mm thickness and 40–70 Ωcm resistivity are used as substrates, also subjected to the acetone and ethanol, but not to the Kaufman-source pretreatment. The cross-shaped holder (see Fig. 2.12) has four sites for mounting different kinds of substrates or substrate holders. Via the rotating vacuum feedthrough, it can be manually turned in order to face the sample to different devices: the magnetron, the Kaufman source, or the connecting path to the transfer chamber. When a substrate faces magnetron target, the distance between the two is about 10 cm, except the case of graphite target when, due to low sputtering yield [72,73], the distance was reduced to about 4 cm. On one of the sites the quartz crystal monitor is mounted to control the deposition rate. Before the deposition, the plasma in the chamber should be run for a while to achieve stability of deposition parameters. The substrate holder can be biased at desired voltage. In our experiment, we have kept the substrate holder either grounded, or biased at –150 V dc (by means of Advanced Energy, MDX power supply). Since that was the parameter that determined majority of film properties throughout this work, in the further text we

shall use the terms *grounded* and *biased* to denote samples deposited without and with substrate bias voltage, respectively. To avoid surface charging effects, the thickness of the deposited coatings for PES studies was between 10 and 20 nm. Here should be also noted that grounded and biased samples are obtained in subsequent depositions in order to diminish the target poisoning effect and changes in the stoichiometry of the deposited coatings. To ensure this, after deposition of biased probes (which were themselves deposited immediately after the grounded ones), another grounded samples are made and their stoichiometry crosschecked by XPS. The differences in obtained metal concentrations did not exceed 0.5 at. %. Therefore, we made sure that the differences encountered in grounded and bias samples originate exclusively in applying substrate bias. These differences will be shown in metal concentration, surface morphology and topmost clusters coverage. To emphasize this, the samples that are obtained in subsequent depositions and differ in substrate bias voltage *only* we will denote as *counterparts*. If not specified otherwise, wherever we simultaneously present data of grounded and biased samples, these will be – the counterparts. Here should be also noted that temperature measurements during deposition, using a thermocouple attached to the substrate holder, did not encounter any change from the room temperature on either grounded or biased substrates.

For *in vacuo* measurements, the samples were transferred from the deposition to the electron spectrometer ultra-high vacuum (UHV) chamber without breaking the vacuum, via an intermediate and independently evacuated chamber with a base pressure of about 1×10^{-7} mbar, see Fig. 2.12. The base pressure in the PES measurement chamber is about 1×10^{-10} mbar. All measurements that will be presented in the following chapter are made *in vacuo*, unless otherwise specified. For the reference measurements, Au, Ag, and Cu monocrystalline samples are used, pretreated by Ar^+ ion sputtering using Penning source. The calibration is made upon the Au $4f_{7/2}$ signal at 84.0 eV, Ag $3d_{5/2}$ at 368.3 eV, and Cu $2p_{3/2}$ at 932.7 eV binding energies [97]. In this work, for UV He I and He II valence band spectroscopy data acquisition, we used the constant retardation ratio mode of electron analyzer with a retardation value of 3. For core-level spectroscopy, the constant analyzer energy mode is used with pass energies of 50 eV for survey spectra (1000 eV – 0 of binding energy) and 30 eV for Au $4f_{7/2}$, Ag $3d_{5/2}$, Cu $2p_{3/2}$, C 1*s*, Ar 2*p* and S 2*p* core levels. For data acquisition and relative atomic concentration determination (see Paragraph 2.2.1) of elements in the samples, the commercial SpecsLab software is used. Beside the electron analyzer and excitation sources, the UHV chamber is equipped with scanning ion gun, which enables one to make *in situ* in-depth analysis by alternative sample etching and PES recording. The ion source was kept at the dynamical pressure of 10^{-6} mbar. The Ar^+ ions with 1 keV kinetic energy were used, a value which showed to remove the topmost sample layers reasonably slow to enable meaningful subsequent PES measurements (see Paragraph 2.2.2).

3. Results and comparative discussion: *a*-C:H/Au, *a*-C:H/Ag, and *a*-C:H/Cu

3.1. Series of a-C:H samples with different noble metals concentration studied by XPS and UPS

We begin the survey of the results with series of *a*-C:H/Au, *a*-C:H/Ag, and *a*-C:H/Cu samples with different atomic concentration of noble metals, starting from low concentrations and ending with 100 at.% monocrystalline reference metal samples. The substrates were kept grounded during the deposition. This kind of study for *a*-C:H/Au has already been made by Gampp [26], and here this system is revisited for the sake of completeness of the 1B group of transition metals. Figure 3.1 shows normalized core-level spectra of Au $4f_{7/2}$ and C 1*s* in *a*-C:H/Au, Ag $3d_{5/2}$ and C 1*s* in *a*-C:H/Ag, and Cu $2p_{3/2}$ and C 1*s* in *a*-C:H/Cu. Regarding metallic core levels, in all three systems one notices that, starting from about 40-50 at.% (percolation threshold, see [99]) downwards to the lower concentrations, shifts toward higher binding energies (BE) are observed. In apparent absence of chemical shifts, we can correlate these shifts to the metallic cluster size, as described in Paragraph 2.2.2. Assuming (at this point in the first approximation) that surface clusters are fully embedded in the *a*-C:H matrix and substituting constants in Eq. 2.9, we obtain for the cluster diameter:

$$D\,[\mathrm{nm}] = \frac{2.876}{\varepsilon\,\Delta E_B\,[\mathrm{eV}]} \tag{3.1}$$

where ΔE_B is the positive shift (towards higher values) in binding energies from the reference, equal to E_C in Eq. 2.9. Taking the value of dielectric constant of *a*-C:H approximately equal to the one of diamond ($5.66 \le \varepsilon \le 5.87$, [98]) the cluster diameter in the *a*-C:H matrix can be estimated as:

$$D\,[\mathrm{nm}] \approx \frac{0.50 \pm 0.01}{\Delta E_B\,[\mathrm{eV}]} \tag{3.2}$$

For nearly equal metallic concentrations in nanocomposites one roughly estimates the mean cluster diameters as follows:

a-C:H/Au	8.6 at.%	ΔE_B = 0.11 eV	$D \approx 4.5$ nm,
a-C:H/Ag	9.8 at.%	ΔE_B = 0.18 eV	$D \approx 2.8$ nm,
a-C:H/Cu	8.6 at.%	ΔE_B = 0.53 eV	$D \approx 0.9$ nm.

The sample of *a*-C:H/Cu 8.6 at.% is shown later, in Fig. 3.12. These values may be underestimated by neglecting possible cluster partial, instead of full embedment into *a*-C:H matrix. However, it is obvious that cluster size decreases from Au to Cu.

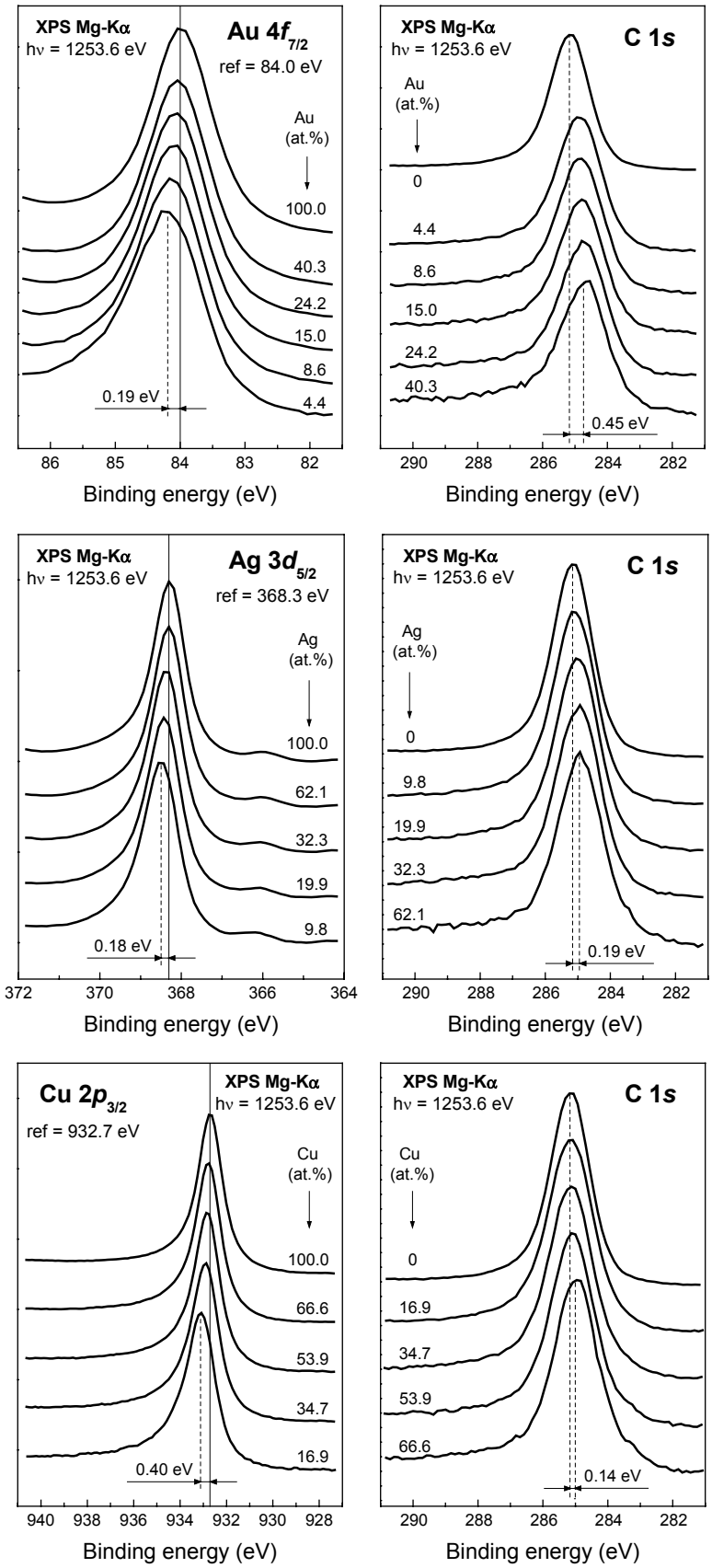

Fig. 3.1. Normalized core-level spectra of Au $4f_{7/2}$ and C 1*s* in *a*-C:H/Au, Ag $3d_{5/2}$ and C 1*s* in *a*-C:H/Ag, and Cu $2p_{3/2}$ and C 1*s* in *a*-C:H/Cu with different metallic contents. Substrates were kept grounded. Vertical solid lines mark the reference binding energy positions.

Carbon core level, C 1*s*, shows in all cases decrease in binding energy with increasing metal content in the film. Before further discussion, it should be noted that the opposite direction of the C 1*s* shift in comparison to the metal core levels proves that charging effects are absent in our measurements.

The behavior of the C 1*s* core level and its correlation with sp^2-coordinated (graphitic-like) and sp^3-coordinated (diamond-like) bonds, and the sp^2/sp^3 ratio in amorphous carbon films is of significant importance regarding hardness and conductivity of the coatings. It is generally regarded that harder *a*-C films have higher amount of sp^3-coordinated carbon, whilst softer and more conductive coatings contain more sp^2 bonds between carbon atoms [100-103]. Therefore, structural problem of carbon-based thin films is studied by number of authors. First treatment of DLC, graphite and diamond by joint XPS of C 1*s* and x-ray excited Auger electron spectroscopy (XAES) of C KLL peak was made by Mizokawa *et al.* [104]. It was followed by Lasovich and coworkers [105,106], who studied several ion-beam sputtered *a*-C and *a*-C:H samples and established the correlation between the binding energy of C 1*s* core level, the C KLL first-derivative XAES, and the sp^2 content, by comparing sputtered samples with diamond and carbon references. In addition, they observed the influence of low-energy Ar^+ ion bombardment to the structure of the coatings. Díaz *et al.* [102] and Mérel *et al.* [107] studied *a*-C samples obtained by pulsed laser deposition technique. This type of analysis is extended also to polymer materials [108]. Recently, Lu and Komvopoulos reported on the sp^3 content revealed by XPS and XAES applied to the nonmagnetron RF-sputtered *a*-C [109]. Using UV and x-ray excited valence band spectroscopy, the annealing-induced structural properties of ion-beam sputtered *a*-C:H films have also been studied by Oelhafen and Ugolini [110]. Similar PES results, together with electron energy loss spectroscopy (EELS) and Raman spectroscopy of electron beam evaporated *a*-C on substrates with elevated temperatures are obtained by Schelz *et al.* [111]. PES studies of the structural changes in electron beam evaporated *a*-C and CVD-obtained diamond film are reported by Reinke and collaborators [112,113].

In the light of the above studies, we believe that the shift of the C 1*s* core level to the lower binding energies, Fig. 3.1, is due to the disorder induced by compression stress that metallic inclusions introduce into *a*-C:H. This stress gets higher as metallic content increases [114] and is reflected in diminishing sp^3 bonds, increasing therefore sp^2-coordinated carbon content in the matrix [115,116]. The large difference in C 1*s* shift between *a*-C:H/Au and other two systems can be a result of high mobility of Ag and Cu atoms, which, contrary to Au, easily diffuse through the matrix and on the surface, thereby reducing the stress-induced potential energy. However, the increasing negative BE shift in C 1*s* core levels with increased metallic content can be also attributed to the progressive reduction of hydrogen content in *a*-C:H matrix [26,114]. Another reason for this effect one may find in possible graphitized layer that is formed at the interface between metallic clusters and *a*-C:H matrix. With increasing metallic content and cluster size, that layer occupies larger volume fraction of the surface region, accessible by PES. This explanation would also put in agreement the

largest C 1*s* negative shift with largest Au clusters revealed earlier from the positive shift of the Au $4f_{7/2}$ core level.

Figure 3.2 shows He I and He II UPS spectra for all three systems under consideration. The spectra are normalized in intensity both within one system, and between different nanocomposites. From reference samples (100 at.%) one notices characteristic features of Au 5*d*, Ag 4*d*, and Cu 3*d* bands in He I spectra. In the Au 5*d* pronounced features are broad peaks at 2.6 eV and 4.4 eV, and a narrow peak at 6.1 eV with shoulder at about 7.3 eV. A broad 4*d* valence band of silver is characterized by three adjacent peaks at 4.5 eV, 5.0 eV, and 5.6 eV, and a narrower feature at 6.2 eV, with shoulder at 6.9 eV. The 3*d* valence band of copper features one peak at 2.4 eV with two shoulders at about 3.1 eV and 4.7 eV. He II spectra generally follows the He I but, due to different excitation energy, the mechanism of excitations of particular features is different, resulting in some of them being more pronounced, and some depressed. A gradual increase of the metallic features in UPS spectra from pure *a*-C:H to the reference monocrystalline metals is observed in Fig. 3.2.

The UPS spectra of pure *a*-C:H (0 at %, Fig. 3.2) feature broad maximum at about 7.5 eV and a shoulder at about 3.5 eV. The former is related to the σ-bonds in tetrahedral sp^3 hybridization and in-plane bonds in sp^2 hybridized carbon. The shoulder at 3.5 eV is related to the weaker π-bonds in sp^2 hybridization. In accordance with C 1s negative BE shift with increasing metallic content that we attributed to the increase of sp^2/sp^3 coordinated carbon ratio, one would also expect the relative rise of the π-states with respect to the σ-states in the valence band. However, with increasing metallic content, the UPS spectra are overwhelmingly dominated by metallic features, some of them being located at the same energies as σ- and π- states of carbon, therefore covering their tiny changes. Nevertheless, it can be noticed that carbon σ-band affects the spectra up to the very high metallic contents, see Fig. 3.2. It is particularly interesting to point out the *a*-C:H/Cu He I spectra: comparing the reference sample (100 at.%) and the sample with just slightly lower Cu content of 95.9 at.%, one already notices the rise of the carbon σ-feature at about 7 eV.

It is interesting to focus on the He II spectra in Fig. 3.2, bearing in mind that He II excitation is the most sensitive mechanism in PES due to the highest photoemission cross section for incident photons of about 50 eV [117]. Comparing *a*-C:H/Ag spectra with the other two, one observes that with the smallest Ag inclusion of 9.8 at. %, the Ag 4*d* band in He II spectrum almost takes the final shape of reference Ag. From the sample of 19.9 at.% onwards to higher Ag contents, no further significant changes up to the reference sample are encountered. For *a*-C:H/Au and *a*-C:H/Cu, more or less gradual increase of characteristic features of valence bands is observed with increasing metal content. The reason for this behavior of silver in *a*-C:H, one may search in known high mobility of Ag atoms even within hard matrices. The results of Ag included in the TiN matrix by reactive co-sputtering are recently reported by de los Arcos *et al.* [118]. The cross-section SEM revealed that within a coating of about 200 nm in thickness, cluster size increased from bottom to the top of the film, while topmost clusters merged to form larger islands [118]. Using GISAXS,

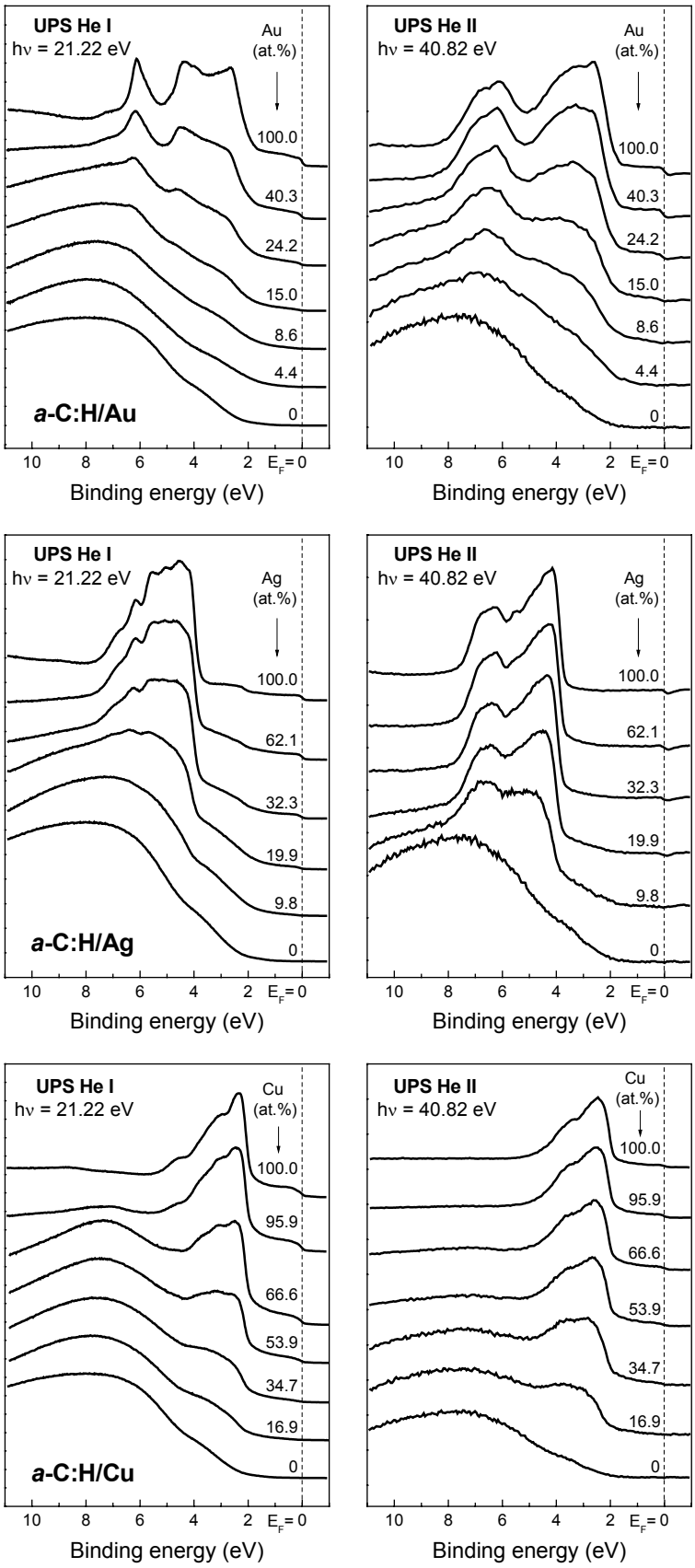

Fig. 3.2. Normalized He I and He II valence band spectra of grounded *a*-C:H/Au, *a*-C:H/Ag, and *a*-C:H/Cu with different metallic content. Zero binding energy denotes the Fermi edge.

Babonneau *et al.* [119] also encountered two families of Ag clusters in ion-sputtered *a*-C/Ag: one of the smaller cluster size in the bulk, and the bigger islands at the surface, induced by surface diffusion. Our He II spectra indicate that the same probably takes place with Ag in *a*-C:H, showing high surface exposure of silver even with small total Ag content. In the further text, we will provide additional evidences on silver agglomeration on the sample surfaces.

The region of special interest in the UPS spectra is the vicinity of the Fermi edge. The step-like drop of the density of states (DOS) in this region is an indication of the metallic nature of the sample. Metals with abrupt DOS drop at the Fermi level, e.g. Au, Pd or Pt, are usually used for the zero binding energy calibration. The enlargement of the Fermi edge region of He I spectra given in Fig. 3.2 is shown in Fig. 3.3. One observes the evolution of the Fermi edge in our nanocomposite systems with metal content rising from zero to 100 at %. The scale on the intensity axis are adjusted to emphasize the “step down” character of DOS in each system approaching 100 at.% of a metal. One notices an advantage of Au regarding the definition of the Fermi edge. The density of states of silver at the Fermi edge is not very high, and the beginning point of the "step down" in DOS of copper is not so well defined. Nevertheless, there are clear shifts in all three systems from the reference-defined zero towards higher BEs. These shifts characterize decreasing metallic character of a sample, and therefore are also related to the shifts in BEs of the metallic core levels in the same direction, see XPS spectra in Fig. 3.1.

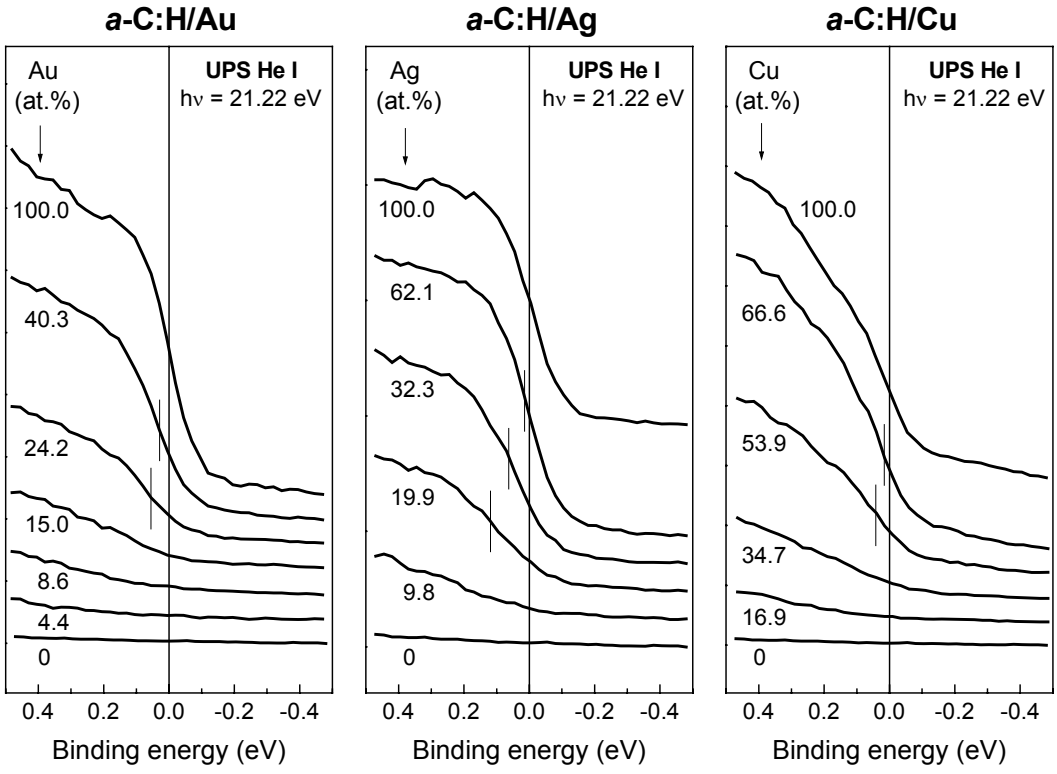

Fig. 3.3. Enlarged Fermi edge region of the He I spectra from Fig. 3.2 of *a*-C:H/Au, *a*-C:H/Ag, and *a*-C:H/Cu with different metallic content.

3.2. Influence of substrate bias voltage on surface morphology and nanocluster arrangement of gold containing amorphous hydrogenated carbon

Reprint:

I. R. Videnović, V. Thommen, P. Oelhafen, D. Mathys, M. Düggelin, and R. Guggenheim, Appl. Phys. Lett. **80** (2002) 2863-2865.

Reprint:

I. R. Videnović, V. Thommen, P. Oelhafen, D. Mathys, M. Düggelin, and R. Guggenheim, Appl. Phys. Lett. **80** (2002) 2863-2865.

Reprint:

I. R. Videnović, V. Thommen, P. Oelhafen, D. Mathys, M. Düggelin, and R. Guggenheim, Appl. Phys. Lett. **80** (2002) 2863-2865.

3.3. Direct imaging techniques (AFM & SEM) results

As implies from Section 3.2, we confine our further considerations to the surface arrangement of nanoclusters in *a*-C:H samples with low metallic content, deposited on grounded substrates and their –150 V dc biased counterparts. Regarding direct imaging techniques applied to our samples, we shall skip the published data given in 3.2, and present AFM and SEM images of low metallic-content *a*-C:H/Ag and *a*-C:H/Cu.

Figure 3.4 shows AFM images of two grounded samples of *a*-C:H/Ag, and their biased counterparts. The samples are distinguished by their *in vacuo* XPS-revealed silver atomic concentrations. In comparison with *a*-C:H/Au (Section 3.2), a similar trend of decreasing total metallic content by employing substrate bias is observed, and will be discussed in detail in the presentation of PES data. Regarding surface morphology, one clearly notices that roughness of the grounded samples is increased here in comparison to fairly flat grounded samples of *a*-C:H/Au. On the other hand, similar "bump structure" on the surface of biased samples is observed. The quantitative data of the area roughness and maximum height detected are given

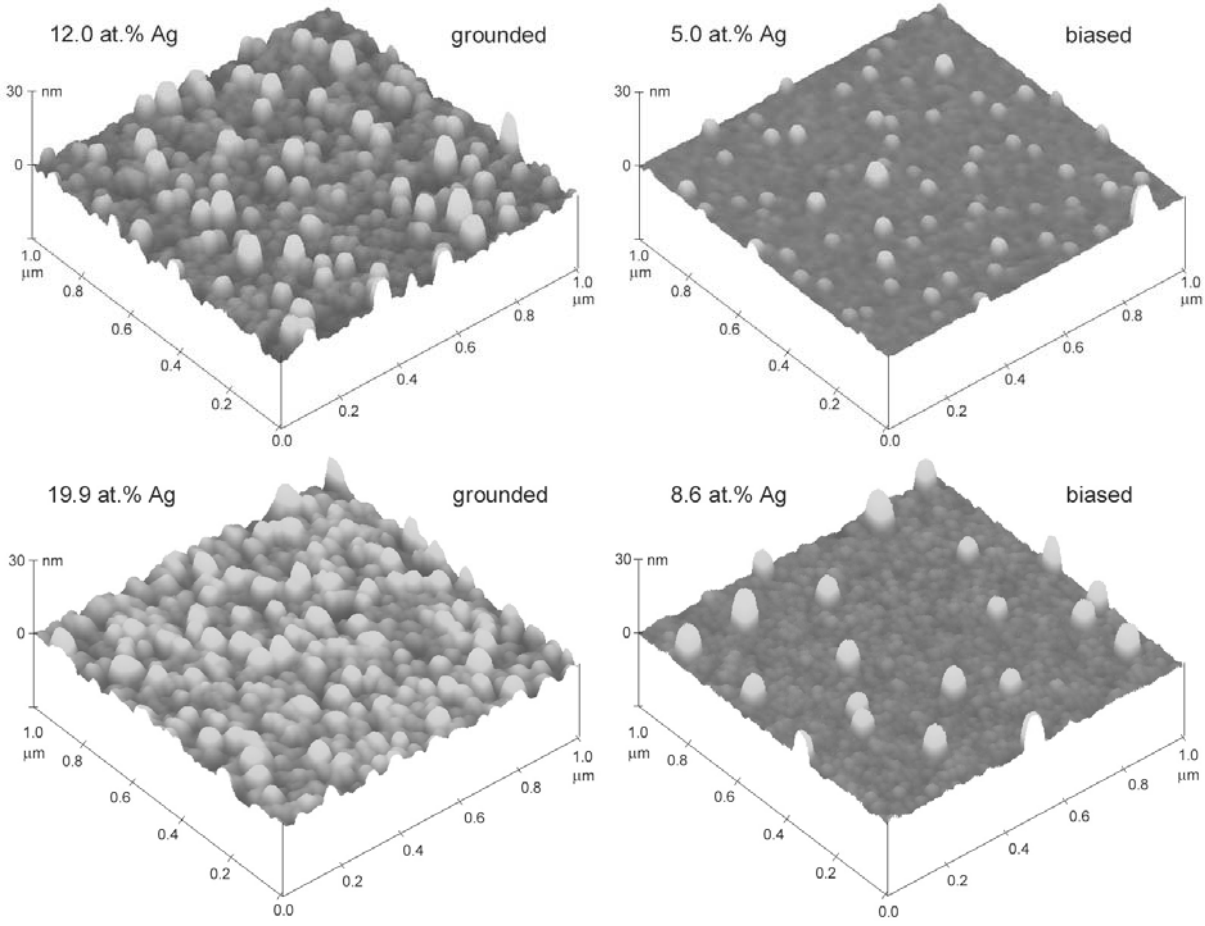

Fig. 3.4. AFM images of two grounded samples of *a*-C:H/Ag and their biased counterparts. Surface roughness of grounded samples is obviously higher in comparison with *a*-C:H/Au grounded sample. Similar bump structures on the surface of biased samples are observed.

for all four samples in Table 3.1, together with *a*-C:H/Cu data. It is interesting to compare roughness data for grounded samples of 12.0 at.% Ag (1.80 nm) and 19.9 at.% Ag (1.55 nm): in spite of higher metallic content, the latter sample appears smoother. If we recall now our discussion from Section 3.1 of He II UPS spectra of *a*-C:H/Ag, given in Fig. 3.2. (all samples in these series were grounded), this may be an additional argument to support the explanation of surface clusters coalescence into bigger agglomerates. Mutually merged, these islands decrease surface roughness. The biased samples expectedly show increase in roughness and maximum bump height with increasing Ag content, which might be an indication that applying surface bias voltage somehow inhibits silver atoms mobility and agglomeration.

The SEM micrographs of the same four samples are given in Fig. 3.5. The images are in reasonable agreement with AFM ones. Intercomparison of grounded samples reproduces the decreased roughness with increasing Ag content, encountered by AFM. Unfortunately, in their biased counterparts, the increased maximum height of the bumps with increasing Ag content is not obviously reproduced in SEM micrographs. Only the arrow-pointed features may be recognized as an isolated bump structures on the surface, while the bright spot in the image of 8.6 at.% biased sample seems to be an artifact.

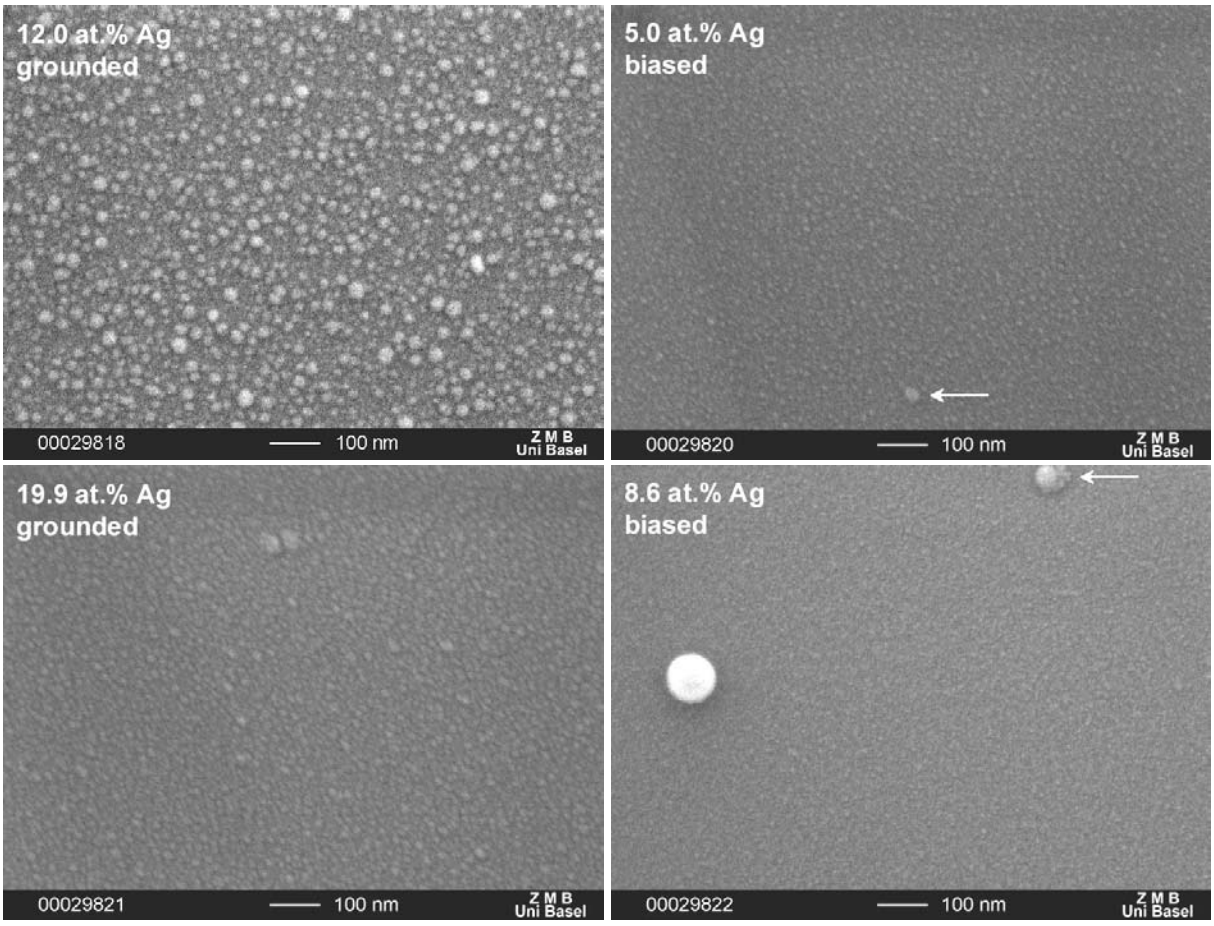

Fig. 3.5. SEM micrographs of *a*-C:H/Ag grounded samples and their biased counterparts, in agreement with AFM results. Arrows point the isolated bump structures at the surface of the biased samples. The bright spot in 8.6 at% sample is probably an artifact.

Figure 3.6 shows results of AFM direct imaging of *a*-C:H/Cu 8.6 at.% grounded sample and its 11.9 at.% Cu biased counterpart. Apart from the fact that, contrary to both *a*-C:H/Au and *a*-C:H/Ag, XPS yields in this case higher Cu content in the biased than in the grounded sample, one notices that general morphology trend is the same. Biasing the substrate results in isolated bump structures on the sample surface. Further increased roughness in the grounded case (2.16 nm, see data in Table 3.1) and somewhat conical shape of the surface structures is observed. Biased sample, in spite of higher metallic content than biased samples of *a*-C:H/Ag, seems to be flattened, with roughness of 0.44 nm. In this figure, we included two samples that are *not* counterparts, but have almost equal and also high metallic content from the point of view of this study. XPS on these samples was made *ex vacuo* and Cu concentrations of 27.1 at.% in the grounded and 26.5 at.% in the biased case are obtained. AFM measurements revealed increased roughness (see Table 3.1), but also the tendency of flattening in the biased sample, similar to the 8.6 at.% Cu grounded and 11.9 at.% biased counterparts.

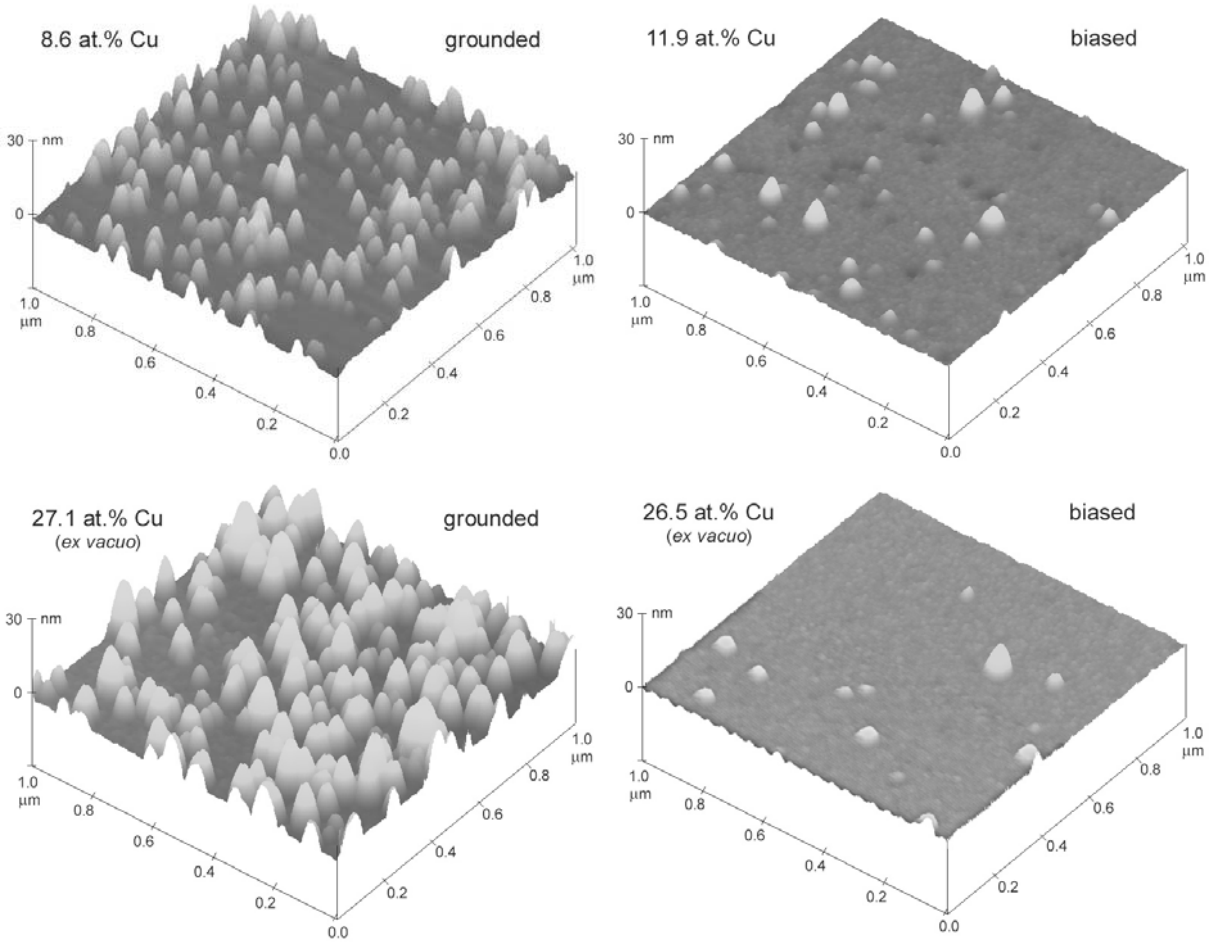

Fig. 3.6. AFM images of *a*-C:H/Cu samples. The two samples in the upper row are counterparts, the lower two are not. Their Cu content is similar and is measured by *ex vacuo* XPS. The apparent flattening of both biased samples and isolated bump structures are observed.

The SEM micrographs of the same four samples of *a*-C:H/Cu are given in Fig. 3.7, reasonably well reproducing the AFM data. The apparent flatness of the biased samples caused difficulties in measurement, and therefore in 26.5 at% Cu biased sample arrows point hardly visible isolated bump structures on the surface.

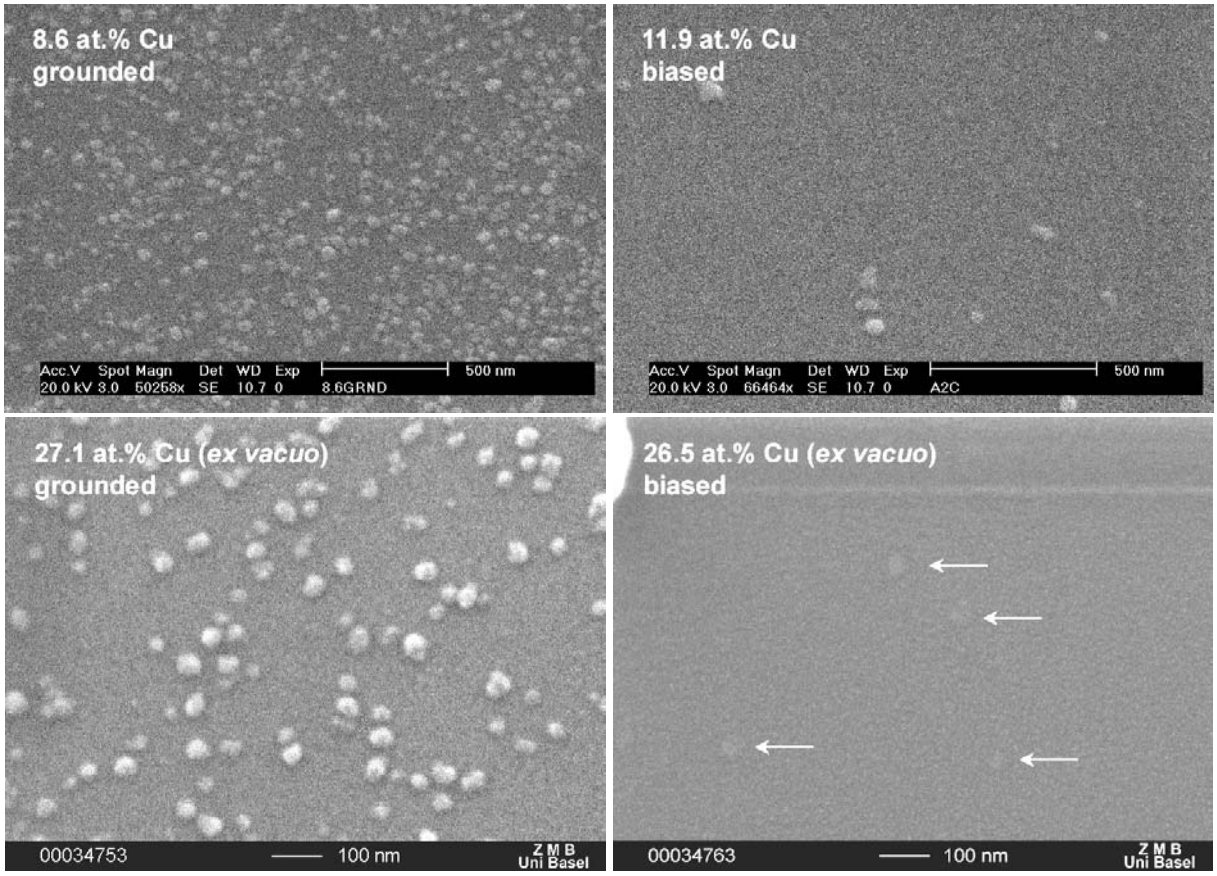

Fig. 3.7. The SEM images of *a*-C:H/Cu grounded and biased samples. A lower magnification for the 8.6 at.% grounded sample and its 11.9 at.% biased counterpart is used. In the last image arrows point hardly visible isolated bump structures at the surface.

Table 3.1. The data of surface area roughness and maximum height detected by AFM of *a*-C:H/Ag and *a*-C:H/Cu samples. Asterisks denote *ex vacuo* XPS-measured Cu content.

material	metal content (at.%)	substrate	roughness (nm)	max. height (nm)
a-C:H/Ag	12.0	grounded	1.80	19.1
	5.0	biased	0.53	14.6
	19.9	grounded	1.55	14.3
	8.6	biased	0.91	16.8
a-C:H/Cu	8.6	grounded	2.16	19.5
	11.9	biased	0.44	12.6
	*27.1	grounded	3.95	28.3
	*26.5	biased	0.37	12.4

Recapitulating the direct imaging results of all three nanocomposites studied, we may draw the common line as follows. Deposition on grounded substrates results in gradually increased roughness from *a*-C:H/Au to *a*-C:H/Cu. In *a*-C:H/Ag and *a*-C:H/Cu, this may be the result of surface agglomeration of clusters into bigger islands, in *a*-C:H/Cu showing a conical shape. For all three systems, biased samples show similar surface morphology: relatively flat base surface with isolated bumps with high aspect ratio. All these effects originate in inclusion of the metallic species into *a*-C:H matrix. This conclusion is supported by direct imaging of pure *a*-C:H, deposited on grounded and biased substrate, and shown in Fig. 3.8. AFM images

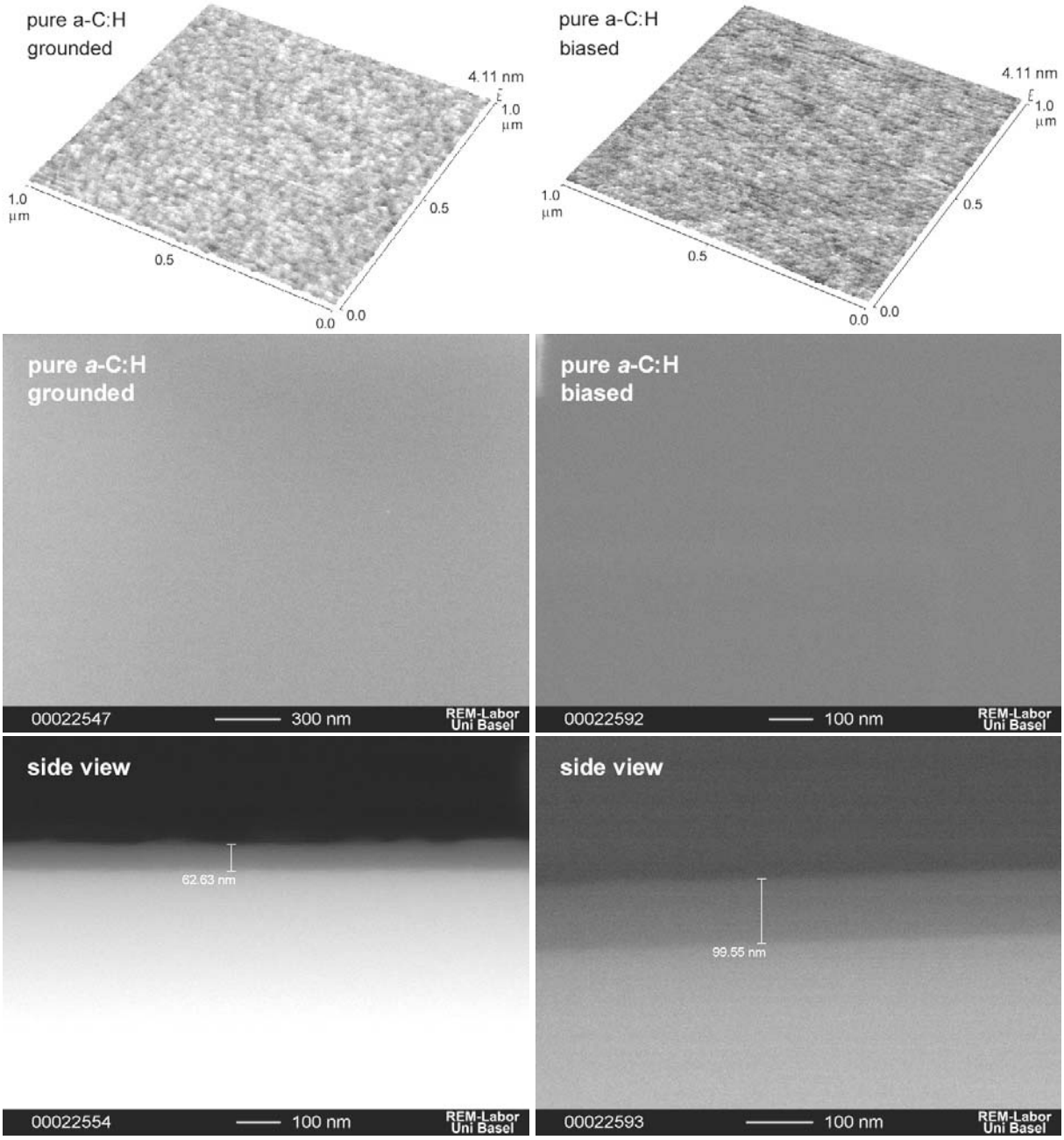

Fig. 3.8. Direct imaging of pure *a*-C:H, deposited on grounded and biased substrate. AFM (upper) reveals roughness of 0.18 nm and 0.15 nm, respectively. The from the SEM images is obvious (middle). The lower images show side view of *a*-C:H films in backscattering mode.

reveal extremely low roughness of 0.18 nm and 0.15 nm in grounded and biased case, respectively. From the top SEM views the flatness of the samples is obvious. The side view in backscattering mode shows the substrate and the *a*-C:H film on it. It should be noted that films of that large thickness are not deposited in nanocomposite materials. In pure *a*-C:H deposition one does not tremble from target poisoning.

3.4. GISAXS results

The GISAXS patterns of our grounded *a*-C:H/Au samples are analyzed in detail by Babonneau *et al.* [35]. Here we shall give the GISAXS patterns of 8.2 at.% sample and its biased counterpart, followed by the samples of other two nanocomposite systems. At the end of this section, all quantitative data on cluster dimensions and intercluster distance will be comprised in Table 3.2.

Figure 3.9 shows GISAXS patterns of *a*-C:H/Au 8.2 at.% grounded sample and its biased counterpart. An isotropic half-ring in the grounded sample pattern evidences on the spatial correlation between nearly spherical isolated gold clusters embedded in the *a*-C:H matrix. In the biased sample pattern, the high intensity near the beam-stop (physical barrier to cut the primary beam) is an indication of either very large clusters, or high roughness of the surface. Quantitative analysis to obtain information of cluster dimensions and intercluster distance fails in the cases like the latter one, and therefore GISAXS technique immanently requires smooth surfaces. Hence, this kind of pattern is in agreement with high aspect ratio bumps in the biased sample observed by direct imaging techniques, see Section 3.2, Fig. 1.

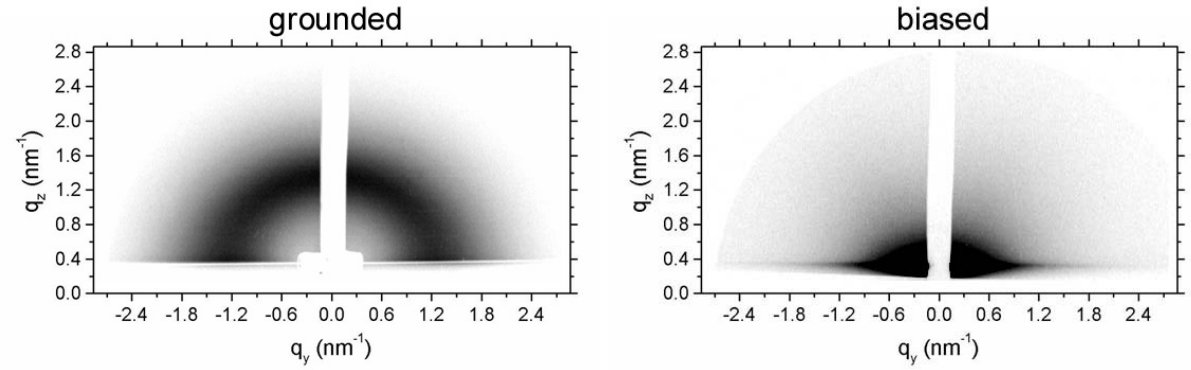

Fig. 3.9. GISAXS patterns of *a*-C:H/Au grounded sample and its biased counterpart. The isotropic ring in the grounded pattern indicates spatial correlation of gold clusters. In the biased sample, the intensity maximum near the beam-stop reveals high surface roughness.

The GISAXS patterns of *a*-C:H/Ag grounded samples of 12.0 at.% and 19.9 at.% and their biased counterparts of 5.0 at.% and 8.6 at.%, respectively, are given in Fig. 3.10. No isotropic ring, like the one in the case of grounded *a*-C:H/Au sample is observed in *a*-C:H/Ag. Some spatial correlation can be deduced in samples with higher Ag content, but only in the lateral direction. Absence of isotropic ring in the

grounded samples may be another evidence on cluster agglomeration at the sample surface. However, the fact itself that an usable scattering signal, which can be analyzed, is obtained from biased *a*-C:H/Ag samples reveals that surface roughness is decreased in comparison with *a*-C:H/Au biased sample.

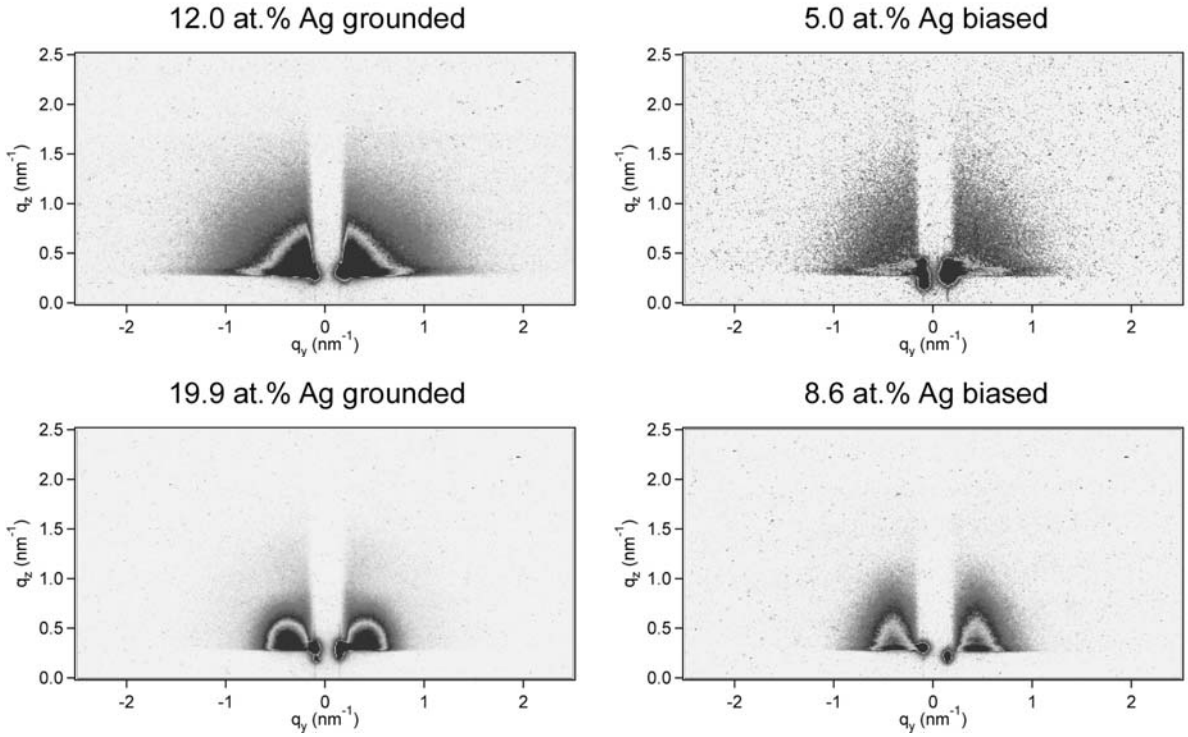

Fig. 3.10. GISAXS patterns of two *a*-C:H/Ag grounded and biased samples. In-plane correlation in the 19.9 at.% grounded and 8.6 at.% biased sample is observed.

Figure 3.11 shows GISAXS patterns of grounded and biased *a*-C:H/Cu samples. Similarly to *a*-C:H/Au, in the 8.6 at.% Cu grounded case a half-ring is observed, evidencing on isotropic distribution of nearly spherical Cu clusters. In the biased 11.9 at.% Cu sample, a pattern that reveals in-plane correlation is observed. The two lower images show GISAXS patterns of samples with *ex vacuo* measured Cu content of 27.1 at.% and 26.5 at.% in grounded and biased case, respectively. The GISAXS patterns show that an isolated cluster structure exists in these samples, in principle similar to the cluster structure of low copper-content samples. Once again should be noted that biased samples yield usable GISAXS patterns that enable quantitative analysis.

All quantitative data obtained by Guinier plot analysis of the images in Figs. 3.9 – 3.11 are comprised in Table 3.2. The missing data in the table are in those cases where no correlation was encountered. It is interesting to compare data in Table 3.2 with estimation of the cluster size from shift in binding energies of the metallic core levels, see Section 3.1. Observing first sample in each group in Table 3.2, it turns out that rough approximation of spherical capacitor and one-electron charging from Section 3.1 yields correct order of magnitude for the cluster diameter. Moreover,

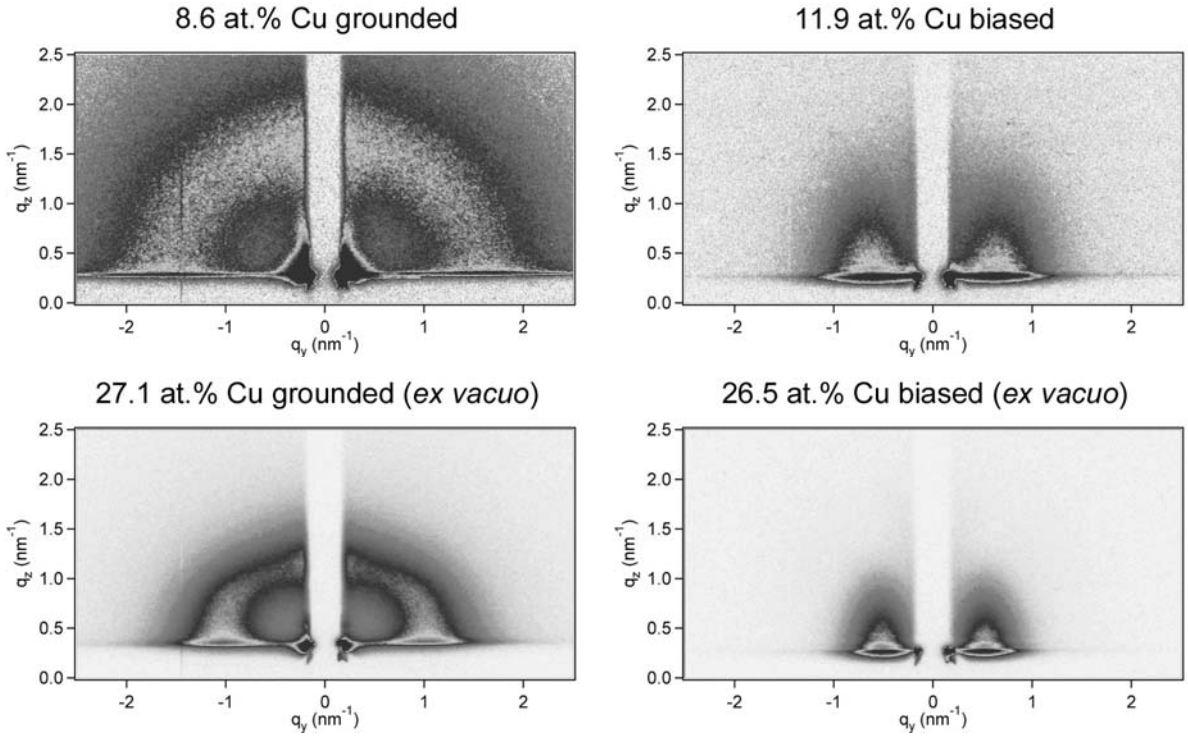

Fig. 3.11. GISAXS patterns of *a*-C:H/Cu grounded sample and its biased counterpart (upper). An isotropic cluster arrangement in the grounded, and lateral correlation in the biased case are envisaged. Two higher-Cu content samples (lower images), with *ex vacuo*-determined Cu concentration reveal similar cluster structure as low-Cu content ones.

the deviations do not exceed factor of 2. The trend of decreasing cluster size from *a*-C:H/Au to *a*-C:H/Cu is also reproduced. The Ag clusters only do not fit into this trend. Apart from the fact that GISAXS analyzed *a*-C:H/Ag 12.0 at.% sample contains more metal than the sample characterized by XPS in Section 3.1 (9.8 at.% Ag), we believe that the reason for this deviation lies in cluster post-deposition agglomeration. GISAXS measurements are made *ex vacuo*, and later will be shown that exposure of an *a*-C:H/Ag sample to the atmospheric oxygen induces structural changes, with agglomeration of silver clusters being the most pronounced one.

Table 3.2. Nanocluster dimensions obtained by Guinier plot-analysis of GISAXS patterns. Values are missing where no spatial cluster correlation exist. The copper content denoted by asterisks is measured by *ex vacuo* XPS.

material	metal conc. (at.%)	substrate	in-plane cluster dimensions		growth direction dimensions	
			diameter (nm)	distance (nm)	height (nm)	distance (nm)
a-C:H/Au	8.2	grounded	2.7	4.5	3.3	4.7
a-C:H/Ag	12.0	grounded	3.8	/	spherical	/
	5.0	biased	3.9	/	bit flattened	/
	19.9	grounded	6.5	14.2	5.7	/
	8.6	biased	8.8	15.6	8.4	/
a-C:H/Cu	8.6	grounded	1.8	4.0	spherical	isotropic
	11.9	biased	4.3	10.3	3.5	/
	*27.1	grounded	4.1	5.8	spherical	isotropic
	*26.5	biased	6.5	12.2	5.3	/

3.5. Photoelectron spectroscopy results

3.5.1. As-deposited sample surfaces

We start the review of a series of photoelectron spectroscopy measurements aimed to reveal the surface structure and nanocluster arrangement in low-metallic content *a*-C:H/Au, *a*-C:H/Ag, and *a*-C:H/Cu with the classical *in vacuo* PES measurement of as-deposited surfaces of grounded and biased samples.

Figure 3.12. shows Au $4f_{7/2}$, Ag $3d_{5/2}$, Cu $2p_{3/2}$, and corresponding C 1*s* core-level spectra of as-deposited low metallic content nanocomposites on grounded substrates and their biased counterparts. For this purpose *a*-C:H/Au 5.7 at.%, *a*-C:H/Ag 12.0 at.%, and *a*-C:H/Cu 8.6 at.% and their biased counterparts of 2.9 at.% Au, 5.0 at.% Ag, and 11.9 at.% Cu are deposited. With the exception of *a*-C:H/Au samples, the other two pairs are also studied by *ex vacuo* techniques – direct imaging and GISAXS, and these results are already presented and discussed.

Metal core levels of all grounded samples at these concentrations show shifts towards higher binding energies with respect to the bulk metal references. This effect we already related to the isolated cluster structure of metallic inclusions (see Section 3.1). The first effect of biasing the substrate that one notices by PES is the decrease of the metal amount in the coating, which we quantitatively specified above (also given in Fig. 3.12). This is a systematic consequence in all *a*-C:H/Au and *a*-C:H/Ag samples that we examined. The decrease of the total metal amount in comparison to the grounded counterparts is about 50%. The *a*-C:H/Cu nanocomposite turned out to be an exception from this rule, with higher metallic content in biased than in the grounded case.

Further, the metal core levels of the biased *a*-C:H/Au and *a*-C:H/Ag samples are shifted to even higher binding energies than in the grounded cases. Again, the only exception was *a*-C:H/Cu, which in both grounded and biased cases showed same BE shift of 0.53 eV. In the *a*-C:H/Au sample the difference between biased and grounded shifts is 0.09 eV, and in *a*-C:H/Ag as much as 0.20 eV. As already discussed in Section 3.1, this may be a result of either smaller or only partially embedded clusters at the surface. The assumption of smaller clusters in the biased than in the grounded samples would be hardly supported by direct imaging and especially GISAXS results (Sections 3.3 and 3.4)[*]. AFM and SEM clearly showed isolated bump structures in the biased cases. At the first glance one may guess that these structures are metallic clusters themselves, but their dimensions of about 30 nm in diameter (see Fig. 1 in Section 3.2 and Figs. 3.5 and 3.6) are far above those that may cause the BE shifts which we measured. It is more likely that these bumps are some modification of the *a*-C:H, induced by the presence of metallic clusters.

[*] The comparison of the *in vacuo* and *ex vacuo* results should be made carefully, due to possible air-induced cluster coalescence (see Paragraph 3.5.4).

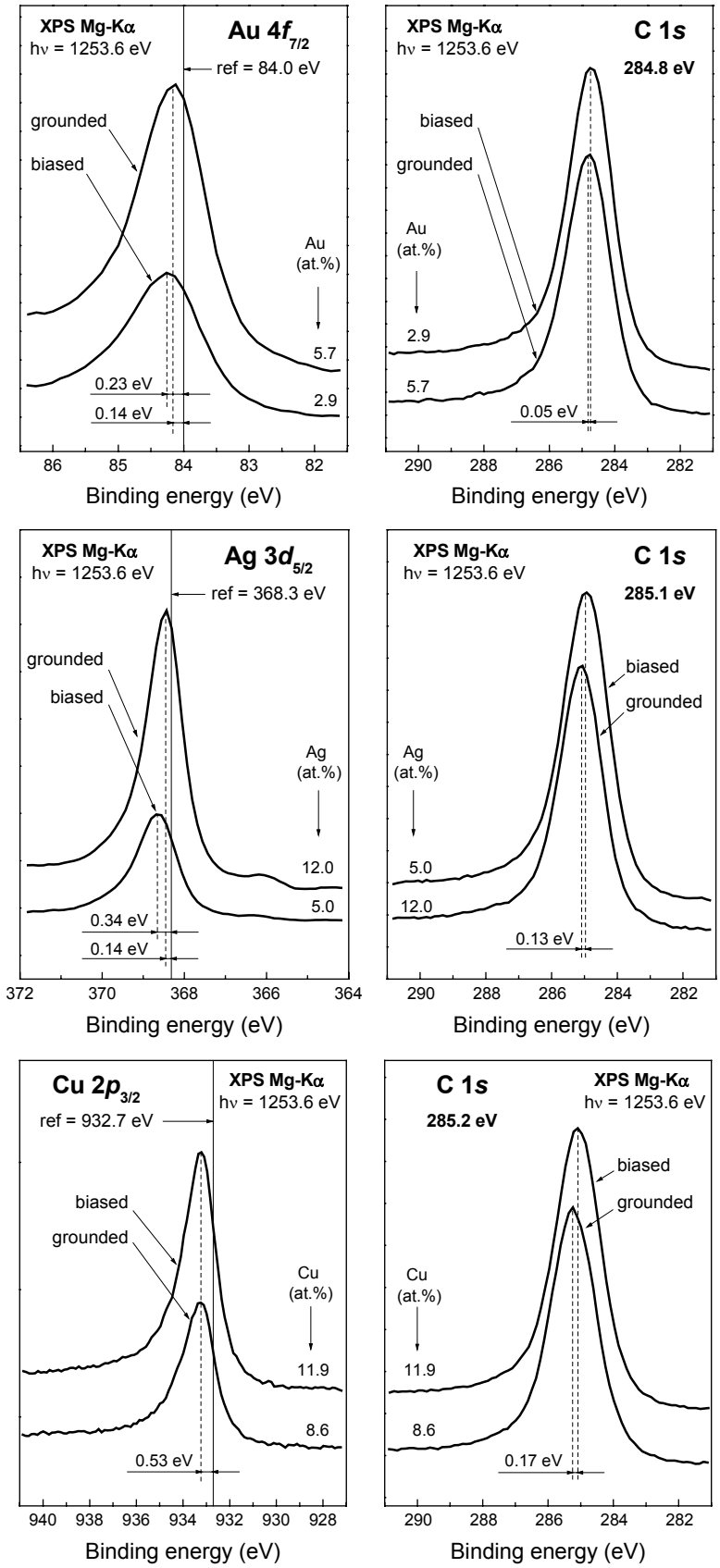

Fig. 3.12. Core-level spectra of Au $4f_{7/2}$, Ag $3d_{5/2}$, Cu $2p_{3/2}$, and corresponding C 1*s* in low-metallic content grounded and biased samples. Vertical solid lines mark the bulk metal reference BE. Bolded BE values in C 1*s* spectra are absolute BEs in grounded cases.

The GISAXS results clarify to some extent this puzzle. Analysis of biased *a*-C:H/Ag and *a*-C:H/Cu samples revealed not only the bigger size clusters in the biased than in the grounded case, but also significantly increased intercluster distance (see Table 3.2). Again, the obtained cluster size, although increased than in the grounded cases, is much smaller than the structures seen in the AFM and SEM images, and confirms that those are not metal clusters themselves. On the other hand, increased intercluster distance provides an explanation on decreased total metal content in the biased case.

Putting all these arguments together, it is reasonable to look for the reason of the increased metal BE shift in *biased samples* in partial embedment, i.e. *baldness* of the surface clusters. Being slightly bigger than in the grounded cases (see Table 3.2), they are most probably concentrated at the large bump structures of about 30 nm in size, observed by direct imaging techniques (see Fig. 1 in Section 3.2 and Figs. 3.5 and 3.6). This explanation of the situation upon applying substrate bias voltage, implicitly embraces the picture of topmost metallic clusters in *ground cases* that are not partially embedded, i.e. which *are covered with a tiny layer of a-C:H*. The thickness of this layer has to be below escape depth of x-ray excited metal-originated electrons. That is, according to Fig. 2.7 and related explanations, below 2 nm. If proved by another test experiments, this model can explain earlier problem [31] of systematically higher metallic content in the bulk obtained by RBS, than on the surface, measured by XPS.

In analysis of behavior of the C 1*s* core level in all three systems, we shall also begin with grounded samples. The absolute BEs of the C 1*s* peak are given in Fig. 3.12. It is interesting to notice that C 1*s* core level in *a*-C:H/Au, which has the lowest metallic content of 5.7 at.%, appears at the lowest BE of 284.8 eV. In *a*-C:H/Ag and *a*-C:H/Cu, the C 1*s* position of 285.1 eV and 285.2 eV are measured, respectively. In the light of our discussion of the C 1*s* core level in Section 3.1, this result should indicate highest sp^2-coordinated carbon content in *a*-C:H/Au in comparison with other two systems. This may be a result of either largest clusters (even in that low-metallic content), or, which is more likely, the highest compressive stress of *a*-C:H due to the poor mobility of Au atoms within the matrix. The other two metals are characterized with higher mobility that reduces the potential energy of compressive stress.

Applying substrate bias voltage in all samples results in C 1*s* core level shift to the lower binding energies, revealing increased ratio of sp^2/sp^3 coordinated carbon. The values of these shifts are given in Fig. 3.12. The smallest negative BE shift of 0.05 eV is encountered in *a*-C:H/Au. Although GISAXS results on *a*-C:H/Ag and *a*-C:H/Cu revealed increased cluster size upon biasing the substrate, it also yielded increased intercluster distance and therefore, we would not attribute this gain in sp^2-coordinated carbon to the compressive stress. It is more likely that the additional "graphitization" is due to the sample bombardment by Ar^+ ions during the deposition process. If we recall the potential distribution in the magnetron plasma given in Fig. 2.2, applying negative substrate bias results in accelerating Ar^+ ions not only to the target, but also to the substrate. Bombarding the substrate, Ar^+ ions break the iso-

tropic sp^3 bonds in the carbon matrix and hence pronounce sp^2-coordinated carbon [105]. This additional increase is the least reflected in *a*-C:H/Au, due to its highest ground content of in sp^2-coordinated carbon (C 1*s* at lowest BE of 284.8 eV, see Fig. 3.12). The Ar^+ ion bombardment of the sample during the deposition is, we believe, also responsible for baldness of the topmost surface clusters on the biased samples.

This is a point where we should draw some attention to the accuracy of our measurements. One notices that we have given the absolute binding energy values with usual uncertainty order of 0.1 eV, while the shifts are given with one order of magnitude higher accuracy. The question that might be risen here is – how approved is to report values with uncertainty less than 0.1 eV, with the instrument resolution of 0.93 eV (see Paragraph 2.2.1)? Our opinion is that this remark is reasonable and we adopted it in absolute BE measurements. However, reducing the accuracy in direct comparison measurements and rounding the obtained BE values would hide the fine effects and tiny BE shifts. In using a higher accuracy, we rely on the fact that observed shifts are not random errors, but *systematical trends* in our measurements. Therefore, we generally adopted the uncertainty of absolute measurements of 0.1 eV, and estimated error bar of relative BE measurements of 0.02 eV.

The normalized valence band spectra of the samples whose core level spectroscopy discussion we just completed, are given in Fig. 3.13. With increased surface sensitivity, He I and particularly He II spectra reveal new information on the phenomenon that occurs when two samples are deposited under the same conditions, just one grounded and the other with –150 V applied to the substrate. One notices first that all three grounded samples He I spectra are quite alike, very much reproducing the shape of the pure *a*-C:H spectrum, with dominant broad maximum of carbon σ-states at 7.5 eV, and a shoulder at about 3.5 eV attributed to the π-states of carbon (see Fig. 3.2). That evidences on the similar, in majority *a*-C:H content of the surface region of all grounded samples. With higher photoemission cross-section of incident photons [117] and hence increased sensitivity, He II spectra provide stronger evidence on the presence of metallic inclusions in all three grounded samples. One notices evidences of characteristic metal valence band features: in *a*-C:H/Au – an increased shoulder at about 3 – 4 eV, and a development of a narrow peak at about 6 eV typical for the Au 5*d* band; in *a*-C:H/Ag – a clear evidence of Ag 4*d* band between 4 eV and 7 eV; in *a*-C:H/Cu – a development of a shoulder at 3 – 4 eV related to the Cu 3*d* band. The He II spectrum of *a*-C:H/Ag shows more pronounced metallic features than the He II spectra of the other two materials, which also supports the possible Ag cluster coalescence at the surface.

Biasing the substrate during deposition results in altered valence band spectra (Fig. 3.13). In the He I spectrum of *a*-C:H/Au 2.9 at.% biased sample, in comparison to the 5.7 at.% grounded one, these alterations are: increased shoulder at 3.5 eV (a) and appearance of a kink at 6 eV (b). Both features are related to the rise of Au 5*d* band, evidencing on higher exposure of gold at the surface. Feature (a) can be also recognized as increased π-states of carbon, but it overlaps with broad Au 5*d* band and these contributions cannot be distinguished. The alterations in all three features

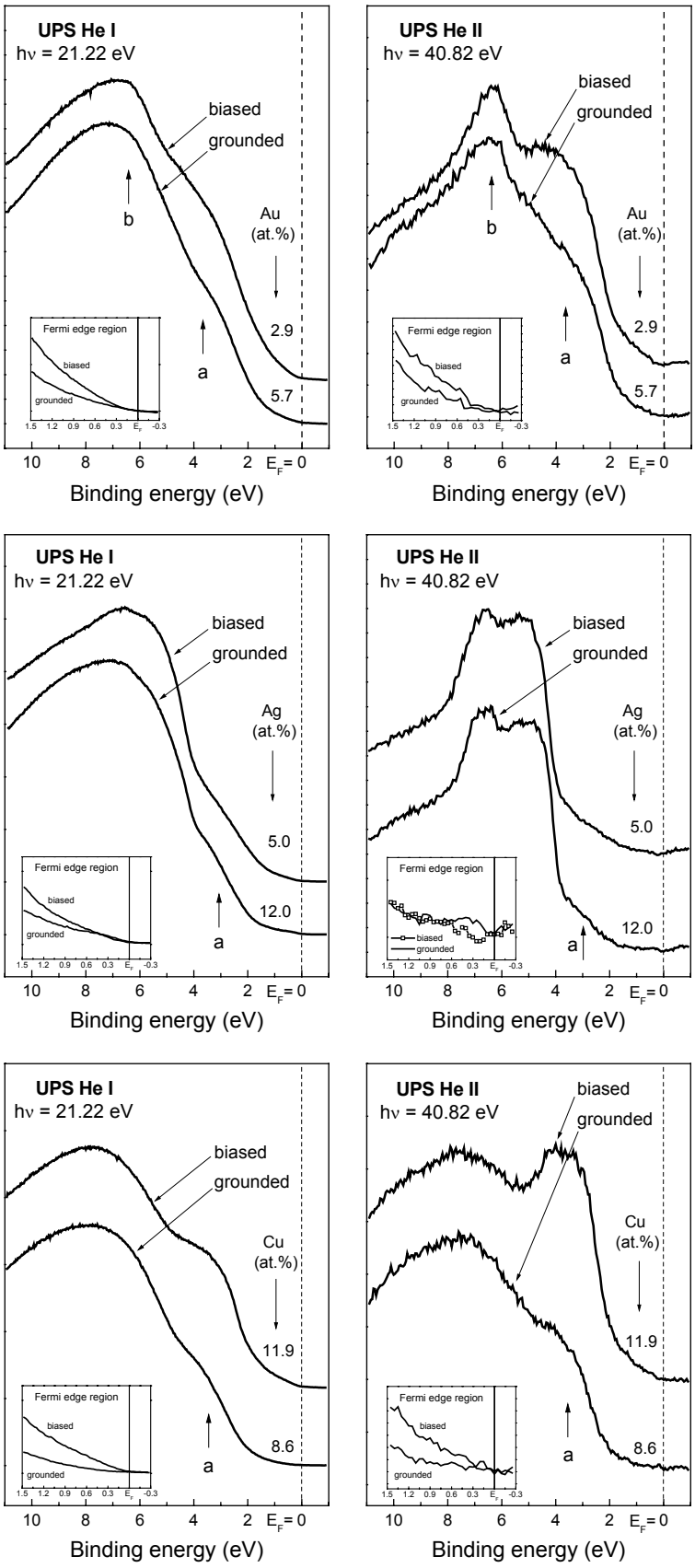

Fig. 3.13. Normalized He I and He II valence band spectra of low-metallic content grounded and biased samples. The features that are altered upon biasing are denoted by letters and pointed by arrows. The insets show enlarged Fermi edge regions.

are much more reflected in the He II spectrum of biased *a*-C:H/Au sample. A clear increase of a narrow peak (b) in Au 5*d* band, strong development of both low-BE part of Au 5*d* band (a, overlapping with π-states of carbon) evidence on higher exposure of gold at the surface. The insets in He I and He II spectra show enlarged Fermi edge region. We cannot speak about the development of a Fermi edge in any of the samples we examined here, because all of them are doped with low metal amount and, as a whole, are insulating. However, there is a clear rise of the DOS in biased samples close to the Fermi edge, which may originate from development of the Au 5*d* band or/and higher content of sp^2-hybridized carbon bonds [107,108].

Similarly to the *a*-C:H/Au biased sample, the He I spectrum of *a*-C:H/Ag 5.0 at.% biased sample shows alterations related to the increased silver at the surface. Two kinks at about 5.8 eV and 6.6 eV (Fig. 3.13) evidence on the increase of the characteristic Ag 4*d* band features. The more sensitive He II valence band spectroscopy does not show significant alterations from already very Ag features-rich grounded sample spectrum. The increase of the carbon π-states (a) is not unambiguously observed. The enlarged Fermi edge in the inset of He I spectra show rise of the DOS near the Fermi edge, which is not, however, clearly supported with the same enlargement inset in the He II spectra.

The biased sample of *a*-C:H/Cu is the only one which showed higher total metal content than its grounded counterpart. That fact is also reflected in the valence band spectra (Fig. 3.13). The He I spectrum of *a*-C:H/Cu 11.9 at.% biased sample shows the most prominent alterations in comparison to the grounded counterpart. The increase of intensity at about 3 eV (a) where the Cu 3*d* band is located is not only due to the higher Cu content, but also due to the increased exposure of Cu clusters at the surface. The development of the Cu 3*d* band masks the change in carbon π-states that are located at same binding energies. The insets in both graphs show increased intensity in states near the Fermi edge in biased *a*-C:H/Cu sample.

The biased samples valence band spectra are, therefore, more or less altered, but all in the same direction, towards increase of the metallic features at the surface.

3.5.2. Off-normal take-off angle XPS

Looking for further evidences of the apparent topmost metallic clusters coverage with a layer of *a*-C:H on grounded substrates, and their baldness with the substrates kept on negative bias voltage, we performed XPS experiments changing the take-off angle of electrons by tilting the sample. The idea and the principle of this experiment are given in Paragraph 2.2.2 and in Fig. 2.9: with increasing off-normal take-off angle, the coverage and the baldness of the surface clusters should give different response in the intensity ratio of the metal core levels to the C 1*s* core level.

Figure 3.14 comprises typical results of this experiment in all three nanocomposite systems we examined, for grounded samples and their biased counterparts with different metallic contents. In the figure, the intensity ratios of Au $4f_{7/2}$ and C 1*s*, Ag $3d_{5/2}$ and C 1*s*, and Cu $2p_{3/2}$ and C 1*s* are given for grounded and biased samples, as a function of angle of tilting the sample (take-off angle). The intensity is measured as an integral area below the core level peak, after subtracting Shirley background. Being closely related to the core level intensity, the apparent atomic "content" is given on the right-hand side axis, and represented by hollow symbols.

The results shown in Fig. 3.14 encourage our interpretation of the results obtained by PES of as-deposited samples. By tilting the low metal-content grounded sample, the monotonous decrease of metal to carbon core levels intensity ratio reveals that fewer metal-originated electrons arrive to the spectrometer. At the same time, the number of electrons escaped from carbon atoms increases. These results support the previously offered explanation of surface clusters that are covered with a tiny layer of *a*-C:H. In the biased samples, the increase of the metal to carbon core level intensity ratio reveals bald metallic clusters on the surface.

In the grounded samples in Fig. 3.14 one observes that samples with higher content of Au and Ag do not follow the tendency of monotonous decrease that is encountered with all low-metallic content samples. This is a good point to place for the first time our assumption of the origin of clusters coverage on the surface of grounded samples. We believe that this effect is caused by the phenomenon known in plasma physics as *afterglow*. Namely, after switching off the plasma power supply, the different species in the ionized gas are de-excited, neutralized and thermalized neither instantaneously, nor simultaneously. Some species "live" longer in the so-called afterglow than the others. We believe that in this case, carbon and hydrocarbon species persist longer in the afterglow than metallic ones, still having sufficient kinetic energy to arrive to the substrate. Arriving latest, they form that thin layer which covers topmost metallic clusters. The concentration of carbon and carbohydrates in the plasma is determined by the gas pressure, which was kept constant in all our experiments. Therefore, smaller surface clusters may be fully covered by an *a*-C:H layer, while bigger ones, in samples with higher metallic content, most probably contain only some scattered *a*-C:H on the surface. To our belief, this is the reason why bigger metallic clusters in the grounded samples show behavior of bald surface clusters. They are actually bald, like the smaller ones in the biased samples.

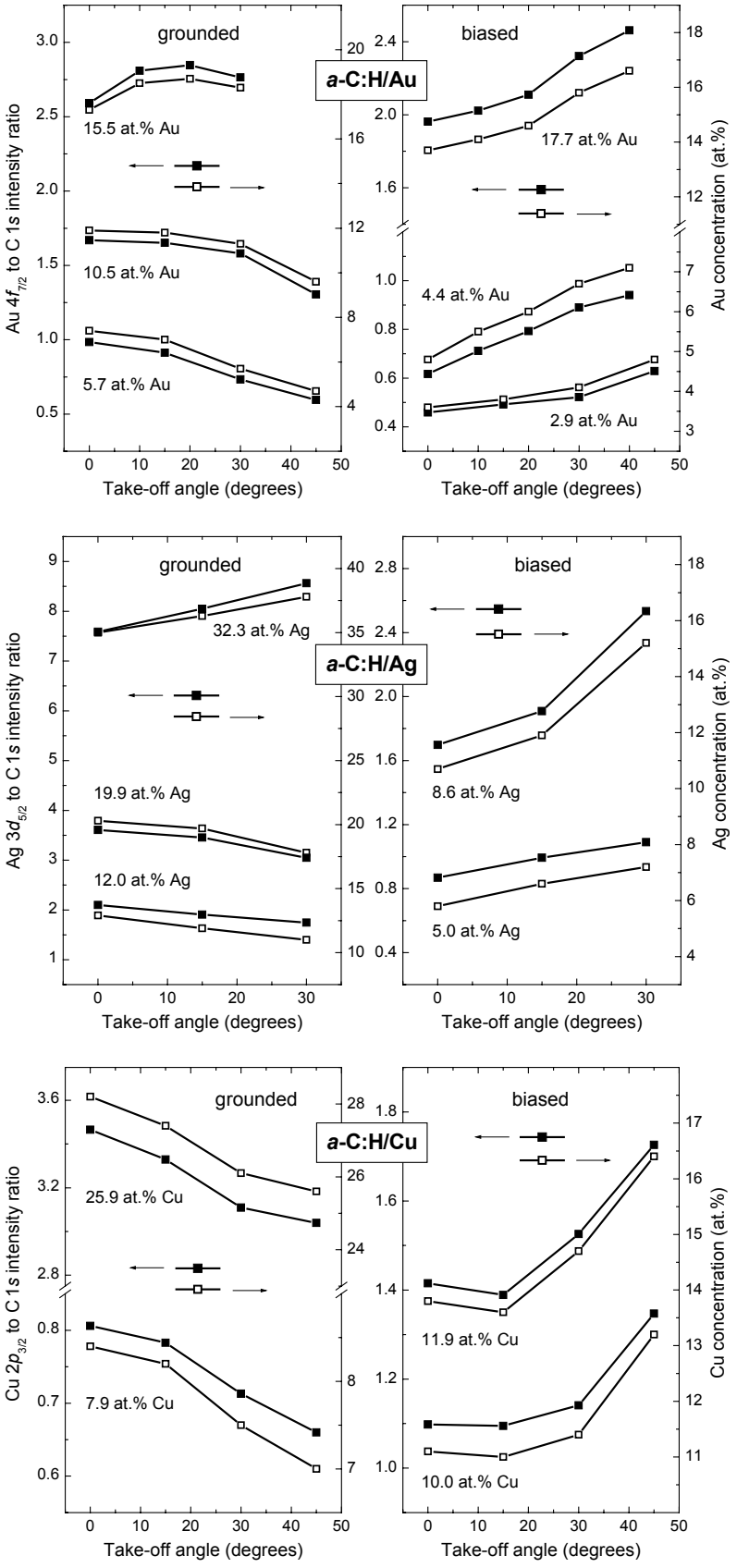

Fig. 3.14. Intensity ratio of metal to carbon core levels (solid symbols, left axis) and apparent metal “content” (hollow symbols, right axis) vs. electron take-off angle (zero refers to the usual electron take-off, perpendicular to the sample surface).

3.5.3. *In situ* in-depth PES analysis

A further challenge that arises from so far presented results and arguments related to the coverage of the topmost metallic clusters in nanocomposites with *a*-C:H is as follows: if topmost clusters in the grounded samples are really covered with a layer of *a*-C:H – it should be possible to remove that layer. The idea of the *in situ* etching the sample surface is already explained in Paragraph 2.2.2 and schematically depicted in Fig. 2.10. We subjected our samples to the Ar^+ ion bombardment in the PES measurement chamber, and to the XPS and UPS analysis after subsequent sputtering sessions.

Figure 3.15 shows the results of the measured intensity ratio of metal (Au $4f_{7/2}$, Ag $3d_{5/2}$, and Cu $2p_{3/2}$) to appropriate carbon C 1*s* core levels, i.e. related metal content (C content complements to 100 at.%), for several samples of each nanocomposite system. Some samples are treated *in vacuo*, immediately after deposition, and some after being exposed to the air – *ex vacuo*, and this information is provided accordingly. E.g. all *a*-C:H/Au samples are treated *ex vacuo*, and all *a*-C:H/Ag *in vacuo*, while with *a*-C:H/Cu samples both methods are applied. The influence of the sample exposure to the air is obvious in the ex vacuo measurements: after first, very short steps of 5 s of sputtering the sample, a steep increase of metal to carbon core level intensity ratio is observed. This rise we attributed to the removal of the atmospheric contamination from the sample surface. After that point, both *ex* and *in vacuo* treated samples show similar behavior. The values of the metallic content given in the graphs in at.% are those measured before beginning of the sputtering process.

The results in Fig. 3.15 provide couple of important supporting conclusions to our study, especially to the origin of coverage of topmost metallic clusters in the grounded samples. In all grounded samples, at the beginning of the sputtering process, a rise of metal to carbon core level intensity is observed. This rise is related to the removal of the *a*-C:H layer from the surface clusters. Existence of the maximum at these curves is attributed to the point when topmost clusters are completely uncoated. Further Ar^+ ion bombardment reduces the metallic content as well. By comparing time scales in the graphs one concludes that samples with low metallic content take longer time to remove the covering layer than high-metallic content ones, which reach the maximum in the intensity ratio curve after relatively shorter sputtering time. This result supports our proposal for explanation of the origin of the grounded samples surface clusters coverage. Namely, if our assumption from previous section is right, the covering *a*-C:H “material” that is at the disposal to the surface clusters, depends on the gas pressure in plasma only, i.e. is constant to all samples deposited in this study. The smaller clusters, in lower metallic-content samples, are therefore covered with thicker layer than the larger ones in higher metallic-content samples, and need longer sputtering time to get fully uncoated. The higher metallic-content samples not only reach maximum after shorter time, but in some cases show no detectable coverage, i.e. monotonous decrease of the intensity ratio curve, e.g. *a*-C:H/Ag 32.3 at.% sample, see Fig. 3.15. An interesting question arises here: what

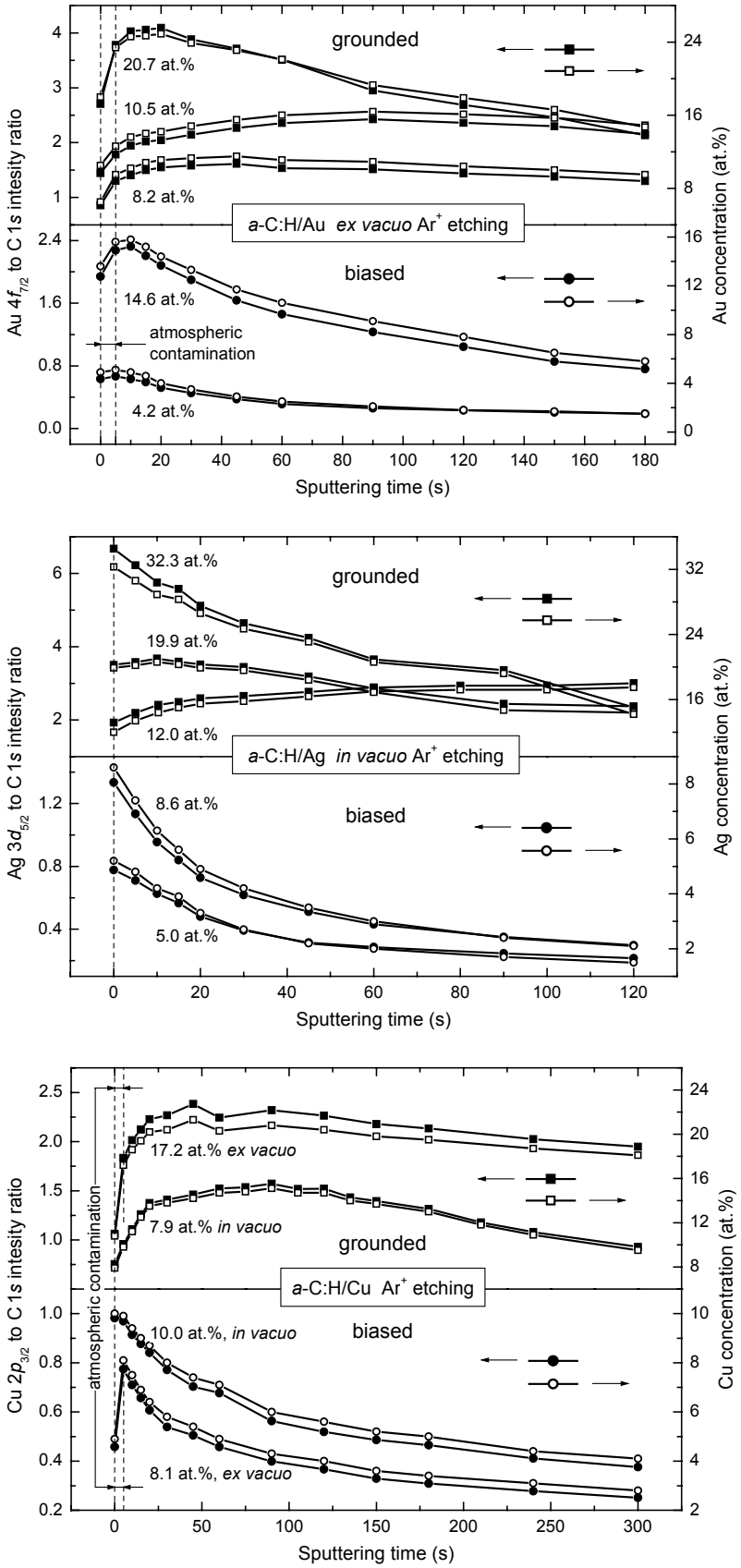

Fig. 3.15. *In situ* Ar^+ ion etching of the samples: sputtering time evolution of the intensity ratio of metal to carbon core levels (solid symbols, left axis) and metal concentration (hollow symbols, right axis). The nominal metal contents are measured before sputtering beginning.

we should take as a real metallic content in a nanocluster-containing *a*-C:H sample deposited on a grounded substrate? Is it the one that we measure by *in vacuo* XPS, or is it the one that we encounter as a maximum of the intensity ratio (i.e. metallic content) vs. sputtering time curve? In some cases these values can differ significantly. E.g. for *a*-C:H/Cu 7.9 at.%, measured *in vacuo* as-deposited, the maximum content of 15.1 at.% Cu is reached after 90 s of sputtering, see Fig. 3.15. Of course, one should bear in mind that Ar^+ ion etching is an intrusive technique that affects the sample. Nevertheless, we believe that this is the problem that Schüler *et al.* faced in the XPS and RBS comparison of the titanium content in *a*-C:H/Ti [31].

Biased samples, as we expected in this experiment, show monotonous decrease of the metal to carbon core level intensity ratio throughout the measurement (Fig. 3.15). The only exceptions are *ex vacuo* measured samples in the first short sputtering time interval, when air contamination removal took place. This behavior of biased samples is another argument for their baldness on the sample surface in all examined nanocomposite systems.

Apart from the core level intensity ratio, i.e. metal content measurements, subsequent Ar^+ ion etching and PES measurements provided a series of spectra that describe the time evolution of the treated sample. In the following figures, we shall present XPS and UPS spectra at several selected points on the sputtering time scale. Only *in vacuo* samples are given in these figures. The starting sample state i.e. zero sputtering time and the ending point will be included in all graphs.

As usual, we start with *a*-C:H/Au. Figure 3.16 shows Au $4f_{7/2}$ and C 1*s* core levels of grounded sample with 5.7 at.% Au and its biased counterpart with 2.9 at.% Au during the sputtering process. Unlike other *a*-C:H/Au samples that we showed in Fig. 3.15, this sample is treated by Ar^+ ion bombardment *in vacuo*. The Au $4f_{7/2}$ to C 1*s* intensity ratio curve for this sample is shown in Section 3.2, Fig. 4. In grounded samples, with Ar^+ ion sputtering, the binding energy of Au $4f_{7/2}$ core level is slightly shifted from the starting 0.14 eV (5.7 at.% Au) to 0.18 eV (6.8 at.% Au) above the reference position, after 90 s of bombardment. This increase may be attributed to the thinning of the *a*-C:H layer that covers topmost clusters. It should be noted here that in this sample total removal of the cover layer is not achieved – the point of maximum in Au $4f_{7/2}$ to C 1*s* intensity ratio curve is not reached, see Section 3.2, Fig. 4. In the biased samples, together with the intensity decrease, the Au $4f_{7/2}$ is shifted from starting 0.23 eV (2.9 at.% Au) to 0.34 eV (1.8 at.% Au) above the Au reference. This increase may be assigned to the erosion of the bald surface Au clusters.

Carbon core level in both grounded and biased sample shows shift towards lower binding energies with Ar^+ ion sputtering (Fig. 3.16). The negative shift is more pronounced in the grounded sample (0.27 eV) than in the biased one (0.13 eV). This difference may be explained by higher sp^2-coordinated carbon content in as-deposited biased sample. At zero sputtering time, biased sample C 1*s* level is registered at 284.7 eV, and the grounded one at 284.8 eV. The biased sample was already subjected to the Ar^+ ion bombardment during the deposition process, and further sputtering does not affect it as much as it does the grounded one.

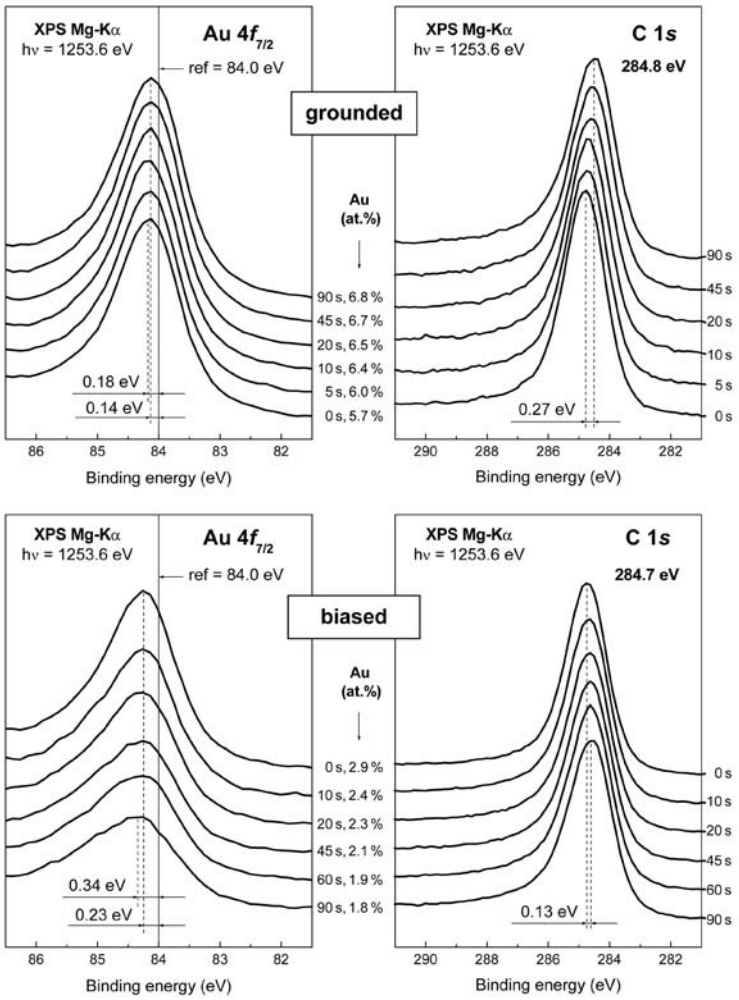

Fig 3.16. Evolution of the Au $4f_{7/2}$ and C 1*s* core levels with Ar^+ ion sputtering time and appropriate Au content development in the grounded and biased sample of *a*-C:H/Au. Quantitative values of BE shifts are given for starting (0 s) and ending (90 s) spectra. Absolute binding energies of C 1*s* core level for both samples before sputtering process beginning are also given.

The UPS He I and He II spectra of grounded and biased *a*-C:H/Au, at the same points on the sputtering time scale, are shown in Fig. 3.17. They provide yet another evidence that Ar^+ ion sputtering does what we postulated, i.e. removes the *a*-C:H cover layer from the topmost clusters in the grounded samples, and erodes the bald surface clusters in the biased ones. The grounded sample He I and He II spectra show that, with sputtering time, the characteristic features of Au 5*d* band at about 6 eV and 4 eV rises, related to the uncovering of the surface clusters. In the biased sample, the starting characteristic features of gold exposed at the surface are diminished with the sputtering time, in accordance with total Au content decrease. The rise of the DOS in the vicinity of the Fermi edge, in spite of the decrease of Au content and its 5*d* band features, may be additional argument in favor of sp^2/sp^3 coordinated carbon ratio increase, observed by XPS (Fig. 3.16).

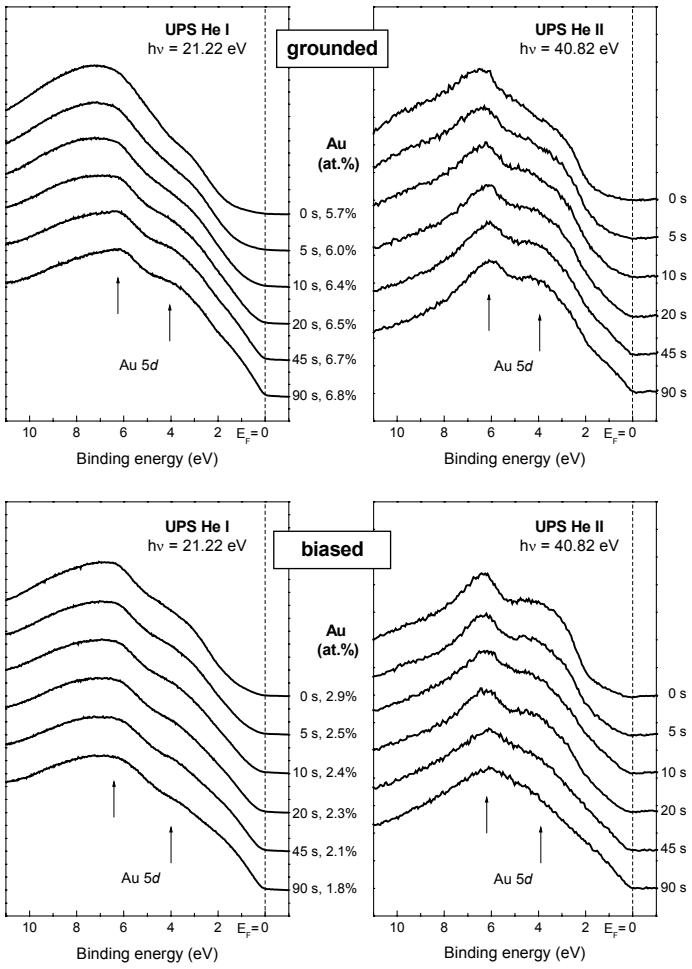

Fig. 3.17. The UPS He I and He II spectra of grounded and biased *a*-C:H/Au sample, with 5.7 at.% Au and 2.9 at.% Au at the beginning of the sputtering process, respectively. The appropriate Au content changes during Ar^+ ion etching are also given.

The *a*-C:H/Ag nanocomposite system, as we mentioned few times already, show tendency of cluster agglomeration at the surface due to the high mobility of Ag atoms. This may be the reason why Ag $3d_{5/2}$ core level, shown in Fig. 3.18, does not show significant change in BE position during the Ar^+ ion treatment. In both grounded (12.0 at.% Ag) and biased case (5.0 at.% Ag) the Ag $3d_{5/2}$ core level remain on its starting BE values of 0.14 eV and 0.34 eV, respectively.

The binding energy of the carbon C 1*s* core level in *a*-C:H/Ag, however, decreases significantly, particularly in the grounded case, where the total shift from the starting (285.1 eV) to the ending sputtering point equals 0.52 eV. The biased sample C 1*s* is less shifted, for 0.30 eV from the beginning at 285.0 eV, see Fig. 3.18. We have already given the possible reason of this effect in Paragraph 3.5.1: due to the mobility of Ag atoms, the compressive stress is not as high as e.g. in *a*-C:H/Au, and therefore, as-deposited film is not so rich in sp^2-coordinated carbon. Hence, a pronounced increase of its content during the Ar^+ ion sputtering takes place.

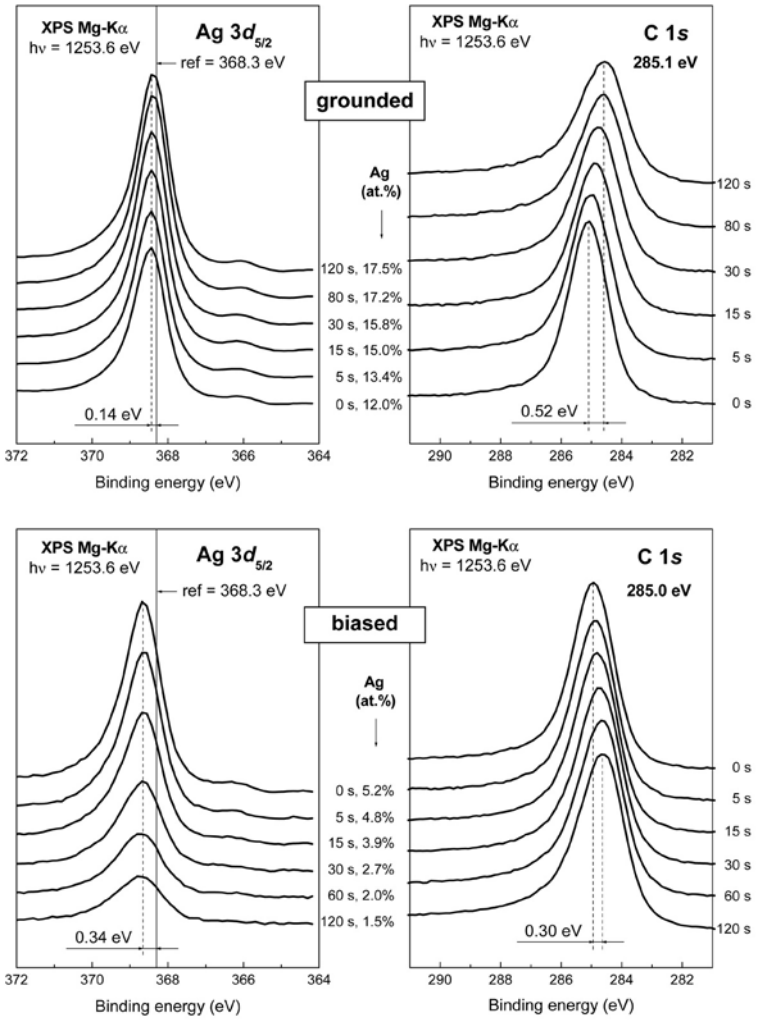

Fig 3.18. Ag $3d_{5/2}$ and C 1*s* core levels evolution with Ar^+ ion sputtering time and appropriate Ag content development in the grounded and biased sample of *a*-C:H/Ag. Quantitative values of BE shifts are given for starting (0 s) and ending (120 s) spectra. The binding energies of C 1*s* core level for both samples before sputtering process beginning are also given.

Valence band spectroscopy during Ar^+ ion sputtering of grounded and biased *a*-C:H/Ag sample with as-deposited content of 12.0 at.% Ag and 5.0 at.% Ag, respectively, is shown in Fig. 3.19. In the grounded sample, both He I and He II spectra show clear rise of the Ag 4*d* band with ongoing etching process, yet again evidencing on uncovering of the surface Ag clusters. The 5.0 at.% biased sample, with decreasing Ag content revealed by XPS, show decrease in Ag 4*d* band intensity. In valence band spectroscopy of *a*-C:H/Ag, thanking to the favorable position of the Ag 4*d* band that does not mask the π-states of carbon at about 3 eV, the *a*-C:H matrix alteration during sputtering process can be also observed. In both 12.0 at.% Ag grounded and 5.0 at.% Ag biased samples, with ongoing sputtering the rise of the π-states is observed, evidencing on increasing sp^2/sp^3 coordinated carbon ratio, in agreement with the negative BE shift of the C 1*s* core level in XPS spectra (Fig. 3.18).

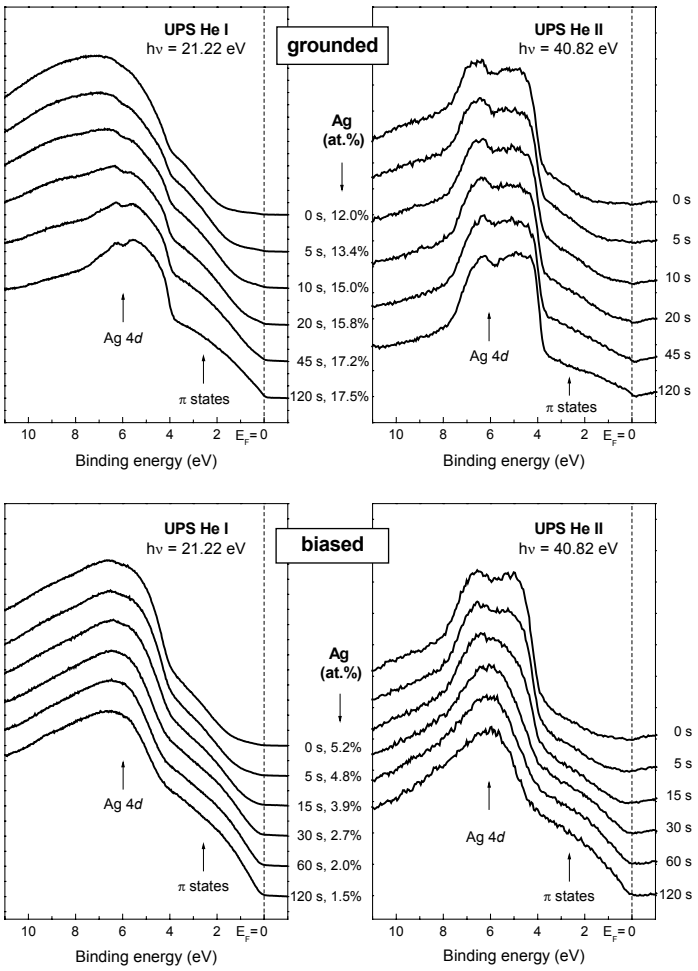

Fig. 3.19. Sputtering time evolution of the UPS He I and He II spectra of grounded and biased *a*-C:H/Ag sample, with as-deposited contents of 12.0 at.% Ag and 5.0 at.% Ag, respectively. The assigned Ag contents revealed by XPS are also given.

The evolution of the Cu $2p_{3/2}$ and C 1*s* core levels in Ar^+ ion sputtered *a*-C:H/Cu is shown in Fig. 3.20. An interesting behavior is observed in the Cu $2p_{3/2}$ core level in the grounded sample with 7.9 at.% Cu. Starting from 0.63 eV above the reference binding energy, the increase of the metallic content with Ar^+ ion sputtering is followed by the slight decrease of Cu $2p_{3/2}$ binding energy towards reference position. Passing the maximum in the Cu $2p_{3/2}$/C 1*s* intensity ratio curve at 90s sputtering time, see Fig. 3.15, the decrease in Cu content is again followed by the increase of the Cu $2p_{3/2}$ binding energy, so the ending point is shifted back to the 0.63 eV above the reference. The Cu $2p_{3/2}$ core level spectrum in biased sample (10.0 at.% Cu, as-deposited) show decrease in intensity only, and no changes in BE position.

Similarly to *a*-C:H/Ag, C 1*s* core level in *a*-C:H/Cu show pronounced shift towards lower binding energies with Ar^+ ion sputtering (Fig. 3.20). Measured as-deposited at 285.2 eV, after 300 s of bombardment the C 1*s* peak is shifted in negative direction for 0.61 eV. Again, this effect is less pronounced with the biased sample, which C 1*s* core level is detected at 285.1 eV after deposition, and is shifted

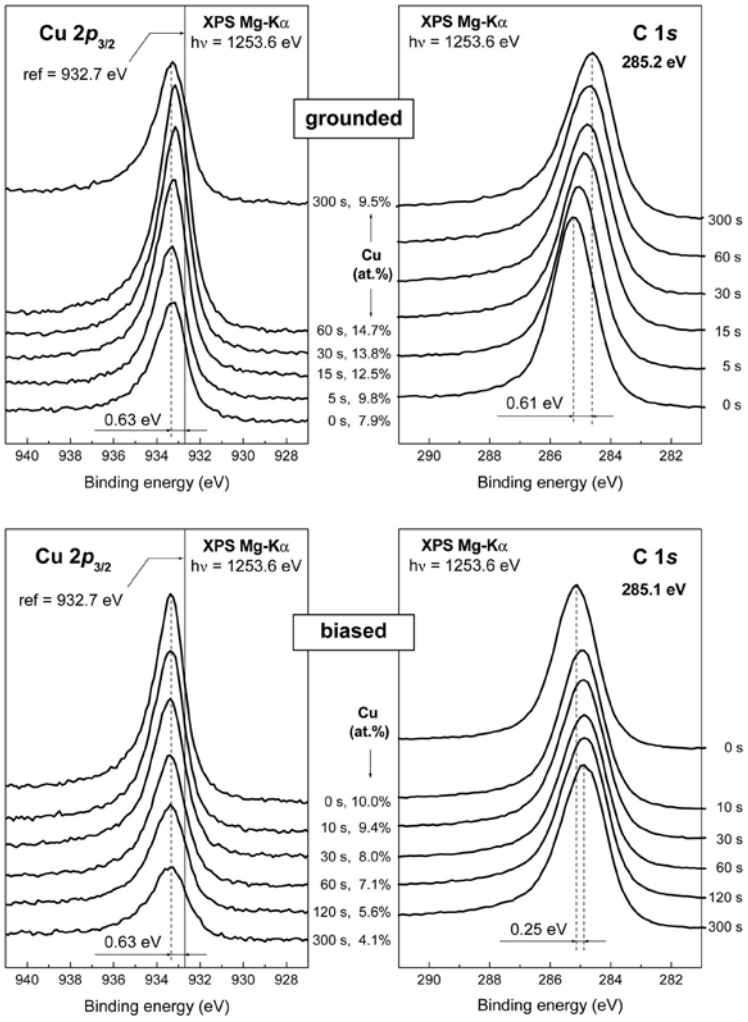

Fig 3.20. The development of the Cu $2p_{3/2}$ and C 1*s* core levels with Ar^+ ion sputtering time and appropriate Cu content in the grounded and biased sample of *a*-C:H/Cu. Quantitative values of BE shifts are given for starting (0 s) and ending (300 s) spectra. The as-deposited binding energies of C 1*s* core level for both samples are also given.

during 300 s of etching for 0.25 eV. Essentially the same reasons for this kind of C 1*s* core level evolution are already discussed for *a*-C:H/Au and *a*-C:H/Ag nanocomposite systems.

Finally, the UPS He I and He II spectra of the *a*-C:H/Cu grounded sample 7.9 at.% Cu and its biased counterpart of 10.0 at.% Cu are shown in Fig. 3.21. The grounded sample spectra follow the XPS-revealed increase of the Cu content in the sample due to the surface clusters uncovering up to the 90 s of the sputtering time. After this maximum, the Cu 3*d* band at about 3.5 eV decreases. The peculiarity of these spectra is, however, the rise of the kink at the binding energy of about 9 eV after long sputtering time. This feature belongs to the excitation of the Ar 3*p* level (8.7 eV), and evidences on Ar incorporation in the *a*-C:H/Cu film after longer (90 s and 300 s) bombardment. Similar effect is observed by Reinke *et al.* [112] in their study of the structural changes of diamond and amorphous carbon under Ar^+ ion irradiation. Biased sample valence band spectroscopy shows development that evidences, in

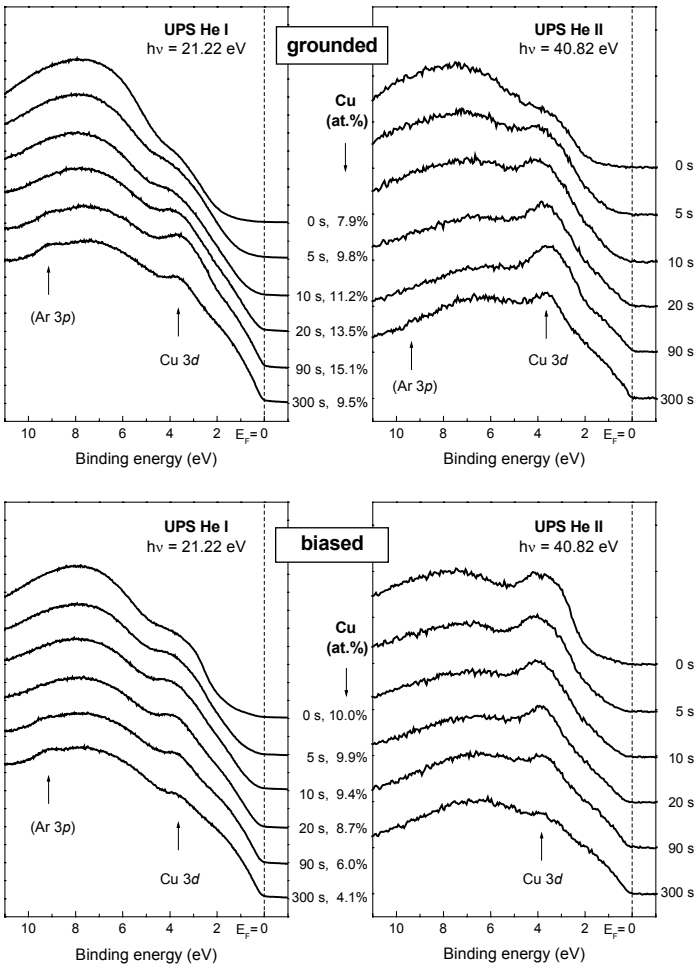

Fig. 3.21. Evolution of the UPS He I and He II spectra of grounded and biased *a*-C:H/Cu sample, with as-deposited contents of 7.0 at.% Cu and 10.0 at.% Cu, respectively. The assigned Cu contents revealed by XPS are also given. At sputtering times of 90s and 300 s a kink that originates from excited Ar 3*p* level of incorporated argon is observed.

agreement with XPS data, on the decrease of the Cu content, increase of the DOS near the Fermi edge that indicate increase of sp^2/sp^3 coordinated carbon ratio, and the same Ar 3*p* - originated kink after long Ar^+ ion sputtering, see Fig. 3.21.

At the end of this extended review of the PES results obtained by *in situ* Ar^+ ion sputtering, we would like to remind once again to the behavior of the states in the vicinity of the Fermi edge in the UPS spectra in all our samples. One or another way exposed to the argon ion bombardment, i.e. during the deposition or *in situ* etched, that process is followed by the rise of the states near the Fermi edge, evidencing on the increased sp^2/sp^3 coordinated carbon ratio in the *a*-C:H component of our nanocomposite materials. The enlarged Fermi edge regions of all He I UPS spectra given in Figs. 3.17, 3.19, and 3.21 are jointly shown in Fig. 3.22.

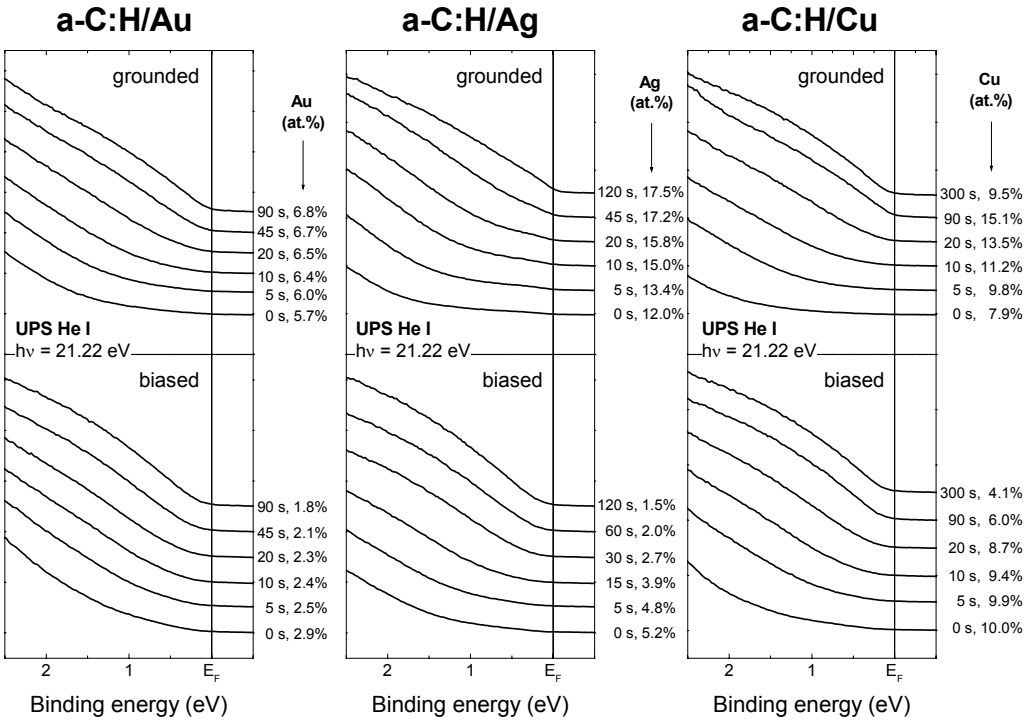

Fig. 3.22. The Ar^+ ion sputtering time evolution of the states in He I spectra in the vicinity of the Fermi edge, in low metal-content *a*-C:H nanocomposite systems deposited on grounded and biased substrates.

3.5.4. Influence of the sample exposure to the air

In several occasions so far we intimated the possible surface clusters coalescence, particularly silver ones, due to their high mobility within the matrix and on the sample surface. We implied this effect is pronounced upon sample exposure to the atmospheric conditions. A tendency of silver to create larger agglomerates has been also observed in other host matrices, like TiN [118], ion-sputtered carbon [119], Al_2O_3 [120] and polymers [121]. It was also observed that noble metals like copper, which have strong tendency to diffuse into polymer matrix during annealing [122-126], when found on the polymer surface diminish that diffusion [127,128]. The cohesive energy of metals overwhelms their interaction with polymer matrix. In addition, the Au nanostructures show decrease in size and area in the air and moderate vacuum, and relative stability in the UHV [129,130]. In the UHV conditions, the coalescence of nanometer Ag islands deposited by filtered arc technique on ZnO- and TiO- covered glass substrates was reported by Byon *et al.* [131]. Layson and coworkers [132,133] have shown that in the air conditions molecular oxygen is directly responsible for post-deposition coarsening and formation of Ag islands on Ag (100) surface.

In this work we aroused the suspicion that some of the results obtained on our noble metal-containing *a*-C:H nanocomposites may be due to the surface agglomeration of metallic clusters. To check out this assumption, with all three nanocomposite systems, we have undertaken a PES study that comprised XPS and UPS of: 1. *as-deposited* grounded and biased samples, 2. same samples after about *20 hours dwell in the ultra-high vacuum* (UHV), 3. same samples after about *20 hours residence in the air*. For this purpose, the samples of *a*-C:H/Au, *a*-C:H/Ag, and *a*-C:H/Cu have been deposited, with *in vacuo* measured metal contents as follows: grounded samples of 10.5 at.% Au, 7.9 at.% Ag , and 7.0 at.% Cu and their biased counterparts of 4.8 at.% Au, 1.2 at.% Ag, and 8.8 at.% Cu. To get an overview of this experiment, in Fig. 3.23 we present survey XPS spectra of as-deposited grounded samples in UHV, and the same samples after about 20 hours in the air. For the clarity of the figure, a Shirley background is subtracted from each spectrum. The common features that one observes in all spectra are the C 1*s* peak at about 285 eV and a low-kinetic energy C KLL Auger peak at the BE of about 990 eV. At the far right hand-side of the energy scale, an x-ray excited valence band (VB) of each sample is observed. After exposure to the air, in all samples the rise of oxygen O 1*s* core level at about 532 eV and O KLL Auger peak at about 743 eV is detected. UHV spectra of all samples show presence of peaks characteristic for deposited material only and *no other impurities*, including e.g. oxygen from residual gas in the deposition chamber, or contamination during the transfer from the deposition to the PES measurement chamber. After exposure to the air, apart from the native oxide, no further impurities are observed. Due to the oxide layers at the surface, all metallic and carbon peaks are decreased in intensity in comparison to the UHV spectra. The total amount of oxygen was about 8 at.% in *a*-C:H/Au and *a*-C:H/Ag, and 15% in *a*-C:H/Cu.

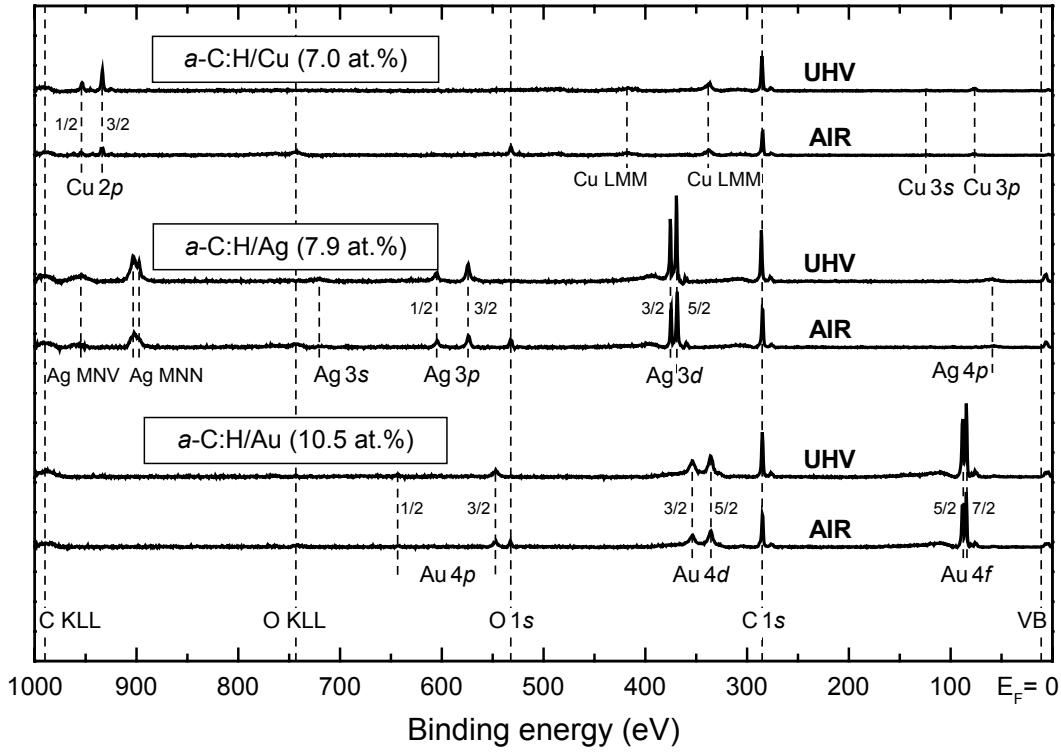

Fig. 3.23. Survey XPS of the *a*-C:H/Au, *a*-C:H/Ag, and *a*-C:H/Cu in UHV conditions and after exposure to the air. The common features of C 1*s*, C KLL, O 1*s*, and O KLL are drawn in all spectra. The core levels of Au, Ag, and Cu are observed only, with no other impurities. The decrease in intensity of metallic and C 1*s* peaks upon exposure to the air is observed.

To reveal the influence of the sample exposure to the air, we will once again consider higher resolution and statistics core level and valence band spectroscopy, starting as usual, with *a*-C:H/Au. Figure 3.24 shows Au $4f_{7/2}$ and C 1*s* core level spectroscopy of *a*-C:H/Au grounded sample of 10.5 at.% Au and its biased counterpart of 4.8 at.% Au. The scattered data points represent as-deposited and the measurement after 20 h in the UHV, while the solid line represents a measurement after 20 h in the air. In the Au $4f_{7/2}$ spectroscopy, apart from the usual shift of the core level from the reference position in Au nanoclusters-containing samples (see Section 3.1), a very good matching of all three sets of data is obtained in both grounded and biased samples. These spectra evidence that Au clusters did not undergo the major changes either after 20 h in the UHV, or even exposed to the air. The Au content measured after 20 h dwell in the air was 10.2 at.% and 4.6 at.% in the grounded and biased sample, respectively (the oxygen peak is ignored in the “air” samples).

The C 1*s* core levels in both samples are detected at the binding energy of 284.7 eV. After 20 hours in the UHV, no observable changes in both spectra are encountered. However, taking sample out of the UHV, and after 20 h dwell in the air, the C 1*s* peak of the grounded sample was shifted for 0.20 eV towards lower binding energies, and the C 1*s* of the biased one – for 0.12 eV in the same direction. It is not clear what causes this shift. We could envisage a number of reasons, some of them

being: air-induced increase of sp^2-coordinated carbon, C–O and C–N bonds, or some unidentified hydrocarbon impurity from the atmosphere.

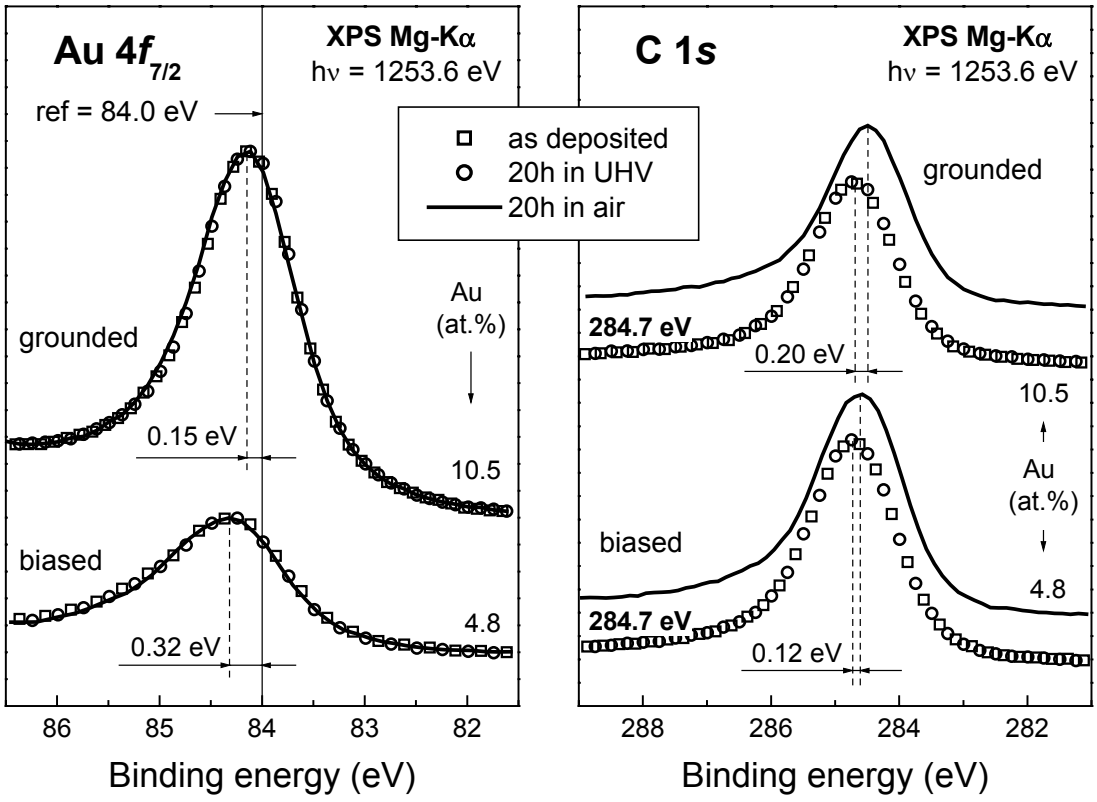

Fig. 3.24. The Au $4f_{7/2}$ and C 1*s* core-level spectra of grounded and biased *a*-C:H/Au samples: as-deposited (squares), after 20 h in the UHV (circles), and after 20 h in the air (solid line). The *in vacuo* Au contents and absolute C 1*s* BEs are given. After 20 h in the air a shift in the C 1*s* position towards lower BEs is observed, being higher in the grounded case.

The UPS spectra of *a*-C:H/Au 10.5 at.% grounded sample and its biased counterpart of 4.8 at.% Au, under same conditions, are shown in Fig. 3.25. After 20 h in the UHV, both He I and He II spectra of the grounded sample do not seem to be altered, reproducing the familiar shape from Figs. 3.2 and 3.13. The He I and He II spectra of the biased sample, immediately after deposition showed increased Au 5*d* band features. The increase of sp^2/sp^3 coordinated carbon ratio that is observed in C 1*s* negative BE shift (Fig. 3.12), which would have been represented in UPS by the rise of the π-states at about 3.5 eV, was covered by strong Au 5*d* band features. After 20 h of relaxation time in the UHV, however, the DOS at about 3 – 4 eV is slightly reduced. This effect may be attributed to the catalytic activity of Au nanoparticles exposed on the biased sample surface. They may be able to break some H_2 molecules from the residual gas in the UHV and adhere some hydrogen to the *a*-C:H component of the sample, therefore reducing the p-states of carbon. After 20 h in the air, He I spectra of both samples look alike, while He II spectra reveal higher Au exposure at the surface in the biased sample.

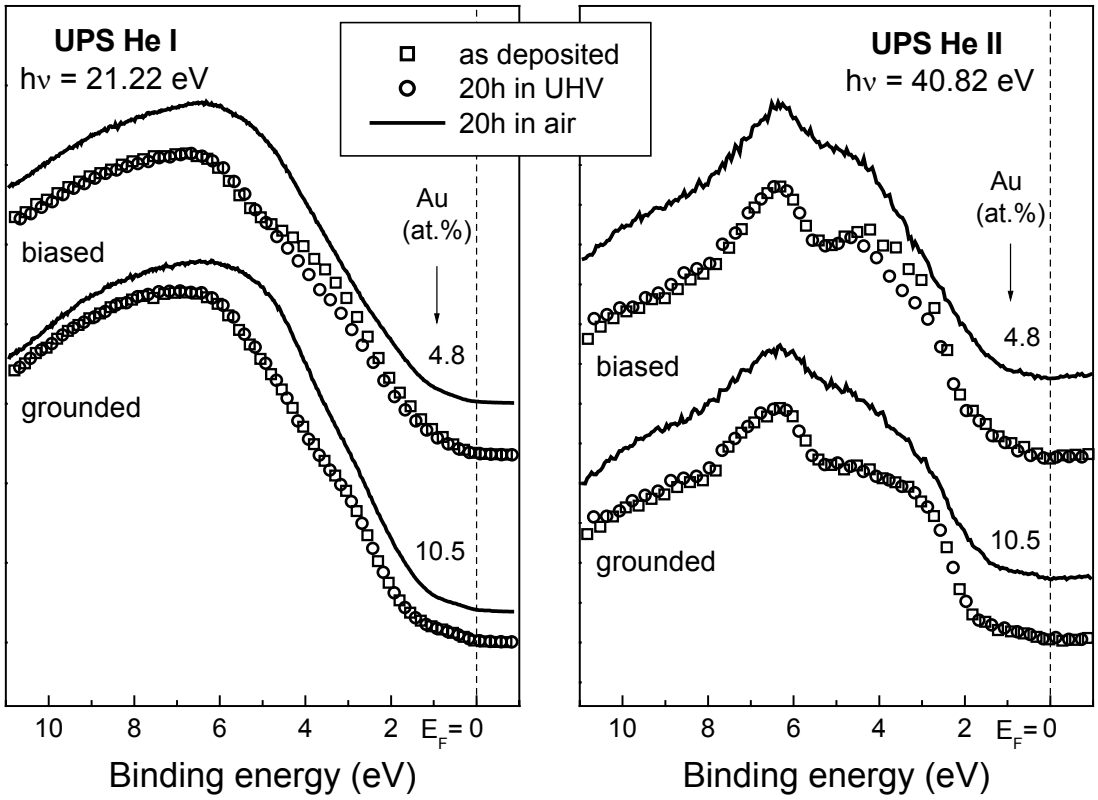

Fig. 3.25. Normalized He I and He II UPS spectra of grounded and biased *a*-C:H/Au samples: as-deposited (squares), after 20 h in the UHV (circles), and after 20 h in the air (solid line). The *in vacuo* Au contents are given. After 20 h in the UHV a decrease in the π-states of carbon in the biased sample is observed.

The most interesting system, both from our previous results, and from the other references, should be *a*-C:H/Ag. The Ag $3d_{5/2}$ and C 1*s* core level spectroscopy of the grounded (7.9 at.% Ag) and biased sample (1.2 at.% Ag) are given in Fig. 3.26. The Ag $3d_{5/2}$ peak in both samples, immediately after deposition and after 20 h in the UHV, showed no observable alterations. Due to the low intensity, the biased sample spectra are given with intensity magnification factor of 10 in Fig. 3.26. Exposing the samples to the air for 20 h introduces significant changes in the Ag nanocluster structure, though Ag content was not significantly altered: 7.4 at.% in the grounded and 1.3 at.% in the biased case. In the grounded sample, the Ag $3d_{5/2}$ core level is shifted towards lower binding energies for 0.13 eV. In the biased sample this shift is as high as 0.41 eV. If we recall Eq. (3.2), we can make the following estimation: in the grounded 7.9 at.% Ag sample, the cluster diameter of 1.0 nm in the UHV conditions, after exposure to the air is increased to 5.6 nm; in the biased 1.2 at.% Ag case, the cluster size of 0.7 nm in the UHV conditions is increased to 1.6 nm in diameter after 20 h dwell in the air. The air-induced coalescence, therefore, increases the Ag clusters volume for the factor of about 170 in the grounded and 12 in the biased case. The absolute values are, of course, questionable and disagree with

GISAXS data, but the difference in relative increase of the cluster volume of *one order of magnitude* between grounded and biased cases may offer the answers to the number of questions aroused in this work. Some of them are: (1) increased surface roughness in the grounded *a*-C:H/Ag 12.0 at.% in comparison with fairly flat *a*-C:H/Au 8.6 at.% grounded sample encountered by direct imaging techniques (Sections 3.2 and 3.3), (2) the lack of correlation between Ag clusters in GISAXS pattern of the same 12.0 at.% Ag grounded sample (Section 3.4), and (3) the pronounced Ag 4*d* band even in low-metallic content samples (Figs. 3.2 and 3.13).

The carbon C 1*s* core level in *a*-C:H/Ag undergoes even higher shift towards lower binding energies after exposure to the air (Fig 3.26) than the C 1*s* in *a*-C:H/Au. Measured as-deposited in the grounded 7.9 at.% Ag sample at 285.2 eV, and in the biased 1.2 at.% Ag sample at 285.0 eV, after 20 h residence in UHV, C 1*s* core levels did not suffer from any change. Exposed 20 h to the air conditions, however, the C 1*s* core level was shifted to the lower binding energies for 0.52 eV in the grounded sample, and for 0.21 eV in the biased one. Again, one may speculate on the reason for this behavior of the C 1*s* core level. One of them should certainly be the structural change in the *a*-C:H matrix due to the redistribution of surface Ag clusters.

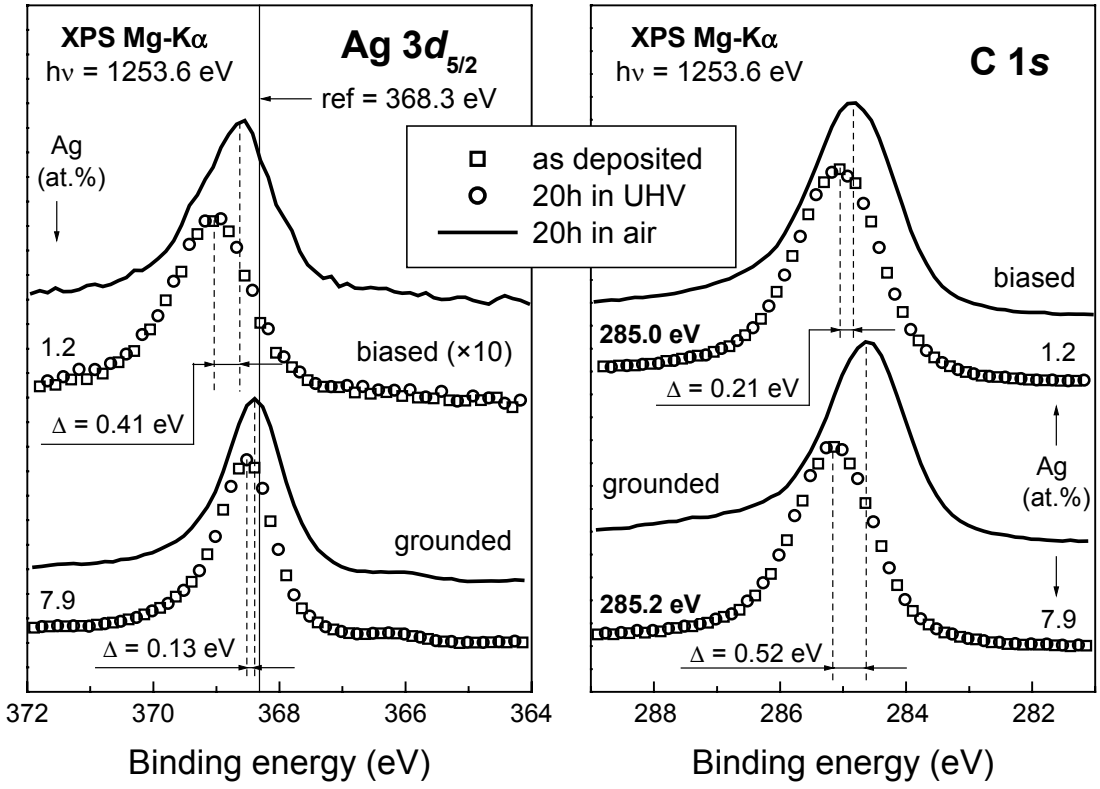

Fig. 3.26. The Ag $3d_{5/2}$ and C 1*s* core-level spectra of grounded and biased *a*-C:H/Ag samples: as-deposited (squares), after 20 h in the UHV (circles), and after 20 h in the air (solid line). A large shift of the Ag $3d_{5/2}$ core level towards lower binding energies is observed after 20 h sample dwell in the air. The *in vacuo* Au contents and absolute C 1*s* BEs are given. A shift in the C 1*s* position towards lower BEs is observed, being higher in the grounded case.

The UPS He I and He II spectra of the same grounded and biased samples of *a*-C:H/Ag are shown in Fig. 3.27. After 20 h in the UHV, just like the core levels, neither of spectra of both samples seemed to be changed, again reproducing the familiar shape from Figs. 3.2 and 3.13. Exposure of the samples to the air for another 20 h introduces alterations that are, more or less, in agreement with our discussion of the core level alterations. In both He I and He II spectra of the grounded 7.9 at.% Ag sample, the valence band spectroscopy reproduces the fact that Ag clusters merged to form larger islands, keeping nearly same total Ag content (7.4 at.%). Therefore, larger areas of *a*-C:H are exposed at the surface, which is reflected in He I and He II spectra as an increase of carbon π-states at about 3.5 eV. The developed shoulder at about 9 eV may be attributed to the broad carbon σ band. Also, the relative intensity of the Ag 4*d* band is decreased (particularly in the He II spectrum) in comparison to the UHV conditions. The biased 1.2 at.% Ag sample also did not suffer from any changes for the first 20 h in the UHV. Exposure to the air for another 20 h results in altered He I and He II spectra, with increased Ag 4*d* band. The carbon features are also increased, but this case should not be taken as a representative due to the very low Ag content of 1.2 at.%.

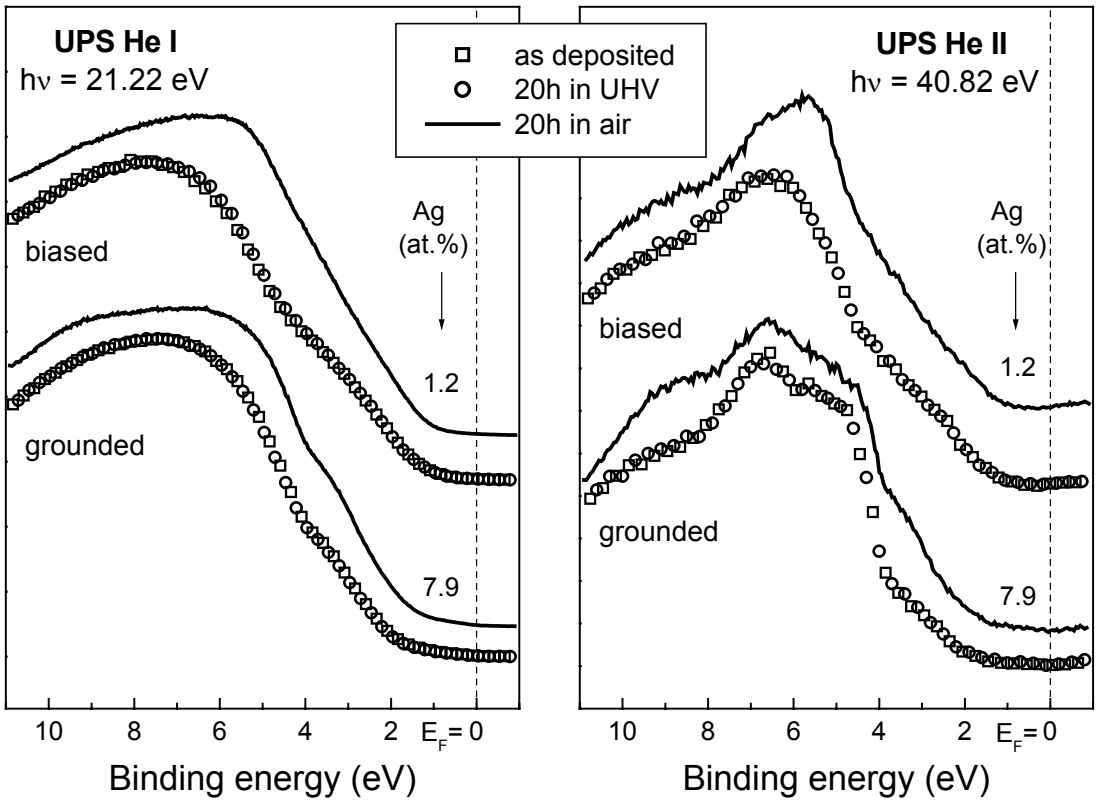

Fig. 3.27. Normalized He I and He II UPS spectra of grounded and biased *a*-C:H/Ag samples: as-deposited (squares), after 20 h in the UHV (circles), and after 20 h in the air (solid line). The *in vacuo* Ag contents are given. After 20 h in the air grounded sample shows increased carbon features in comparison to the Ag 4*d* band. The biased sample shows higher exposure of Ag at the surface.

Copper is an oxidizing metal and this fact is reflected in this experiment with *a*-C:H/Cu. Figure 3.28 shows grounded sample with 7.0 at.% Cu and its biased counterpart with 8.8 at.% Cu. 20 h of dwell time in UHV does not change Cu $2p_{3/2}$ peak in either of the samples, in comparison to as-deposited measurements. In both grounded and biased as-deposited samples the Cu $2p_{3/2}$ core level is shifted towards higher binding energies for 0.58 eV. This equal shift from the reference position is typical for *a*-C:H/Cu, see Fig. 3.12. Exposed to the air, both grounded and biased copper core levels show degradation related to the oxidation. The Cu $2p_{3/2}$ core level does not seem to be shifted, but it shares its intensity with the Cu $2p_{3/2}$ in CuO at 1.8 eV higher BE, and with a shake-up at about 944 eV. Altogether, the Cu content measured after 20 h in the air (taking into account all three features that appear) did not change very much: 10.3 at.% in the grounded and 6.6 at.% in the biased sample.

The C 1*s* core level follows the trend that we already had with both *a*-C:H/Au and *a*-C:H/Ag. Detected as-deposited at the BEs of 285.2 eV and 285.1 eV in the grounded and biased cases, respectively, after 20 h in the UHV no changes in both samples are observed. After 20h dwell in the air, the C 1*s* of the grounded sample is shifted towards lower binging energies for 0.49 eV, and C 1*s* of the biased sample for 0.23 eV. Similar values of the negative BE shift we encountered in the grounded and biased *a*-C:H/Ag samples.

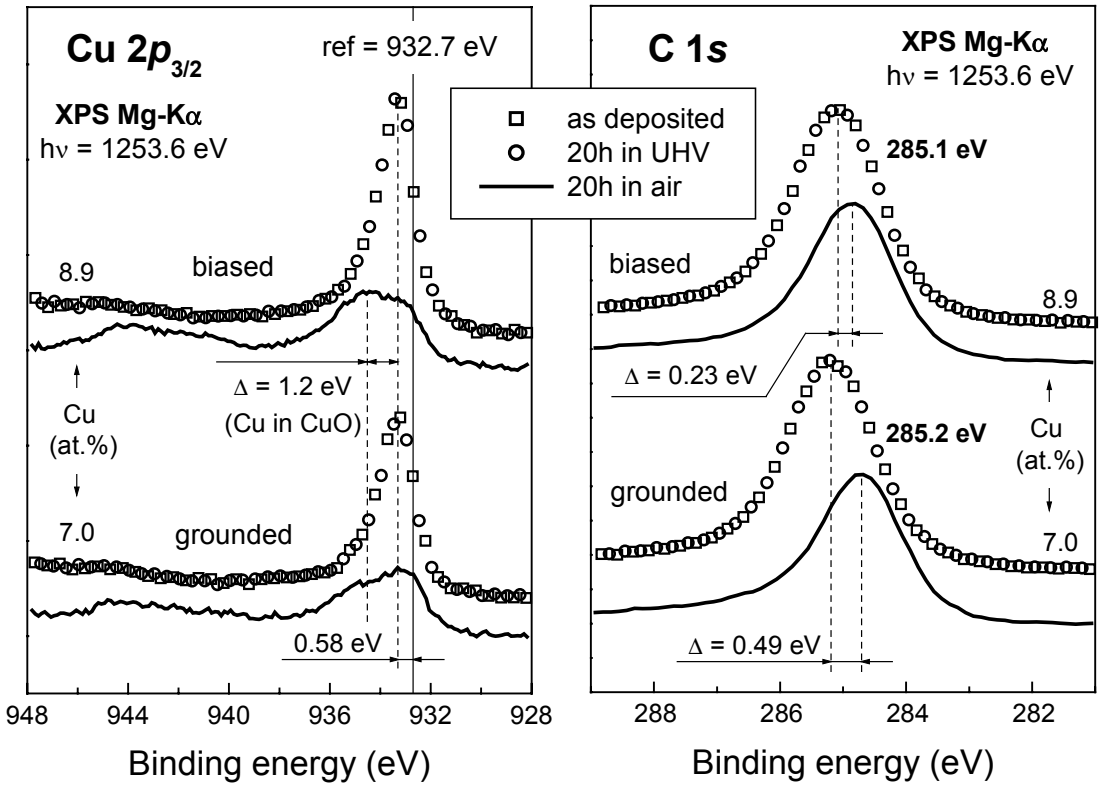

Fig. 3.28. The Cu $2p_{3/2}$ and C 1*s* core-level spectra of grounded and biased *a*-C:H/Cu samples: as-deposited (squares), after 20 h in the UHV (circles), and after 20 h in the air (solid line). The *in vacuo* Au contents and absolute C 1*s* BEs are given. The Cu $2p_{3/2}$ after 20 h in the air reveals oxidized copper. The C 1*s* shifts are similar to those in *a*-C:H/Ag.

The valence band spectroscopy of the same grounded and biased *a*-C:H/Cu samples is shown in Fig. 3.29. The He I and He II spectra revealed once again that as-deposited and samples kept for 20 h under UHV conditions do not differ, with valence band spectra matching very well. In both He I and He II spectra, a typical *a*-C:H/Cu shape is reproduced, with increased feature at about 4 eV that originates from the Cu 3*d* band and is more pronounced in the biased spectra, the case we already had (Figs. 3.2 and 3.13). After exposure to the air for 20 h, quite altered valence band spectra occurred, being mutually almost identical for grounded and biased sample. Therefore, we believe they primarily originate from copper oxide.

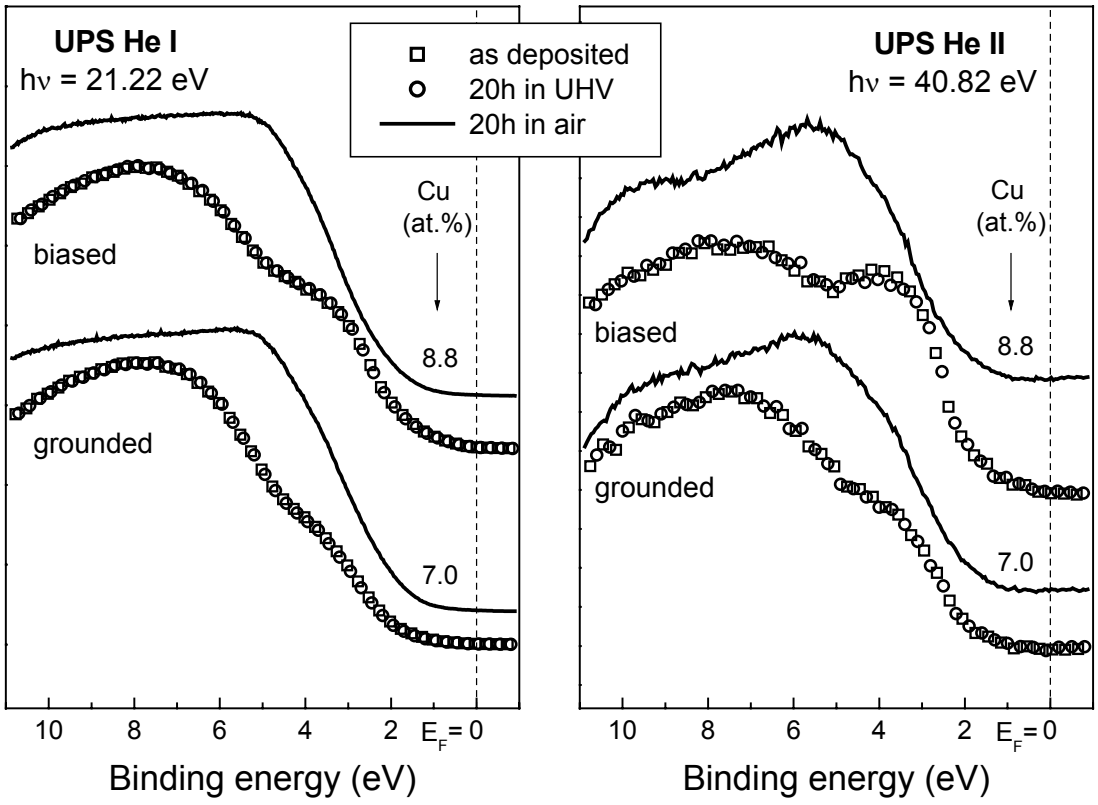

Fig. 3.29. Normalized valence band spectroscopy of grounded and biased *a*-C:H/Cu samples: as-deposited (squares), after 20 h in the UHV (circles), and after 20 h in the air (solid line). The *in vacuo* Cu contents are given. After 20 h in the air quite altered and also mutually almost identical results occurred in ground and biased He I and He II spectra.

Completing the survey of the experimental data related to the influence of the samples exposure to the air, we would like to draw a common line as follows. In all our nanocomposite systems, the XPS and UPS spectra recorded immediately after deposition and after 20 h sample dwell in the UHV, yield almost identical results. The samples structure seems to be “frozen” in the vacuum conditions. More or less significant alterations take place when the sample is taken out of the UHV and exposed to the air for another 20 hours. The Au $4f_{7/2}$ showed no changes at all, revealing preserved cluster structure from the UHV conditions. The Ag $3d_{5/2}$ shows shifts towards

lower binding energies, indicating strongly enhanced cluster coalescence under air conditions. Copper oxidizes in the air. In all samples, the C 1*s* core level in the air conditions show shift towards lower binding energies. This shift is always higher in the grounded than in the biased samples. Being lower in the *a*-C:H/Au than in *a*-C:H/Ag and *a*-C:H/Cu, air-induced C 1*s* shift follows the tendency that is encountered in intercomparison of grounded and biased counterparts (Fig. 3.12), as well as in the C 1*s* core level evolution during *in situ* Ar^+ ion bombardment of the samples (Figs 3.16, 3.18, and 3.20).

Before we leave this topic, it is worthwhile to revisit once again XPS spectra of grounded and biased *a*-C:H/Cu that is, as we said, oxidized after 20 h in the air. Even at the first glance in Fig. 3.28, it is obvious that the grounded and biased *a*-C:H/Cu samples show the Cu $2p_{3/2}$ core level in Cu and in CuO with different contributions. In Fig. 3.30, we enlarged this region of the both spectra and applied a deconvolution procedure using Doniach-Šunjić algorithm [134], corrected for the Shirley background [90]. The convolution profiles fit very well the Cu $2p_{3/2}$ peak in Cu (933.1 eV) and in CuO (934.9 eV) in both grounded and biased case. The contribution of each profile in the convolved one reveals difference in the grounded and biased samples: in the ground sample the contribution of Cu $2p_{3/2}$ from copper is 70%, and from CuO 30%. Biased sample deconvolution reveals lower Cu $2p_{3/2}$ intensity from copper, with contribution of 58% and increased influence of 42% of the CuO-originated Cu $2p_{3/2}$ peak. The higher amount of oxidized copper at the surface of the biased sample confirm once again, and moreover may represent one of stronger arguments of the coverage of surface Cu clusters with a layer of *a*-C:H in the grounded sample, and their baldness in the biased one.

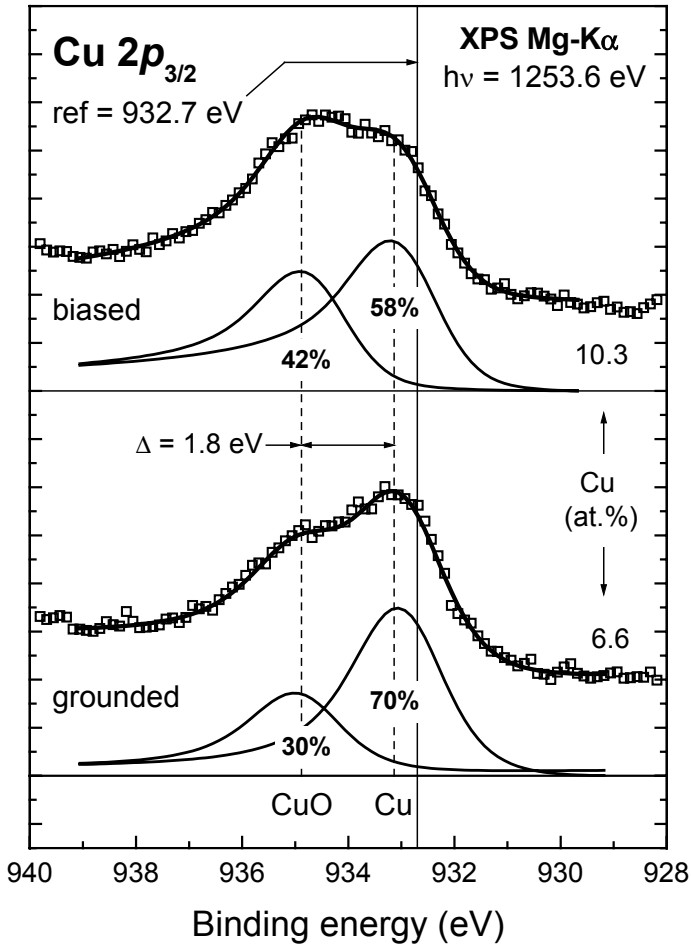

Fig. 3.30. The Cu $2p_{3/2}$ peak after exposure of the grounded and biased sample to the air. Deconvolution of the Cu- and CuO-originated Cu $2p_{3/2}$ core level reveals higher amount of oxidized copper in the biased sample, confirming its clusters baldness at the surface.

3.5.5. XPS study of thiophene adsorption

The last in the series of our PES-based experimental tests aimed to reveal whether topmost noble metal clusters in nanocomposites with *a*-C:H are covered with a tiny matrix layer or not is based on the known tendency of sulfur to bind with noble metals. A number of chemical studies has been undertaken to investigate bonds between noble atoms and sulfur-containing organic compounds [135-138]. For this test, we have selected thiophene (C_4H_4S), with structural formula given in Fig. 3.31. The idea behind this experiment was to cover our samples with a layer of thiophene, and to study them again by XPS. The amount of sulfur detected at the surface should provide information on the exposure of topmost metallic clusters, i.e. if the clusters are bald on the surface, more sulfur is expected to be bound to them, and *vice versa*.

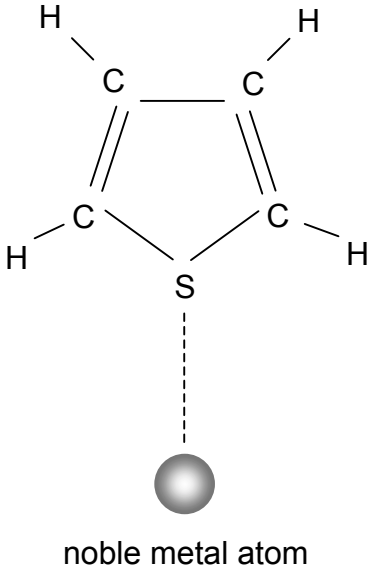

Fig. 3.31. Structural formula of thiophene (C_4H_4S) and its prospective bond to a noble metal atom.

The experiment was made *ex vacuo*, by putting several drops of liquid thiophene (Fluka, purity >98%) on our samples so that entire area is covered. After complete evaporation of the liquid, samples are put again into UHV and subjected to XPS analysis. In general, very little amount of sulfur is detected at the surface, at maximum about 5 at.%. As a consequence, a noisy XPS signal of the S 2*p* region is obtained, in spite of increased measurement statistics.

Figure 3.32a shows the S 2*p* core levels of sulfur detected on a monocrystalline gold reference sample. After subtraction of the Shirley background, the fitting of the experimental data by convolved Gauss and Lorentz profiles is made using three S $2p_{1/2}$ – S $2p_{3/2}$ doublets with fixed energy separation of 1.18 eV and intensity ratio between j = 3/2 and j = 1/2 components of 1.71 [97]. The best fit values of binding energies of the S $2p_{3/2}$ core level are attributed to S–Au bonds (161.9 eV) [138], sulfur in C_4H_4S (163.8 eV) [97], and S–O bonds (167.8 eV) [139]. Figure 3.32b shows results of the same 3-doublets fitting procedure applied to *a*-C:H/Au grounded samples of 4.6 at.% and 19.4 at.% Au and the biased samples (not counterparts) of 6.3 at.% and 16.8 at.% Au, respectively. The relative content of sulfur measured on each sample is given in the figure and, for clarity, total atomic contents of each nancomposite sample covered with a layer of thiophene are given in Table 3.3 at the end of the paragraph. The amount of detected sulfur in *a*-C:H/Au samples, although very small, is regularly higher in the biased than in the grounded samples. The C_4H_4S-originated S $2p_{3/2}$ is a dominant peak in all spectra. However, more than just a higher relative

concentration of sulfur, the shapes of fitted spectra of 16.8 at.% and 6.3 at.% Au biased samples show a developed shoulder at about 162 eV that originates from S–Au bonds. Therefore, higher content of these bonds in the biased than in the grounded samples can be envisaged and related to the higher gold exposure at the surface.

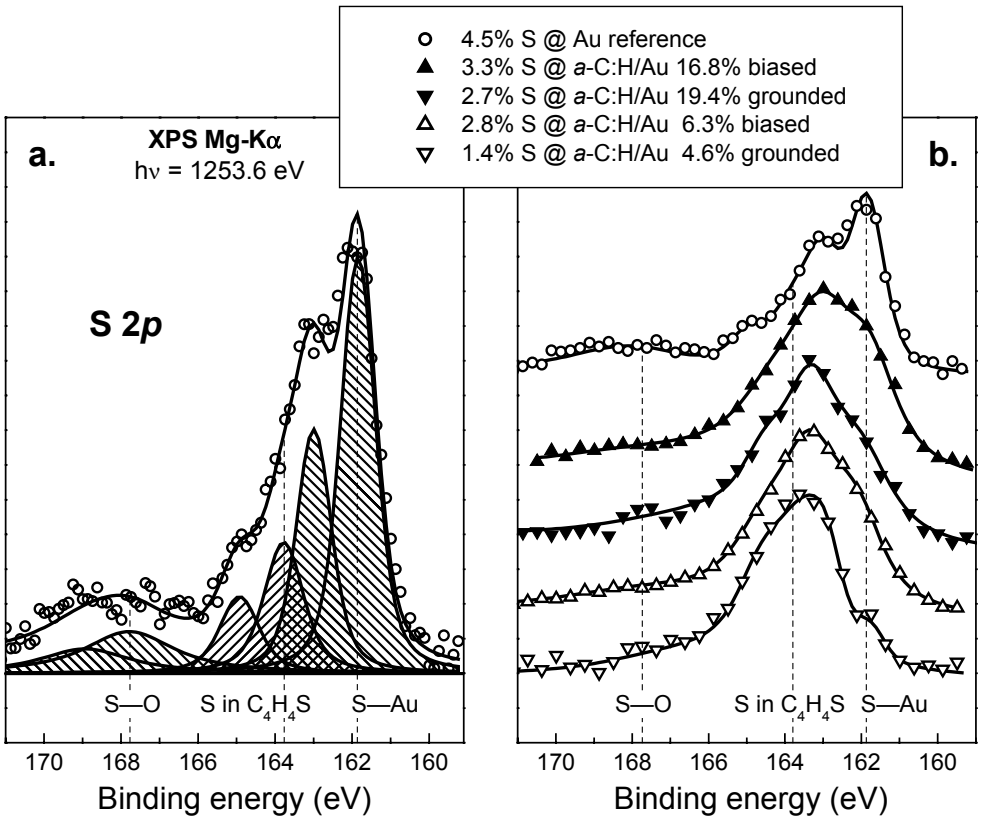

Fig. 3.32. a. Sulfur S 2*p* spectrum at the Au reference sample, fitted with three S $2p_{1/2}$ – S $2p_{3/2}$ doublets and their origin. b. Intercomparison of normalized S 2*p* spectra on two *a*-C:H/Au grounded and two biased samples, together with the thiophene-covered Au reference. A shoulder at about 162 eV, related to S–Au bonds, in both biased samples is observed.

The same 3-doublet fitting procedure is applied to the silver monocrystalline reference sample and two grounded *a*-C:H/Ag samples of 12.0 at.% Ag and 19.9 at.% Ag, and their biased counterparts of 5.0 at.% Ag and 8.6 at.% Ag, respectively. The results of fitting the S 2*p* spectrum after thiophene evaporation from the Ag reference sample are shown in Fig. 3.33a. Again, the S $2p_{3/2}$ position at 161.8 eV is assigned to the S–Ag bonds and the S $2p_{3/2}$ at 164.1 eV to the sulfur in C_4H_4S. The contribution of the S–O bonds at 167.8 eV was negligible in the case of Ag reference sample. All *a*-C:H/Ag samples show strong peak related to sulfur in C_4H_4S, but also, in all spectra the shoulder at about 162 eV related to S–Ag bonds is obvious. The grounded samples adsorbed higher amount of sulfur (see Fig. 3.33b and Table 3.3), what may be explained by already elaborated coalescence of the surface Ag clusters. Also, in the grounded samples the C_4H_4S-related sulfur peak is stronger. Higher

relative contribution of the S–Ag bonds-related peak at 162 eV in the biased 8.6 at.% Ag sample can be envisaged, and hence, a higher exposure of silver at the surface.

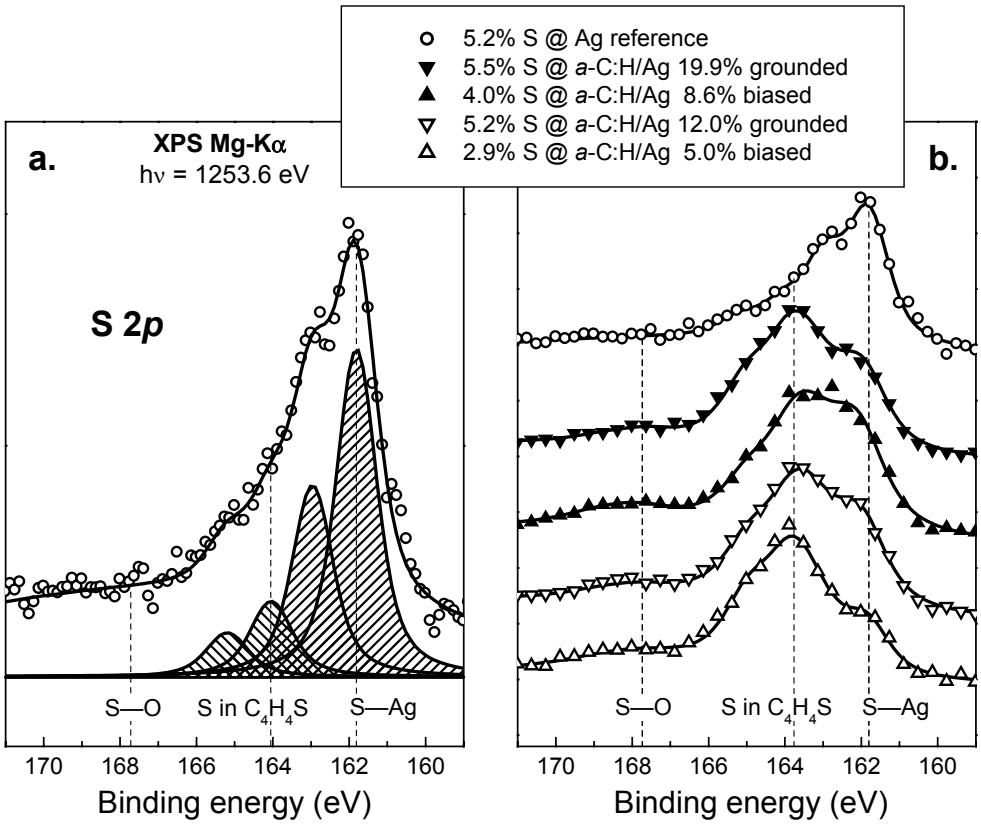

Fig. 3.33. a. Sulfur S 2*p* spectrum at the Ag reference sample, fitted with two S $2p_{1/2}$ – S $2p_{3/2}$ doublets. b. Normalized S 2*p* spectra on *a*-C:H/Ag grounded samples and their biased counterparts, together with the Ag reference. A shoulder at about 162 eV, related to the S–Au bonds, is observed in all *a*-C:H/Ag spectra.

The same experiment is also performed with grounded and biased *a*-C:H/Cu samples, but in both cases only some traces of sulfur from the thiophene itself are detected. This result was expected due to the oxidation of copper, and cannot provide the useful information on the amount of sulfur bonded to the Cu nanoclusters. Therefore, the results of thiophene adsorption on the *a*-C:H/Cu surfaces will be omitted.

The relative atomic contents of all samples exposed to the thiophene adsorption, including grounded and biased pure *a*-C:H samples (for sake of comparison) with extremely low amount of adsorbed sulfur, are given in Table 3.3.

Table 3.3. Relative atomic concentration of elements in the samples subjected to thiophene adsorption. The nominal metallic content is measured *in vacuo*. Within one material, samples are sorted in descending order of sulfur content, preceded by the reference sample.

material	substrate	relative concentration (at.%)		
		C	O	S
a-C:H	grounded	82.4	16.8	0.8
	biased	86.6	13.0	0.4

material	Au content (at.%)	substrate	relative concentration (at.%)			
			Au	C	O	S
Au reference			35.2	45.4	14.9	4.5
a-C:H/Au	16.8	biased	13.4	72.4	10.9	3.3
	6.3	biased	5.1	79.9	12.2	2.8
	19.4	grounded	13.3	71.3	12.7	2.7
	4.6	grounded	3.6	82.9	12.1	1.4

material	Ag content (at.%)	substrate	relative concentration (at.%)			
			Ag	C	O	S
Ag reference			41.6	36.3	16.9	5.2
a-C:H/Ag	19.9	grounded	10.5	64.9	19.1	5.5
	12.0	grounded	8.5	68.0	18.3	5.2
	8.6	biased	5.9	74.6	15.5	4.0
	5.0	biased	2.1	80.1	14.9	2.9

4. Summary and concluding remarks

In this work nanocomposite thin films of amorphous hydrogenated carbon (*a*-C:H) doped with noble transition metals of 1B group (gold, silver, and copper) are studied. The composite materials are obtained by combined magnetron sputtering (MS) of a metal target by argon, and plasma-assisted chemical vapor deposition (PACVD) of methane under vacuum conditions. The Ar/CH_4 mixture in a mass flow ratio of 1.5 was used as an operating gas. This mass flow ratio value shows most efficient reduction the target coverage with carbon atoms during the deposition, so-called "target poisoning effect" (see Paragraph 2.1.1). Particular attention is devoted to the low metal-content *a*-C:H samples, in which metallic inclusions have a form of isolated nanoclusters. Our aim was to reveal surface cluster arrangement, i.e. to figure out whether topmost metallic nanoclusters are covered with a layer of *a*-C:H or are bald on the surface and hence exposed to the surrounding environment. We deposited our samples onto substrates kept on the ground potential and on –150 V dc bias voltage. The differences encountered in the surface structure and nanocluster arrangement between samples, which differed in the deposition process in this parameter only, provided an answer to the question of surface clusters coverage.

The experimental techniques used to reach this goal comprised *in vacuo* and *ex vacuo* photoelectron spectroscopy (PES), direct imaging by atomic force microscopy (AFM) and scanning electron microscopy (SEM), and grazing incidence small-angle x-ray scattering (GISAXS). The majority of work is made in several photoemission experiments, using both x-ray and UV-excited photoelectron spectroscopy (XPS and UPS, respectively).

In the course of the work, series of *a*-C:H/Au, *a*-C:H/Ag, and *a*-C:H/Cu samples, with metallic content varying from zero to 100 at.%, have been deposited and studied *in vacuo* by XPS and UPS (Section 3.1). This kind of study for *a*-C:H/Au has been made before [26] but, to our knowledge, there are no similar studies reported for silver- and copper-containing *a*-C:H. The XPS results of these series show that, with decreasing metal content below the percolation threshold (at about 40-50 at.% of metal concentration), a shift in binding energy (BE) of metal core levels towards higher BEs is observed. With non-carbidic metals like the ones we used in our work, these shifts can be related to their isolated cluster structure in the host matrix. Decrease of the total metal content in the sample is followed by the decrease in the cluster size, which is reflected in increased binding energy of electrons escaping from them (see Paragraph 2.2.2 and Section 3.1, Fig. 3.1).

At the same time, carbon C 1*s* core level is shifted in the opposite direction, towards lower binding energies, and this shift rises as metal content increases in the sample. Negative shift in C 1*s* binding energy reveals increased relative content of sp^2-coordinated carbon in the *a*-C:H matrix, which, we believe, should be attributed to the compressive stress that metallic inclusions introduce in the host *a*-C:H, being

higher with higher metal content in the sample. Another possible reason is catalytic reduction of hydrogen in the *a*-C:H matrix with increasing metallic content.

UPS of the same series (Fig. 3.2) showed increased relative contribution of metal valence band features with increased metal content. A peculiar case in these series is *a*-C:H/Ag, which show very pronounced features of the Ag 4*d* band even at very low Ag-content samples, see Fig. 3.2. Other experiments showed that the responsibility for this behavior of *a*-C:H/Ag samples lies on the pronounced surface clusters coalescence into bigger agglomerates. The Fermi edge evolution from monocrystalline metal reference samples to low metal-content *a*-C:H (Fig. 3.3) showed both decrease in the density of states near the Fermi level and its shift to the higher BEs, related to the cluster structure of metallic inclusions and to the same direction-shifts in metal core levels (Fig. 3.1).

Our further attention was focused on low metal-content *a*-C:H that is, typically below 10 at.%, and to the differences between grounded and biased samples. The reprint of the communication on these effects encountered in *a*-C:H/Au and published in the Applied Physics Letters (Vol. 80, 2002, p.2863) is given in Section 3.2.

Direct imaging techniques (Sections 3.2 and 3.3) reveal that even small amount of metal included in the *a*-C:H significantly changes the surface morphology and increases roughness. For all three nanocomposite materials, biased samples show similar surface morphology, characterized by relatively flat basis and isolated bump structures, of about 30 nm in diameter and up to 15 nm in height, see (Fig. 1 in Section 3.2 and Figs. 3.4-3.7). These structures are attributed to the altered morphology of *a*-C:H component of a nanocomposite, with metallic clusters concentrated on them. Grounded samples characterize low roughness in *a*-C:H/Au and increased in *a*-C:H/Ag and *a*-C:H/Cu. The increase of roughness in the latter two materials is explained by enhanced surface diffusion of metal atoms and clusters coalescence into bigger islands.

Complementary to direct imaging, GISAXS technique revealed more detailed insight in cluster dimensions and intercluster distance, in cases when it was applicable to our samples that is, not very rough ones. GISAXS patterns (Section 3.4, Figs. 3.9-3.11) showed isotropic cluster size and intercluster distance distribution in grounded *a*-C:H/Au and *a*-C:H/Cu samples. With grounded *a*-C:H/Ag sample, no spatial correlation could be revealed, probably again due to the surface agglomeration of Ag clusters. It is interesting that GISAXS, which was with less success applied to the grounded samples of *a*-C:H/Ag and *a*-C:H/Cu in comparison to *a*-C:H/Au, with biased samples showed inverted situation: *a*-C:H/Ag and *a*-C:H/Cu, contrary to *a*-C:H/Au, yielded usable GISAXS patterns that could be analyzed and at least cluster size revealed. These analysis showed that biased samples contain bigger clusters than grounded ones, and slightly flattened in the grow direction (Table 3.2).

The differences between grounded and biased samples were first detected by *in vacuo* XPS of *a*-C:H/Au in systematically lower, in average about 50%, Au content in the biased than in the grounded case. This decrease is followed by higher positive shift of the Au $4f_{7/2}$ core level binding energy in the biased case (Section 3.2 and

Paragraph 3.5.1). The similar situation was encountered in *a*-C:H/Ag samples, while *a*-C:H/Cu showed higher Cu content in the biased than in the grounded case and no difference in Cu $2p_{3/2}$ shifts from the reference BE (Fig. 3.12). Having in mind: (1) results of the direct imaging of the samples, particularly isolated bump structures in the biased ones (Fig. 1 in Section 3.2 and Figs. 3.4-3.7) and (2) GISAXS results, which revealed larger clusters and higher intercluster distance in biased than in grounded *a*-C:H/Ag and *a*-C:H/Cu (Section 3.4, Table 3.2), following conclusions may be drawn:

1. The decrease of the total metal content in biased *a*-C:H/Au and *a*-C:H/Ag samples most probably results from increased distance among surface clusters and their concentration on isolated bump structures;
2. The reason for the increased BE shift of Au $4f_{7/2}$ and Ag $3d_{5/2}$ core levels in the biased samples should be searched in cluster baldness at the sample surface;
3. The violation of both above conclusions in *a*-C:H/Cu, i.e. higher Cu content in the biased sample and equal shift of the Cu $2p_{3/2}$ core level in grounded and biased sample is probably due to high relative increase of copper cluster size upon biasing (see Table 3.2), which compensates the effect of their baldness at the surface;
4. The topmost clusters of grounded nanocomposite samples are, therefore, most probably covered with a layer of *a*-C:H. The thickness of this layer must be below escape depth of metal-originated photoelectrons, i.e. less than about 2 nm.

Upon biasing, the carbon C 1*s* core level in all samples is shifted towards lower binding energies, indicating increased sp^2/sp^3 coordinated carbon ratio in the *a*-C:H component. Our opinion is that Ar^+ ion bombardment of the substrate during the deposition process itself additionally reduces the content of isotropic sp^3 carbon bonds in favor of sp^2 hybridization. Therefore, to our list of conclusions, we would add the following one:

5. The negative shift of the C 1*s* core level in the biased samples is induced by increased sp^2/sp^3 coordinated carbon ratio due to the sample bombardment by Ar^+ ions during the deposition process. To our belief, the same effect is responsible for surface metallic clusters baldness in the biased samples.

These conclusions are supported by several following PES experiments, other than XPS of as-deposited samples. First of them was *in vacuo* UPS of as-deposited samples (Fig. 3.13). In the grounded samples, the He I spectra mostly reproduce the characteristic shape of *a*-C:H valence band, and only higher sensitivity He II UPS reveal the presence of metallic inclusions. Upon biasing, even when total measured metal content was lower than in the grounded case (*a*-C:H/Au and *a*-C:H/Ag), all

spectra clearly showed increased metallic features, evidencing on higher metal exposure at the surface.

XPS at off-normal take-off angle of escaping electrons (Paragraph 3.5.2) also confirmed our conclusions on the surface clusters coverage. Increasing the tilting angle of a sample, measured intensity ratio of a metal core level to appropriate C 1*s* showed in most grounded samples monotonous decrease, and regular and steady increase in the biased ones (Fig. 3.14). Based on a principle described in Paragraph 2.2.2 and Fig. 2.9, these results support our conclusion on the surface clusters coverage in grounded samples and their baldness in the biased ones. The higher metal-content grounded samples of *a*-C:H/Ag, however, did not show the expected decrease in the intensity ratio, see Fig. 3.14, and that was the first indication that the effect of coverage may be a particularity of small clusters only, i.e. low-metal content grounded samples.

This suspicious is confirmed in the next test experiment that we have undertaken, by subsequent *in situ* low-energy Ar^+ ion etching and PES analysis of a sample. The same metal to carbon core level intensity ratio curves were measured against the sputtering time (Fig. 3.15). In the grounded samples, at the beginning of the sputtering, an increase in the intensity ratio is observed, related to the thinning of the top *a*-C:H layer. In most cases, after some time of sputtering, the maximum is reached related to the total removal of the cover layer, and from that point onwards, Ar^+ ion etching erodes the metallic clusters as well. In biased samples, a monotonous decrease of intensity ratio curves was observed throughout the experiment and is clearly related to the bald surface clusters that are sputtered together with the *a*-C:H matrix. The grounded samples intensity ratio curves showed one more important regularity: in higher metal-content samples the maximum is reached after *shorter* time, i.e. these samples need less time to be fully uncovered. As a special case, *a*-C:H/Ag 32.3 at.% did not show any increase in the intensity ratio curve, but monotonous decrease throughout the measurement (see Fig. 3.15). This result enables us to add one more conclusion to our list:

6. The coverage of the topmost metallic clusters of grounded samples with *a*-C:H is an effect that is characteristics of small clusters in the host matrix, i.e. low metal-content samples. With higher metal contents, there is no observable difference between grounded and biased samples regarding surface clusters coverage.

The decrease of the position of maximum in the intensity ratio curves in Fig. 3.15, i.e. the “uncovering time” with increased metal content in a sample is a good indication that the amount of the “coverage” material is constant for all samples. The smaller clusters are therefore coated with thicker *a*-C:H layer than the bigger ones. This enables one to speculate about the possible origin of “coverage effect”, which we will repeat at the end of this text.

Apart from the core level intensity ratio curves, the evolution of our samples with *in situ* Ar^+ ion etching is described in XPS and UPS spectra recorded at each point of the sputtering time scale (several selected XPS and UPS spectra are shown in Figs 3.16-3.21). Metal core levels in these figures remained either unchanged or are slightly shifted towards higher binding energies. In the grounded samples, this is related to the thinning of the cover layer, and in the biased ones to the decrease of the cluster size by Ar^+ ion sputtering. The only exception is, again *a*-C:H/Ag, which in the first part of the etching process (increasing part in the intensity ratio curve in Fig. 3.15) shows slight shift to the lower binding energies, see Fig. 3.18. This may be explained by enhanced surface clusters coalescence by removal of the "protective" *a*-C:H layer. Carbon C 1*s* core level in all samples shows shift with sputtering time towards lower binding energies, which is related to the further sp^2-coordinated carbon favoring by the *in situ* Ar^+ ion bombardment.

The UPS spectra evolution (Figs 3.17, 3.19, and 3.21) generally follows the trend described by core level intensity ratio curves (Fig. 3.15). That is, in grounded samples, the metal features in valence band spectra rise to the point of total removal of the cover layer, and decrease further to the end of the sputtering experiment. Biased samples, on the other hand, show continuous decrease of the metal features. In both grounded and biased valence band spectra, the development of the carbon π-states is observed throughout the experiment, evidencing on the increase of sp^2-coordinated carbon content with sputtering time. This is additionally emphasized by the evolution of the states in the vicinity of the Fermi edge, Fig. 3.22. The peculiarity of the valence band spectra is the rise of the Ar 3*p* kink from incorporated argon in the sample after longer (90 – 300 s) sputtering time.

Pointed out several times, the Ag surface clusters coalescence is confirmed in experiment in which we compared XPS and UPS spectra of as-deposited samples, after 20 hours residence in the ultra-high vacuum (UHV) conditions and after additional 20 hours in the air (Figs 3.24-3.29). Generally, all as-deposited spectra and after 20 hours in the UHV were almost identical. The only exception is biased *a*-C:H/Au valence band spectra (Fig. 3.25), which showed some of carbon sp^3 bonds (mostly destroyed in deposition under substrate bias voltage, see Fig. 3.12), restored in the UHV. After exposure to the air, in all samples carbon C 1*s* core level is shifted towards lower binding energies. The most interesting differences after residence in the air show metal core levels. The Au $4f_{7/2}$ core level remained practically identical to the one measured in the UHV (Fig. 3.24), revealing that air conditions do not affect Au clusters, and that their size and arrangement remain fully determined by the deposition process. That is not the case, however, with Ag clusters. The Ag $3d_{5/2}$ core levels of both grounded and biased *a*-C:H/Ag samples shift towards lower binding energies (Fig. 3.26). From the differences in UHV- and air-residence binding energy positions of the Ag $3d_{5/2}$, it is estimated that the increase factor of cluster volume in grounded samples is about 170, and the one of biased samples clusters – about 12. In these rough figures one may find the cause of the specific behavior of the *a*-C:H/Ag sample that we encountered in several occasions and assigned to the Ag

surface clusters coalescence: roughness revealed by AFM, lack of correlation in the GISAXS patterns, pronounced Ag 4d features even in low metal content valence band spectra, and negative shift of the Ag $3d_{5/2}$ in the Ar^+ ion *in situ* in-depth profiling. The last of our nanocomposites subjected to UHV- and air-dwell comparison was *a*-C:H/Cu. Copper, however, oxidizes in the air (Fig. 3.28), but nevertheless it provided in this experiment one of most elegant evidences on the surface clusters coverage. The deconvolution procedure applied to copper- and CuO-originated Cu $2p_{3/2}$ (Fig 3.30) revealed that relative content of oxidized copper is higher on the surface of biased sample (with bald surface clusters), than on the grounded one (where surface clusters are covered by *a*-C:H).

The last in the series of experiments aimed to check our conclusions on the surface clusters coverage was based on the prospective sulfur binding to noble metal atoms. Our samples, together with appropriate monocrystalline reference samples, were covered with a layer of liquid thiophene (C_4H_4S) and, after evaporation, subjected again to the XPS analysis. The total amount of adsorbed sulfur was generally low, about 5 at.% or less. That results in noisy XPS spectra of the S 2*p* core levels region, in spite of increased measurement statistics. The S 2*p* spectra adsorbed on the reference samples were fitted with three S $2p_{1/2}$ – S $2p_{3/2}$ doublets assigned to S bonds to a noble metal, S in C_4H_4S, and to S–O bonds (Figs. 3.32-3.34). Intercomparison of our nanocomposite samples with reference ones showed that sulfur adsorbed on surfaces originates predominantly from C_4H_4S itself. However, in biased cases a higher relative contribution of the shoulder related to sulfur bonds to a noble metal is observed in spectra, evidencing on higher metal exposure at the biased samples surfaces. The exception of *a*-C:H/Cu is due to the oxidation of copper.

In conclusion, in several different PES experiments, by direct imaging of samples, and using GISAXS technique, we have revealed that MS/PACVD-obtained low noble metal-content amorphous hydrogenated carbon nanocomposites are characterized with topmost metallic clusters covered with a tiny layer of *a*-C:H when deposited on a grounded substrate, and bald surface clusters when substrate is biased with –150 V dc. Bearing in mind all results that we comprised in this work, we would like to propose a surface model that is schematically depicted in Fig. 4.1. Beside this main result, we encountered few other effects, like e.g. increased sp^2/sp^3 coordinated carbon ratio in the *a*-C:H matrix in the biased samples and surface clusters coalescence in *a*-C:H/Ag (and to some extent in *a*-C:H/Cu) nanocomposites.

By changing one parameter only – the substrate bias voltage in deposition of our grounded and biased “counterparts”, we have shown that surface clusters coverage effect has an origin in the plasma deposition process itself. We believe that one should look for its cause in the plasma afterglow, the state established in the ionized gas immediately after switching off the plasma power supply (see more detail in Paragraph 3.5.2). For some reason, carbon and hydrocarbon species arrive latest to the substrate, and create the cover layer of *a*-C:H in the grounded samples. With the applied substrate bias voltage, an afterglow Ar^+ ion striking the sample most probably preserves formation of this layer. To understand the processes in plasma that lead to

the formation of the cover layer of *a*-C:H, one should employ time- and spatially-resolved optical emission spectroscopy to study the distribution of plasma species in different regions of magnetron plasma discharge, particularly in the vicinity of the substrate.

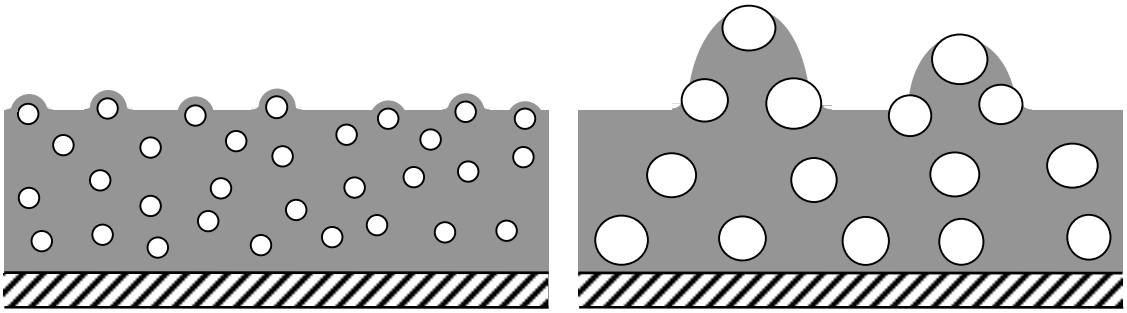

Fig. 4.1. Model of the surface region in low metal-content *a*-C:H nanocomposites deposited on grounded and biased substrate.

From the applicative point of view, we have described, in principle, the mechanism that may be employed to tailor the coverage of topmost metallic clusters embedded in the *a*-C:H matrix. Metal inclusions in the *a*-C:H showed to improve the wear resistance of the coatings, so one can also envisage the applications when the coverage of surface metal clusters with *a*-C:H would be useful. In tribology, these would be cases when incorporated metal reduces the lubricating properties, i.e. increases the friction coefficient. In biocompatible materials the same would be necessary when incorporated metals are toxic, like e.g. silver or copper. *Vice versa*, one may also envisage applications when topmost cluster baldness would be desirable, like e.g. with low-friction MoS_2 and WS_2 inclusions in *a*-C:H for tribological purposes. In addition, surface clusters exposure to the surrounding environment probably influences the optical and aging properties of solar selective coatings based on metal- or metal carbide-containing amorphous hydrogenated carbon nanocomposites.

References

[1] P. Koidl, P. Oelhafen, *Amorphous Hydrogenated Carbon Films* (Les Editions de Physique, Les Ulis, 1987).

[2] S. R. P. Silva, J. Robertson, W. I. Milne, and G. A. J. Amaratunga, *Amorphous Carbon: State of the Art* (World Scientific, Singapore, 1998).

[3] M. Chhowalla, C. W. Chen, B. Kleinsorge, J. Robertson, G. A. J. Amaratunga, and W. I. Milne, Mat. Res. Soc. Symp. Proc. **423** (1996) p. 299.

[4] A. Grill, Surf. Coat. Technol. **94–95** (1997) 507.

[5] A. Grill, IBM J. Res. Dev. **43** (1999) 147.

[6] A. Grill, Diam. Relat. Mater. **8** (1999) 428.

[7] C. Donnet, Surf. Coat. Technol. **100–101** (1998) 180.

[8] A. Gangopadhyay, Tribol. Lett. **5** (1998) 25.

[9] R. Hauert and U. Müller, Diam. Relat. Mater. **12** (2003) 171.

[10] H. S. Tran, M. M. Puc, C. W. Hewitt, D. B. Soll, S. W. Marra, V. A. Simonetti, J. H. Cilley, and A. J. Delrossi, J. Invest. Surg. **12** (1999) 133.

[11] I. de Scheerder, M. Szilard, H. Yanming, X. B. Ping, E. Verbeken, D. Neerinck, E. Demeyere, W. Coppens, F. van de Werf, J. Invasive Cardiol. **12** (2000) 389.

[12] H. Dimigen and H. Hubsch, Philips Tech. Rev. **41** (1983) 186.

[13] H. Dimigen, H. Hubsch, and R. Memming, Appl. Phys. Lett. **50** (1987) 1056.

[14] C.-P. Klages and R. Memming, Mater. Sci. Forum **52–53** (1989) 609.

[15] M. Fryda, K. Taube, and C.-P. Klages, Vacuum **41** (1990) 1291.

[16] H. Dimigen and C.-P. Klages, Surf. Coat. Technol. **49** (1991) 543.

[17] M. Wang, K. Schmidt, K. Reichelt, H. Dimigen, and H. Hubsch, J. Mater. Res. **7** (1992) 667.

[18] M. Fryda, C. Bennorf, C.-P. Klages, and K. Taube, Diam. Relat. Mater. **1** (1992) 558.

[19] M. Grischke, K. Bewilogua, H. Dimigen, Mater. Manuf. Process. **8** (1993) 407.

[20] D. Klaffke, Diamond Films Technol. **3** (1994) 149.

[21] R. Hauert, R. Gampp, U. Müller, A. Schroeder, J. Blum, J. Mayer, F. Birchler, and E. Wintermantel, Abstr. Pap. Am. Chem. S. **213** (1997) 395-POLY Part 2.

[22] R. Hauert, U. Müller, G. Francz, F. Birchler, A. Schroeder, J. Mayer, and E. Wintermantel, Thin Solid Films **308** (1997) 191.

[23] G. Francz, A. Schroeder, and R. Hauert. Surf. Interface Anal. **28** (1999) 3.

[24] R. Hauert, L. Knoblauch-Meyer, G. Francz, A. Schroeder, and E. Wintermantel, Surf. Coat. Technol. **121** (1999) 291.

[25] A. Schroeder, G. Francz, A. Bruinink, R. Hauert, J. Mayer and E. Wintermantel, Biomaterials **21** (2000) 449.

[26] R. Gampp, *Deposition und Charakterisierung von Metalhaltigen, Amorphen Kohlenwasserstoffilmen zur Anwendung in Sonnenkollektoren* (VDI, Düsseldorf, 1996).

[27] R. Joerger, R. Gampp, A. Heinzel, W. Graf, M. Köhl, P. Gantenbein, and P. Oelhafen, Sol. Energy Mater. Sol. Cells **54** (1998) 351.
[28] R. Gampp, P. Oelhafen, P. Gantenbein, S. Brunold, and U. Frei, Sol. Energy Mater. Sol. Cells **54** (1998) 369.
[29] P. Gantenbein, S. Brunold, U. Frei, J. Geng, A. Schüler, and P. Oellhafen, Carbon **37** (1999) 843.
[30] A. Schüler, J. Geng, P. Oelhafen, S. Brunold, and U. Frei, Sol. Energy Mater. Sol. Cells **60** (2000) 295.
[31] A. Schüler, C. Ellenberger, P. Oelhafen, C. Haug, and R. Brenn, J. Appl. Phys. **87** (2000) 4285.
[32] A. Schüler, I. R. Videnović, P. Oelhafen, and S. Brunold, Sol. Energy Mater. Sol. Cells **69** (2001) 271.
[33] K. I. Schiffmann, M. Fryda, G. Goerigk, R. Lauer, and P. Hinze, Ultramicroscopy **66** (1996) 183.
[34] K. I. Schiffmann, M. Fryda, G. Goerigk, R. Lauer, P. Hinze, and A. Bulack, Thin Solid Films 347 (1999) 60.
[35] D. Babonneau, I. R. Videnović, M. G. Garnier, and P. Oelhafen, Phys. Rev. B **63** (2001) 195401.
[36] N. Pinçon, B. Palpant, D. Prot, E. Charron, and S. Debrus, Eur. Phys. J. D **19** (2002) 395.
[37] S. Deki, H. Nabika, K. Akamatsu, M. Mizuhata, A. Kajinami, S. Tomita, M. Fujii, S. Hayashi, Thin Solid Films **408** (2002) 59.
[38] M. Haruta, Catal. Today **36** (1997) 153.
[39] T. Akita, K. Tanaka, S. Tsubota, and M. Haruta, J. Electron Microsc. **49** (2000) 657.
[40] H.-G. Boyen, G. Kästle, F. Weigl, B. Koslowski, C. Dietrich, P. Ziemann, J. P. Spatz, S. Riethmüller, C. Hartmann, M. Möller, G. Schmid, M. G. Garnier, and P. Oelhafen, Science **297** (2002) 1533.
[41] H.-G. Boyen, G. Kästle, F. Weigl, P. Ziemann, G. Schmid, M. G. Garnier, and P. Oelhafen, Phys. Rev. Lett. **87** (2001) 276401.
[42] H.-G. Boyen, Th. Herzog, G. Kästle, F. Weigl, P. Ziemann, J. P. Spatz, M. Möller, R. Wahrenberg, M. G. Garnier, and P. Oelhafen, Phys. Rev. B **65** (2002) 075412.
[43] H. Biederman, Z. Chmel, A. Fejfar, M. Mišina, and J. Pejšička, Vacuum **40** (1990) 377.
[44] H. Biederman, I. Čermák, A. Fejfar, and J. Pejšička, Int. J. Electron. **76** (1994) 937.
[45] M. Iwaki, K. Yabe, A. Fukuda, H. Watanabe, A. Itoh, and M. Takeda, Nucl. Instrum. Meth. B **80–81** (1993) 1080.
[46] D. C. Jacobson, D. E. Luzzi, T. F. Heinz, and M. Iwaki, in: *Beam-Solid Interactions for Materials Synthesis and Characterization*, (Materials Research Society, Pittsburgh, 1995) p. 369.
[47] A. Naudon and D. Babonneau, Z. Metallkd. **88** (1997) 596.

[48] D. Babonneau, T. Cabioc'h, A. Naudon, J. C. Girar, and M. F. Denanot, Surf. Sci. **409** (1998) 358.
[49] D. Babonneau, A. Naudon, D. Thaudière, and S. Lequien, J. Appl. Cryst. **32** (1999) 226.
[50] D. Babonneau, A. Suárez-García, J. Gonzalo, I. R. Videnović, M. G. Garnier, P. Oelhafen, M. Jaouen, and A. Naudon, Mat. Res. Soc. Symp. Proc. **678** (2001) EE5.6.1.
[51] S. Camelio, D. Babonneau, T. Girardeau, J. Toudert, F. Lignou, M.-F. Denanot, N. Maitre, A. Barranco, and P. Guerin, Appl. Optics, **42** (2003) 674.
[52] J.-P. Barnes, A. K. Petford-Long, R. C. Doole, R. Serna, J. Gonzalo, A. Suárez-García, C. N. Afonso, and D. Hole, Nanotechnology **13** (2002) 465.
[53] T. de los Arcos, P. Oelhafen, U. Aebi, A. Hefti, M. Düggelin, D. Mathys, and R. Guggenheim, Vacuum **67** (2002) 463.
[54] H. Hofass, H. Binder, T. Klumpp, and E. Recknagel, Diam. Relat. Mater. **3** (1994) 137.
[55] V. I. Ivanov-Omskiĭ, M. I. Abaev, and S. G. Yastrebov, Tech. Phys. Lett.+ **20** (1994) 917.
[56] B. Oral, R. Hauert, U. Müller, and K.-H. Ernst, Diam. Relat. Mater. **4** (1995) 482.
[57] S. J. Dikshit, P. Lele, S. B. Ogale, S. T. Kshirsagar, J. Mater. Res. **11** (1996) 2236.
[58] V. I. Ivanov-Omskiĭ, V. I. Siklitskiĭ, and S. G. Yastrebov, Phys. Solid State+ **40** (1998) 524.
[59] V. I. Ivanov-Omskiĭ, T. K. Zvonareva, and G. S. Frolova, Phys. Solid State+ **41** (1999) 286.
[60] V. I. Ivanov-Omskiĭ and S. G. Yastrebov, Diam. Relat. Mater. **8** (1999) 554.
[61] V. I. Ivanov-Omskiĭ and S. G. Yastrebov, Phys. Solid State+ **41** (1999) 1711.
[62] T. N. Vasilevskaya, N. S. Andreev, I. A. Drozdova, V. N. Filipovich, S. G. Yastrebov, and T. K. Zvonareva, Phys. Solid State+ **41** (1999) 1918.
[63] V. I. Siklitskiĭ, S. G. Yastrebov, and A. B. Lodygin, Chaos Soliton. Fract. **10** (1999) 2067
[64] L. V. Lutsev, S. V. Yakovlev, and V. I. Siklitskiĭ, Phys. Solid State+ **42** (2000) 1105.
[65] Q. Wei, R. J. Narayan, J. Narayan, J. Sankar, and A. K. Sharma, Mater. Sci. Eng. B - Solid **53B** (1998) 262.
[66] Q. Wei, A. K. Sharma, J. Sankar, and J. Narayan, Compos. Part B – Eng. 30B (1999) 675.
[67] Q. Wei, R. J. Narayan, A. K. Sharma, J. Sankar, and J. Narayan, J. Vac. Sci. Technol. A **17** (1999) 3406.
[68] R. F. Bunshah, *Deposition Technologies for Films and Coatings* (Noyes Publication, Park Ridge, 1982).

[69] J. Bretagne, 16th ESCAMPIG / 5th ICRP Joint Conference, July 14 – 18, 2002, Grenoble, France, *Conference Proceedings*, Vol. 1, p. 11.
[70] J. Laimer, M. Fink, and H. Störi, 16th ESCAMPIG / 5th ICRP Joint Conference, July 14 – 18, 2002, Grenoble, France, *Conference Proceedings*, Vol. 1, p. 267.
[71] B. Chapman, *Glow Discharge Processes* (Wiley, New York, 1980).
[72] J. A. Thornton, in: *Deposition Technologies for Films and Coatings*, Ed. R. F. Bunshah (Noyes Publication, Park Ridge, 1982) 178.
[73] N. Matsunami, Y. Yamamura, Y. Itikawa, N. Itoh, Y. Kazumata, S. Miyagawa, K. Morita, R. Shimizu, and H. Tawara, Atom. Data Nucl. Data **31** (1984) 1.
[74] I. R. Videnović, T. de los Arcos, and P. Oelhafen, 20th SPIG, September 4-8, 2000, Zlatibor, Yugoslavia, *Contributed Papers*, p. 227.
[75] H. Hertz, Wied. Ann. **31** (1887) 983.
[76] J. J. Thompson, Phil. Mag. **48** (1899) 547.
[77] P. Lenard, Wien. Ber. **108** (1899) 649.
[78] P. Lenard, Ann. Physik **2** (1900) 359.
[79] P. Lenard, Ann. Physik **8** (1902) 149.
[80] A. Einstein, Ann. Physik **17** (1905) 132.
[81] S. Hüfner, *Photoelectron Spectroscopy* (Springer-Verlag, Berlin, 1995).
[82] M. Cardona and L. Ley, *Photoemission in Solids I* (Springer-Verlag, Berlin, 1978).
[83] M. Cardona and L. Ley, *Photoemission in Solids II* (Springer-Verlag, Berlin, 1979).
[84] G. Ertl, J. Küppers, *Low Energy Electrons and Surface Chemistry* (VCH, Weinheim, 1985).
[85] K. Siegbahn, C. Nodrling, A. Fahlman, R. Nordberg, K. Hamrin, J. Hedman, G. Johansson, T. Bergmark, S. E. Karlsson, I. Lindgren, and B. Lindberg, *ESCA – Atomic, Molecular, and Solid State Sructure Studied by Means of Electron Spectroscopy* (Almquist and Wicksell, Uppsala, 1967).
[86] K. Siegbahn, C. Nodrling, G. Johansson, J. Hedman, P. F. Heden, K. Hamrin, U. Gelius, T. Bergmark, L. O. Werme, R. Manne, and Y. Baer, *ESCA Applied to Free Molecules*, (North Holland, Amsterdam, 1969).
[87] K. Larson, C. Nodrling, K. Siegbahn, and E. Stenhagen, Acta Chem. Scand. **20** (1966) 2880.
[88] A. Zangwill, *Physics at Surfaces* (Cambridge University Press, 1988).
[89] A. Schüler, R. Gampp, and P. Oelhafen, Phys. Rev. B **60** (1999) 16164.
[90] D. A. Shirley, Phys. Rev. B **5** (1972) 4709.
[91] J. H. Scofield, J. Electron Spectrosc. Relat. Phenom. **8** (1976) 129.
[92] G. Binnig, C. F. Quate, and Ch. Gerber, Phys. Rev. Lett. **56** (1986) 930.
[93] J. R. Levine, J. B. Cohen, Y. W. Chung, and P. Georgopoulos, J. Appl. Crystallogr. **22** (1989) 528.
[94] A. Naudon and D. Thiaudière, J. Appl. Crystallogr. **30** (1997) 822.
[95] M. Schmidbauer, Th. Wiebach, H. Raidt, M. Hanke, R. Köhler, and H. Wawra, Phys. Rev. B **58** (1998) 10523.

[96] A. Guinier and G. Fournet, *Small-Angle Scattering of X-Rays* (Wiley, New York, 1955).
[97] J. F. Moulder, W. F. Stickle, P. E. Sobol, K. D. Bomben, *Handbook of X-ray Photoelectron Spectroscopy* (Perkin-Elmer Corporation, Eden Prairie, 1992).
[98] D. R. Lide, *CRC Handbook of Chemistry and Physics* (CRC Press, Boca Raton, 1997).
[99] C. Benndorf, E. Boettger, M. Fryda, H. G. Haubold, C.-P. Klages, and H. Köberle, Synth. Metals **41-43** (1991) 4055.
[100] J. Robertson, Adv. Phys. **35** (1986) 317.
[101] J. Robertson, Phys. Rev. Lett. **68** (1992) 220.
[102] J. Díaz, G. Paolicelli, S. Ferrer, and F. Comin, Phys. Rev. B **54** (1996) 8064.
[103] S. Hirono, S. Umemura, M. Tomita, and R. Kaneko, Appl. Phys. Lett. **80** (2002) 425.
[104] Y. Mizokawa, T. Miyasato, S. Nakamura, K. M. Geib, and C. W. Wilmsen, J. Vac. Sci. Technol. A **5** (1987) 2809.
[105] J. C. Lascovich, R. Giorgi, and S. Scaglione, Appl. Surf. Sci. **47** (1991) 17.
[106] J. C. Lascovich and S. Scaglione, Appl. Surf. Sci. **78** (1994) 17.
[107] P. Mérel, M. Tabbal, M. Chaker, S. Moisa, and J. Margot, Appl. Surf. Sci. **136** (1998) 105.
[108] S. Tugeron and R. W. Paytner, Thin Solid Films **394** (2001) 44.
[109] W. Lu and K. Komvopoulos, Appl. Phys. Lett. **82** (2003) 2437.
[110] P. Oelhafen and D. Ugolini, in: *Amorphous Hydrogenated Carbon Films*, Eds. P. Koidl and P. Oelhafen (Les Editions de Physique, Les Ulis, 1987) p. 267.
[111] S. Schelz, T. Richmond, P. Kania, P. Oelhafen, and H.-J. Güntherodt, Surf. Sci. **359** (1996) 227.
[112] P. Reinke, G. Francz, P. Oelhafen, and J. Ulmann, Phys. Rev. B **54** (1996) 7067.
[113] P. Reinke and P. Oelhafen, J. Appl. Phys. **81** (1997) 2396.
[114] B. Shi, W. J. Meng, L. E. Rehn, and P. M. Baldo, Appl. Phys. Lett. **81** (2002) 352.
[115] M. Gioti, S. Logothetidis, and C. Charitidis, Appl. Phys. Lett. **73** (1998) 184.
[116] N. A. Hastas, C. A. Dimitriadis, D. H. Tassis, Y. Panayiotatos, and S. Logothetidis, Appl. Phys. Lett. **79** (2001) 3269.
[117] J.-J. Yeh and I. Lindau, At. Data Nucl. Data Tables **32** (1985) 1.
[118] T. de los Arcos, P. Oelhafen, U. Aebi, A. Hefti, M. Düggelin, D. Mathys, and R. Guggenheim, Vacuum **67** (2002) 463.
[119] D. Babonneau, A. Naudon, D. Thiaudière, and S. Lequien, J. Appl. Cryst. **32** (1999) 226.
[120] J.-P. Barnes, A. K. Petfored-Long, R. C. Doole, R. Serna, J. Gonzalo, A. Suárez-García, C. N. Afonso, and D. Hole, Nanotechnol. **13** (2002) 465.
[121] A. Thran, T. Strunskus, V. Zaporojtchenko, and F. Faupel, Appl. Phys. Lett. **81** (2002) 244.
[122] F. S. Ohuchi and S. Freilich, J. Vac. Sci. Technol. A **4** (1984) 1039.

[123] F. S. Ohuchi and S. Freilich, J. Vac. Sci. Technol. A **6** (1988) 1004.
[124] M. Du, R. L. Opila, V. M. Donnnelly, J. Sapjeta, and T. Boone, J. Appl. Phys. **85** (1999) 1496.
[125] J. H. Das and J. E. Morris, IEEE Trans. Compon., Packag. Manuf. Technol., Part B **17** (1994) 620.
[126] D. Popovici, K. Piyakis, M. Meunier, and E. Sacher, J. Appl. Phys. **83** (1998) 108.
[127] M. Keine, T. Strunskus, R. Peter, and F. Faupel, Adv. Mater. **10** (1998) 1357.
[128] N. Marin, Y. Serruys, and P. Calmon, Nucl. Instrum. Methods Phys. Res. B **108** (1996) 179.
[129] D. R. Peale, B. H. Cooper, J. Vac. Sci. Technol. A **10** (1992) 2210.
[130] B. H. Cooper, D. R. Peale, J. G. McLean, R. Phillips, and E. Chason, Mat. Res. Soc. Symp. Proc. **280** (1993) 37.
[131] E. Byon, T. W. H. Oates, and A. Anders, Appl. Phys. Lett. **82** (2003) 1634.
[132] A. R. Layson and P. A. Thiel, Surf. Sci. **472** (2001) L151.
[133] A. R. Layson, J. W. Evans, and P. A. Thiel, Phys. Rev. B **65** (2002) 193409.
[134] S. Doniach and M. Šunjić, J. Phys. C **3** (1970) 285.
[135] Y. Akinaga, T. Nakajima, and K. Hirao, J. Chem. Phys. **114** (2001) 8555.
[136] P. Väterlein, M. Schmelzer, J. Taborski, T. Krause, F. Viczian, M. Bäßler, R. Fink, E. Umbach, and W. Wurth, Surf. Sci. **452** (2000) 20.
[137] D. Krüger, H. Fuchs, R. Rousseau, D. Marx, and M. Parrinello, J. Chem. Phys. **115** (2001) 4776.
[138] K. Heister, M. Zharnikov, M. Grunze, L. S. O. Johansson, and A. Ulman, Langmuir **17** (2001) 8.
[139] J. A. Rodriguez, J. Hrbek, J. Dvorak, T. Jirsak, and A. Maiti, Chem. Phys. Lett. **336** (2001) 377.

List of publications (course of Ph.D.)

ARTICLES IN INTERNATIONAL JOURNALS

Ivan R. Videnović, Verena Thommen, Peter Oelhafen, Daniel Mathys, Marcel Düggelin, and Richard Guggenheim,
Influence of substrate bias voltage on surface morphology and nanocluster arrangement of gold containing amorphous hydrogenated carbon,
Appl. Phys. Lett. **80** (2002) 2863.

D. Babonneau, I. R. Videnović, M. G. Garnier, and P. Oelhafen,
Morphology and size distribution of gold nanoclusters in a-C:H films studied by grazing incidence small angle x-ray scattering,
Phys. Rev. B **63** (2001) 195401.

A. Schüler, I. R. Videnović, P. Oelhafen, S. Brunold, P. Gantenbein, and U. Frei,
Titanium containing amorphous hydrogenated silicon carbon films (a-Si:C:H/Ti) for durable solar absorber coatings,
Sol. Energy Mater. and Sol. Cells **69** (2001) 271.

INTERNATIONAL CONFERENCES

I. R. Videnović, T. de los Arcos, and P. Oelhafen,
XPS study of target poisoning during the plasma assisted deposition of a-C:H/Au thin films,
20th Summer School and International Symposium on the Physics of Ionized Gases (SPIG), September 4 – 8, 2000, Zlatibor, Contributed papers, p. 227.

D. Babonneau, A. Suárez-García, J. Gonzalo, I. R. Videnović, M. G. Garnier, P. Oelhafen, M. Jaouen, and A. Naudon,
Grazing incidence small-angle x-ray scattering applied to the characterization of nanocomposite thin films,
Materials Research Society 2001 Spring Meeting, San Francisco, April 16 – 20, Abstracts, p. 470.

D. Babonneau, A. Suárez-García, J. Gonzalo, I. R. Videnović, M. G. Garnier, P. Oelhafen, M. Jaouen, and A. Naudon,
Grazing incidence small-angle x-ray scattering applied to the characterization of nanocomposite thin films,
Mat. Res. Soc. Symp. Proc. **678** (2001) EE5.6.1.

Ivan R. Videnović, Verena Thommen, Daniel Mathys, Marcel Düggelin, Richard Guggenheim, Peter Oelhafen, David Babonneau, and André Naudon,
Cluster arrangement on the surface of gold containing amorphous hydrogenated carbon (a-C:H/Au) nanocomposites,
Materials Research Society 2002 Spring Meeting, April 1 – 5, 2002, San Francisco, Abstracts, p. 356.

I. R. Videnović, V. Thommen, and P. Oelhafen,
Surface arrangement of gold nanoclusters embedded in amorphous hydrogenated carbon by reactive magnetron sputtering,
16th Europhysics Conference on Atomic & Molecular Physics (ESCAMPIG) and 5th International Conference on Reactive Plasmas (ICRP), July 14 – 18, 2002, Grenoble, Proceedings II, p. 207.

Invited lecture: I. R. Videnović and P. Oelhafen,
Thin film deposition by magnetron plasmas: surface characterization of gold nanocluster-containing amorphous hydrogenated carbon,
4th Yugoslav-Belarussian Symposium on Physics and Diagnostics of Laboratory & Astrophysical Plasma, Belgrade, August 23 – 24, 2002, Abstracts of invited lectures and posters, p. 7.

I. R. Videnović and P. Oelhafen,
Surface morphology of magnetron-sputtered a-C:H/Au nanocomposites: a photoelectron spectroscopy study,
21st Summer School and International Symposium on the Physics of Ionized Gases (SPIG), August 26 – 30, 2002, Sokobanja, Contributed papers, p. 222.

I. R. Videnović and P. Oelhafen,
Photoelectron spectroscopy study of copper-containing a-C:H thin films. Surface arrangement of Cu nanoclusters,
Fifth General Conference of Balkan Physical Union, August 25 – 29, 2003, Vrnjačka Banja (accepted).

NATIONAL CONFERENCES

I. R. Videnović, D. Babonneau, D. Mathys, V. Thommen, and P. Oelhafen,
Characterization of noble metals-containing amorphous hydrogenated carbon thin films,
Swiss Physical Society Annual Meeting, May 2 – 3, 2001, Dübendorf, Bull. SPG/SSP **18** (2001) p. 75.

Ivan R. Videnović and Peter Oelhafen,
Photoelectron spectroscopy study of the surface structure and morphology of gold nanocluster containing amorphous hydrogenated carbon (a-C:H/Au),
Swiss Physical Society Annual Meeting, February 28 – March 1, 2002, Lausanne, Bull. SPG/SSP **19** (2002) p. 33.

I. R. Videnović, D. Babonneau, V. Thommen, D. Mathys, and P. Oelhafen,
Surface arrangement of silver nanocluster-containing amorphous hydrogenated carbon (a-C:H/Ag)
Swiss Physical Society Annual Meeting, March 20 – 21, 2003, Basel, Bull. SPG/SSP **20** (2003) p. 44.

ARTICLES IN PREPARATION

I. R. Videnović and P. Oelhafen,
Surface structure and morphology of gold nanoclusters-containing amorphous hydrogenated carbon (a-C:H/Au) studied by photoelectron spectroscopy.

I. R. Videnović and P. Oelhafen,
Photoelectron spectroscopy study of amorphous hydrogenated carbon doped with transition metals of 1B group.

I. R. Videnović, D. Babonneau, V. Thommen, D. Mathys, and P. Oelhafen,
Surface arrangement of silver nanoclusters-containing amorphous hydrogenated carbon (a-C:H/Ag).

I. R. Videnović, D. Babonneau, V. Thommen, D. Mathys, and P. Oelhafen,
Photoelectron spectroscopy study of copper-containing a-C:H thin films. Surface arrangement of Cu nanoclusters.

I. R. Videnović and P. Oelhafen,
Air-induced structural changes of magnetron-sputtered nanocomposite noble metal containing amorphous hydrogenated carbon thin films.

List of publications (other)

SCIENTIFIC BOOK – MONOGRAPH

Ivan R. Videnović,
Cathode dark space of a glow gas discharge (in Serbian),
Andrejević Foundation, Belgrade (1998).

ARTICLES IN INTERNATIONAL JOURNALS

I. R. Videnović, N. Konjević, and M. M. Kuraica,
Spectroscopic investigations of a cathode fall region of the Grimm-type glow discharge,
Spectrochim. Acta B 51 (1996) 1707.

M. M. Kuraica, N. Konjević, and I. R. Videnović,
Spectroscopic study of the cathode fall region of Grimm-type glow discharge in helium,
Spectrochim. Acta B 52 (1997) 745.

N. Konjević, I. R. Videnović, and M. M. Kuraica,
Emission spectroscopy of the cathode fall region of an analytical glow discharge,
J. Phys. IV France 7, C4 (1997) 247.

ARTICLES IN NATIONAL JOURNALS

N. Konjević, M. M. Kuraica, and I. R. Videnović,
Spectroscopic studies of an analytical glow discharge,
Scientific Review 24 (1997) 15.

INTERNATIONAL CONFERENCES

I. Videnović, M. Kuraica, A. Brablec, and N. Konjević,
Gas temperature in a microwave boosted plane cathode glow discharge,
11th European Sectional Conference on the Atomic and Molecular Physics of Ionized Gases (ESCAMPIG), St. Petersburg, August 25 – 28, 1992, Contributed papers, p. 380.

M. Kuraica, I. Videnović, and N. Konjević,
Electric field measurement in the cathode fall region of the plane cathode abnormal glow discharge,
17th Summer School and International Symposium on the Physics of Ionized Gases (SPIG), August 29 - September 1, Belgrade, 1994, Contributed papers, p. 216.

Invited lecture: N. Konjević, M. M. Kuraica, and I. R. Videnović,
Spectroscopic studies of an analytical glow discharge,
First Belarussian-Yugoslavian Symposium on Physics and Diagnostics of Laboratory & Astrophysical Plasma (PDP-I), July 1 – 3, 1996, Minsk, Proceedings, Publ. Obs. Astron. Belgrade 53 (1996) p. 23.

I. R. Videnović, N. Konjević, and M. M. Kuraica,
Temperatures of excited hydrogen atoms in the abnormal glow discharge,
ibid. p. 85.

I. R. Videnović, M. M. Kuraica, and N. Konjević,
Stark profiles of H_β line in the cathode fall region of an abnormal glow discharge,
ibid. p. 89.

I. R. Videnović, N. Konjević, and M. M. Kuraica,
On the linear Stark spectroscopy of the cathode fall region of abnormal glow discharge in hydrogen,
18th Summer School and International Symposium on the Physics of Ionized Gases (SPIG), September 2 – 6, 1996, Kotor, Contributed papers, p. 375.

I. R. Videnović, N. Konjević, and M. M. Kuraica,
Experimental testing of the cathode fall region theories,
ibid, p. 379.

M. M. Kuraica, N. Konjević, and I. R. Videnović,
Elelctric field measurements in the cathode fall region of abnormal glow discharge in helium,
ibid. p. 383.

N. M. Šišović, M. M. Kuraica, I. R. Videnović, V. I. Miljević, and N. Konjević,
Hydrogen Balmer line shapes in coaxial diode glow discharge,
ibid. p. 302.

I. R. Videnović, M. M. Kuraica, and N. Konjević,
On the hydrogen Balmer H_β line shapes in an abnormal glow discharge operating in helium–hydrogen mixture,
23rd International Conference on Phenomena in Ionized Gases (ICPIG), July 17 – 22, 1997, Toulouse, Contributed papers, Vol. IV p. 146.

I. R. Videnović, N. Konjević, and M. M. Kuraica
Diagnostics of the glow discharge cathode region by the atomic emission spectroscopy,
Week of Doctoral Students, WDS 98, June 9 – 12, 1998, Prague, Proceedings of contributed papers, Part II, p. 317.

I. R. Videnović and M. M. Platiša,
The influence of the fine structure to the Stark splitting of the hydrogen Balmer H_γ line in an external electric field,
19th Summer School and International Symposium on the Physics of Ionized Gases (SPIG), August 31 – September 4, 1998, Zlatibor, Contributed papers, p. 341.

I. R. Videnović and M. M. Platiša,
The influence of the fine structure to the hydrogen Balmer line shapes in the conditions typical for the analytical glow discharge cathode fall region,
2nd Yugoslav-Belarussian Symposium on Physics and Diagnostics of Laboratory & Astrophysical Plasma, September 5 – 6, 1998, Zlatbor, Proceedings, Publ. Obs. Astron. Belgrade 61 (1998) p. 175.

V.M.Astashynski, S.I.Ananin, V.V.Askerko, V.B.Avramenko, E.A.Kostyukevich, A.M.Kuzmitski, V.V.Uglov, V.M.Anishchik, V.V.Astashynski, N.T.Kvasov, A.L.Danilyuk, J.Purić, M.M.Kuraica, I.Dojčinović, and I.R.Videnović,
Compression plasma flows action on monocrystalline silicon surface,
29th EPS Conference on Plasma Physics and Controlled Fusion, June 17 – 21, 2002, Montreux, ECA Vol 26B, P-2.027.

S.I.Ananin, V.M.Astashynski, V.S.Burakov, E.A.Kostyukevich, A.M.Kuzmitski, N.V.Tarasenko, I.Dojčinović, M.M.Kuraica, J.Purić, and I.R.Videnović,
Quasi-stationary high-current plasma accelerator as plasma injector for fusion devices,
29th EPS Conference on Plasma Physics and Controlled Fusion, June 17 – 21, 2002, Montreux, ECA Vol 26B, P-5.049 (2002).

V.M.Astashynski, S.I.Ananin, V.V.Askerko, V.B.Avramenko, E.A.Kostyukevich, A.M.Kuzmitski, V.V.Uglov, V.M.Anishchik, V.V.Astashynski, N.T.Kvasov, A.L.Danilyuk, J.Purić, M.M.Kuraica, I.Dojčinović, and I.R.Videnović,
Structural modification of silicon surface by compression plasma flow action,
16th Europhysics Conference on Atomic & Molecular Physics (ESCAMPIG) and 5th International Conference on Reactive Plasmas (ICRP), July 14 – 18, 2002, Grenoble, Proceedings I, p.149.

NATIONAL CONFERENCES

I.Videnović, M.Kuraica, and N.Konjević,
Spectroscopic measurements of electric field strength in an abnormal glow discharge,
9th Congress of Physicists of Yugoslavia, Petrovac, May 29 – 31, 1995, Contributed papers, p. 449 (in Serbian).

M. Kuraica, I. Videnović, and N. Konjević,
Influence of the cathode material and working gas to the hydrogen Balmer line shapes in an abnormal glow discharge,
ibid. p. 413.

I. Videnović, M. Kuraica, and N. Konjević,
The use of atomic hydrogen line shapes for abnormal glow discharge diagnostics,
1st Yugoslav Conference on Spectral Line Shapes (YCSLS), September 11 – 14, 1995, Krivaja, Proceedings, Publ. Obs. Astron. Belgrade 50 (1995) p. 139.

N. Šišović, I. Videnović, M. Kuraica, V. Miljević, and N. Konjević,
Light source for the study of neutral gas pressure broadening,
ibid. p. 131.

I. R. Videnović, N. Konjević, and M. M. Kuraica,
On the use of atomic hydrogen line shapes for the excited hydrogen atoms temperature determination in a glow discharge,
2nd Yugoslav Conference on Spectral Line Shapes (YCSLS), September 29 – October 2, 1997, Bela Crkva, Proceedings, Publ. Obs. Astron. Belgrade 57 (1997) p. 125.

I. R. Videnović,
Characteristic line profile parameters of hydrogen Balmer lines in an external electric field,
3rd Yugoslav Conference on Spectral Line Shapes (YCSLS), October 4 – 6, 1999, Brankovac, Contributed Papers, J. Res. Phys. 28 (1999) p. 263.